On the role of Hall magnetohydrodynamics in magnetic reconnection: Astrophysical Plasmas

A thesis submitted in partial fulfillment of
the requirements for the degree of

Doctor of Philosophy

by

Kamlesh Bora

(Roll No. 17330016)

Under the guidance of

Dr. Ramitendranath Bhattacharyya

Professor

Udaipur Solar Observatory

Physical Research Laboratory, Udaipur, India.

DEPARTMENT OF PHYSICS

INDIAN INSTITUTE OF TECHNOLOGY GANDHINAGAR

2022

to

my parents

&

teachers

Declaration

I declare that this written submission represents my ideas in my own words and where others' ideas or words have been included, I have adequately cited and referenced the original sources. I also declare that I have adhered to all principles of academic honesty and integrity and have not misrepresented or fabricated or falsified any idea/data/fact/source in my submission. I understand that any violation of the above will be cause for disciplinary action by the Institute and can also evoke penal action from the sources which have thus not been properly cited or from whom proper permission has not been taken when needed.

(Signature)

(Name: Kamlesh Bora)

(Roll No: 17330016)

CERTIFICATE

It is certified that the work contained in the thesis titled **"On the role of Hall magnetohydrodynamics in magnetic reconnection: Astrophysical Plasmas"** by **Miss. Kamlesh Bora** (Roll no: 17330016), has been carried out under my supervision and that this work has not been submitted elsewhere for degree.

I have read this dissertation and in my opinion, it is fully adequate in scope and quality as a dissertation for the degree of Doctor of Philosophy.

Dr. Ramitendranath Bhattacharyya

(Thesis Supervisor)

Professor

Udaipur Solar Observatory

Physical Research Laboratory

Badi Road, Udaipur 313001, India

Thesis Approval

The thesis entitled

On the role of Hall magnetohydrodynamics in magnetic reconnection: Astrophysical Plasmas

by

Kamlesh Bora

(Roll No. 17330016)

is approved for the degree of

Doctor of Philosophy

Examiner	Examiner
Supervisor	Chairman

Date: ______________

Place: ______________

Acknowledgements

The completion of this thesis would not have been possible without the help and support of many people. Here, I would like to express my deep gratitude toward all of them.

Firstly, I am grateful to my Ph.D. supervisor Prof. Ramit Bhattacharyya for giving me the opportunity to work with him. I thank him for his continuous patience, support and valuable guidance throughout my Ph.D. tenure. Working with such a courteous mentor, who allowed me to work without any constraint, has been a great experience for me and turned me into an independent researcher.

I am indebted to my collaborators Prof. Piotr K. Smolarkiewicz, Prof. Qiang Hu, and Dr. Avijeet Prasad for their invaluable contribution and support in my scientific endeavors. I sincerely thank the members of my Doctoral Studies Committee, Dr. Aveek Sarkar, Dr. Brajesh Kumar and Dr. Bhuwan Joshi for evaluating my work on a regular basis. Their valuable comments helped me to improve the scientific outcomes.

I am thankful to USO admin Deputy Head, Prof. Nandita Srivastava for her kind support in the past four years. I extend my gratitude to Prof. Anil Bhardwaj, Director, PRL, Ahmedabad for providing necessary facilities to carry out my research work and organizing different acitivities to make the enviornment engaging. I express my deep gratitude toward IIT Gandhinagar for Ph.D. registration. I am also thankful to Dr. Bhushit Vaishnav, Head Academic Services, for his support with the academic matters. I wish to acknowledge the support of Vikram-100 cluster and thank all the staff members of PRL computer center for providing computational facilities. A special thanks to Mr. Jigar Raval for his timely help over any computational issues. I thank the SDO team for their open data policy. Thanks are due to administration and library staff members at USO and Ahmedabad for their timely and kind cooperation throughout my Ph.D. tenure. I sincerely thank all the faculty and staff members of USO for their kind cooperation.

This journey of past five years would not have been possible without the joyful company of my dear batch mates, seniors and juniors in PRL. I convey my sincere thanks to all of them for a pleasant stay in USO and PRL, Ahmedabad. I heartily thank my seniors, Dr. Avijeet Prasad, Dr. Sanjay Kumar, Dr. Ranadeep Sarkar, and Prabir Kumar Mitra for their invaluable support, and help toward learning the subject at initial stage. Without kind affection and company of Dr. Ranadeep Sarkar, Prabir Kumar Mitra, Binal Patel, and Satyam Agarwal, it would not have been possible to get through the COVID-19 pandemic. I specially thank my friends, *Mr. Himanshu Saxena, Ms. Shanwlee Sow Mondal, Mr. Partha S Jena, Mr. Vipin Kumar, Mrs. Rekha and my senior Surendra Vikram Singh for their kind support during my medical urgencies. I would also like to thank Sana, Pooja, and Anu for their joyful company always.*

Thanks are due to Mr. Kushagra Upadhyay and Mr. Ritesh Patel for supporting me and extending their help to me. I am indebted to Ms. Sapna Bist, who is like sister to me, for her unconditional love and support. I would also like to thank Ms. Eesha Dangi and Ms. Kriti Deva for always standing by me and for their love. It would be incomplete without accrediting Mr. Mintu Kumar for his continuous help and motivation to me. Completing this thesis timely without the constant help and support of Mr. Satyam Agarwal would not have been possible, I am deeply indebted to him for his unconditional support.

Lastly, I would like to thank my family, above all, my parents, for their unconditional love, lifelong support, and the freedom they have given me to pursue research. It gives me immense pleasure to dedicate this thesis to them. I must say, that being away from home, I have missed many opportunities to be with my family members. But, they have always been by my side everytime.

(Kamlesh Bora)

Abstract

Magnetic reconnection is a distinctive fundamental process which often causes explosive energy release phenomena in various astrophysical plasmas. Generally, the astrophysical plasmas are characterized by large magnetic Reynolds number ($R_M = Lv/\lambda$, in usual notations) owing to their inherent large length scale and high temperature. Large R_M causes the Alfvèn flux freezing theorem—magnetic flux being frozen to the plasma flow—to be satisfied. Reconnection occurs due to the violation of Alfvén's flux-freezing theorem at small length scales which generate in consequence of large-scale dynamics. Such small scales are characterized by large gradients in magnetic field and may occur as current sheets (regions of high current density) and magnetic nulls (locations where magnetic field vanishes; $\mathbf{B} = 0$). The multiscale behavior of reconnection makes it challenging to study the physics at small scales and capturing its effect on large scale dynamics simultaneously. Identification of the reconnection scale depends on the specific physical system under consideration. The outermost atmosphere of our nearest star Sun—solar corona, serves as a prototype astrophysical plasma. Large scale solar eruptions observed on the Sun, such as flares and coronal mass ejections (CMEs) are manifestation of magnetic reconnection. In particular, solar flares are fast and impulsive phenomena since huge amount of energy ($\approx 10^{32}$ ergs) is released suddenly and rapidly within a very short time period ($\approx$ few minutes to hours). Therefore, the underlying reconnections must be fast and impulsive too. The reconnection length scale in solar corona (based on observed impulsive rise time of hard X-ray emission during the solar flares) turns out to be few tens of meters. At this scale, the order analysis of the induction equation indicates that the order of Hall effect is much higher than the resistive diffusion. This leads to the Hall MHD description which can account for the impulsive behavior as compared to the traditional theoretical models of reconnection.

In the above backdrop, this thesis focuses on the investigation of Hall effect in 3D magnetic reconnection through numerical simulations. For the purpose, a Hall MHD solver is developed and benchmarked toward the known properties of Hall-assisted reconnection. For benchmarking, a comparative study using Hall MHD and MHD simulations is carried out. The simultions are initiated with an unidi-

rectional sinusoidal magnetic field (contained in xz plane of employed Cartesian geometry), having non-zero Lorentz force which initiates the dynamics. In MHD simulation, the evolution of magnetic field lines is symmetric and confined within the xz planes. Magnetic reconnections within each plane generate magnetic islands which, when stacked together along the y direction, appear as magnetic flux tube made by disjoint magnetic field lines. Contrarily, the Hall MHD simulation exihibits an asymmetric and three-dimensional (3D) evolution, owing to the development of an out-of-reconnection plane (xz plane) magnetic field component (B_y) which is quadrupolar. This is in agreement with the earlier Hall MHD simulations in the literature. Subsequently, the B_y component causes the formation of magnetic flux rope (MFR) in the computational domain. In their 2D projections, the rope and the flux tube appear as magnetic islands. Subsequent evolution exhibits the breakage of primary islands into secondary islands followed by their coalescence in both the simulations. However, the dynamics is faster during the Hall MHD. An important finding is the formation of twisted 3D magnetic structures which cannot be apprehended from 2D calculations, although their projections agree with the latter. The volume averaged current density rate shows abrupt changes during the Hall MHD—signifying the impulsiveness. Alongside, we have also explored the Whistler wave mode numerically vis-a-vis its analytical model and found the two to be matching reasonably well in Hall MHD simulations. Overall, the results agree with the existing scenario of Hall-assisted reconnection, thus validating the model.

Since, the evolution of an MFR is instructive to understand the CMEs and eruptive flares on the Sun, the numerical model is employed to perform Hall MHD and MHD simulations toward the generation and evolution of an MFR. The simulations are initiated with 2.5D and 3D bipolar sheared magnetic fields. In 2.5D case, MFR is levitating and unanchored while in 3D case, it is anchored to bottom boundary. The generation of MFR due to primary reconnections is identical for both the cases in the two simulations. However, subsequent evolution of MFRs is influenced by the Hall effect. In 2.5D case, Hall MHD evolution depicts the local breakage of MFR, owing to the internal reconnections. When viewed favorably, the structure appears as reminiscent of the “number eight (8)”. The temporal evolution of average magnetic energies, in the presence and absence of the Hall effect, is near-identical for both the cases and consistent with the theoretical expectation that the Hall term does not affect the magnetic energy evolution. In 3D case, the primary MFR gets generated in both the simulations due to repetitive reconnections at 3D null points. Subsequently, Hall MHD evolution features swirling motion of small scale twisted structures in the vicinity of 3D null points. The intermittent reconnections within these structures lead to the formation of large scale MFR which indicates the association of small scale dynamics with large scale structure formation—a key finding emphasizing the role of Hall effect in 3D reconnection.

Based on the accomplished knowledge about the Hall effect in 3D magnetic reconnection, finally, in this thesis, the role of Hall effect is explored for a solar flare. To achieve the aim, a C1.3 class flare on March 8, 2019 in solar active region (AR) 12734 is selected as a test bed and the numerical model is employed to perform the data-based Hall MHD and MHD simulations. Analysis of multi-wavelength observations from AIA instrument on board SDO reveals an elongated extreme ultraviolet (EUV) counterpart of the eruption in the western part of the AR, a W-shaped flare ribbon and the circular motion of chromospheric material in the eastern part. Subsequently, the magnetic field line morphologies over the AR are explored by employing the non-force-free field (non-FFF) extrapolation which uses the photospheric vector magnetogram from HMI insttrument on board SDO. The analysis of the extrapolated field reveals the presence of 3D nulls and quasi-separatrix layers (QSLs) which are favorable sites for 3D magnetic reconnection. A null point with fan-spine configuration is found in the middle of active region whose Hall MHD evolution is in better agreement with the tip of W-shaped flare ribbon. Further, the lower spine and fan remain anchored to the bottom boundary throughout the evolution, thus providing a pathway for post reconnection plasma flow while in MHD case, the lower spine gets disconnected. Notably, a MFR with QSLs as overlying field lines is found at the location of flare saturation in the SDO/AIA images. The Hall MHD simulation shows faster slipping reconnection of the flux-rope footpoints and overlying QSLs magnetic field lines. Consequently, the overlying magnetic field lines rise and reconnect in corona, thereby providing path for plamsa ejection. This finding agrees with the observed eruption in western part of AR. Contrarily, such significant rise of the flux rope and overlying field lines is absent in the MHD simulation, thus signifying the reconnection to be slower in MHD. Interestingly, such field line dynamics suggests a distinct mechanism of flux rope eruption in 3D, which is not widely documented in the literature. The result further emphasizes that null points and true separatrices in 3D may not be required for eruptive flares. Additionally, "fish-bone-like structure" surrounding a null line is found in the eastern part of the AR. A salient feature captured only in the Hall MHD is that rotating magnetic field lines agree remarkably with the observed circular plasma motion, both spatially and temporally.

Overall, investigations of Hall effect on 3D magnetic reconnection employing the numerical simulations initiated with both the analytical and observed magnetic fields display the significant changes in the magnetic structures around and on the reconnection site which subsequently alter the large scale dynamics making the evolution faster. Therefore, this thesis provides the Hall MHD as potential description to understand the faster reconnections in 3D with particular emphasis on the effects of structural dynamics at small scale on large scale structures.

Keywords: Magnetohydrodynamics, Hall magnetohydrodynamics, Magnetic reconnection, Solar active regions, Solar magnetic fields, Solar flares, Solar coronal mass ejections, Numerical simulations.

List of Publications

1. **K. Bora**, R. Bhattacharyya, Avijeet Prasad, Bhuwan Joshi, Qiang Hu (2022): *"Comparison of the Hall Magnetohydrodynamics and Magnetohydrodynamics Evolution of a Flaring Solar Active Region"*. In: *The Astrophysical Journal*, 925, 197. DOI: https://doi.org/10.3847/1538-4357/ac3bce

2. **K. Bora**, R. Bhattacharyya, P. K. Smolarkiewicz (2021): *"Evolution of Three-dimensional Coherent Structures in Hall Magnetohydrodynamics"*. In: *The Astrophysical Journal*, 906, 102. DOI: https://doi.org/10.3847/1538-4357/abc8f7

Contents

List of Figures

List of Tables

Chapter 1

Introduction

Most of the observable matter in the universe is predominantly in the form of magnetized plasma. Generally, the astrophysical plasmas are magnetized, having high Lundquist number ($S = Lv_A/\lambda$; L being the length scale of magnetic field variation, v_A being the Alfvén speed and λ being the magnetic diffusivity) causing the Alfvén's flux-freezing theorem (Alfvén, 1942) (discussed in detail later) to be satisfied. Dynamical evolution of such plasmas is often described by ~~the~~ ideal magnetohydrodynamics (MHD). Validity of frozen-in condition on magnetic field lines being tied to plasma parcels make it easier to study the dynamical evolution by tracking the motion of either one of them. However, unprecedented observations of explosive energy release phenomena such as flares and coronal mass ejections (CMEs) in ~~the~~ various astrophysical systems reveals the diffusive nature of plasma—breakdown of ideal MHD. The distinct fundamental process through which the magnetic energy is converted into other forms of energy *viz.* heat, kinetic energy of plasma flow and particle acceleration with the re-arrangement of magnetic field line connectivity is known as magnetic reconnection. In presence of electrical resistivity, the flux-freezing condition gets violated and makes the plasma diffusive.

In this Chapter, we present a brief historical overview of magnetic reconnection and introduce the concept. The potential sites of magnetic reconnection in two-dimension (2D) and three-dimension (3D) are described along with the aspects of 2D and 3D reconnection. Then, finally we present the Hall magnetohydrodynamics (Hall MHD) as a potential description to understand the fast and impulsive magnetic reconnection. The Chapter ends with the discussion of thesis objectives and its organization.

1.1 Magnetic reconnection: Historical Overview

Historically, the notion of magnetic reconnection stems from the ideas, first introduced by Giovanelli (1946) motivated from solar flare observations. Later on, the discussions between Giovanelli and Fred Hoyle, lead Hoyel to propose the process occurring in Earth's magnetosphere (auroral substorms) due to the interaction between solar wind and Earth's magnetic field (Hoyle, 1949). Their realization that the electric fields near magnetic X-type neutral point are responsible for the heating and particle acceleration might be based on the fact that particle acceleration is only possible when a component of electric field is parallel to the magnetic field. Later, Cowling (1953) suggested the solar flares owing to ohmic dissipation need a current sheet of only a few meters thick. Shortly, Dungey (1953) recognized that the magnetic reconnection process occurring in Earth's magnetic field is identical to the one in the solar flares. For the first time, Dungey (1953) demonstrated that the collapse of the X-type neutral points can actually form current sheets and proposed a cycle from magnetic reconnection at the magnetopause to reconnection at magnetotail in Earth's magnetosphere—specified as 'Dungey cycle'. It was Dungey who introduced the concept of "lines of force can be broken and rejoined" for the first time. In his pioneering works on ~~the~~ current sheets formation, Dungey treated the self-consistent nature of both plasma and magnetic fields rather than simple motion of charged particles in electric and magnetic fields. Based on the fact that moving charge particles produce the electric and magnetic fields, he used the MHD equations to investigate the effect of such fields where the Maxwell's equations are combined with Navier-Stokes equations.

Afterwards, Sweet (1958) and Parker (1957) proposed a two dimensional (2D) steady-state theoretical model of magnetic reconnection within MHD framework. Parker (1957) formulated the scaling laws for the model and coined the term "reconnection of field lines" or "merging of magnetic fields". Sweet-Parker mechanism of reconnection is detailed in Section 1.3.1.1. The rates at which magnetic energy gets converted into heat and plasma flow, is far too slow (10^9 years) to account for the energy release during solar flares. Subsequently, Petschek (1964) developed a "fast reconnection" model to account for solar flares which, is discussed in Section 1.3.1.2.

Initial developments of magnetic reconnection models were in 2D within MHD framework. Substantial amount of works have accomplished important aspects of 2D reconnection over several decades. However, understanding magnetic reconnection in three-dimensions (3D) is essential since the magnetic field in astrophysical plasmas is inherently 3D. Attempt to define magnetic reconnection have been made by Vasyliunas (1975); Sonnerup (1979), and Axford (1984) which will be discussed later in this chapter. These definitions are important in understanding existing scenarios of 3D magnetic reconnection and form the basis of general magnetic reconnection (GMR) theory suggested by Schindler et al. (1988); Hesse & Schindler (1988).

1.2 Concept of Magnetic Reconnection: An MHD Approach

As described above, the dynamical evolution of astrophysical plasmas is given by MHD description. Generally, MHD equations are a set of coupled differential equations combining the Maxwell's equations of electromagnetism and Navier-Stokes equations of fluid dynamics. MHD description of plasma is valid when the characteristic length and time scales of the system are much larger than the ion gyroradius and ion gyroperiod respectively. The set of MHD equations and their physical interpretation are given as following. Notably, here and hereafter, we use *SI* units except for numerical simulations carried out where cgs and dimensionless units are used.

1.2.1 MHD Equations

- Conservation of mass: Mass continuity equation

$$\frac{\mathcal{D}\rho}{\mathcal{D}t} + \rho(\nabla \cdot \mathbf{v}) = 0 \;\; or \;\; \frac{\partial \rho}{\partial t} + \nabla \cdot (\rho \mathbf{v}) = 0 \;, \tag{1.1}$$

where $\dfrac{\mathcal{D}}{\mathcal{D}t} \equiv \dfrac{d}{dt}$ is the total convective derivative, i.e., $\frac{\mathcal{D}}{\mathcal{D}t} = \frac{\partial}{\partial t} + \mathbf{v}\cdot\nabla$; ρ is the plasma density, and $\mathbf{v}$ is the plasma flow velocity. This equation implies that if mass flows into the system ($\nabla\cdot(\rho\mathbf{v}) < 0$) from the surrounding, the density increases ($\frac{\partial\rho}{\partial t} > 0$) whereas if mass flows out of the system ($\nabla\cdot(\rho\mathbf{v}) > 0$) the density decreases ($\frac{\partial\rho}{\partial t} < 0$).

- Conservation of momentum: Momentum balance or force balance equation

$$\rho\frac{\mathcal{D}\mathbf{v}}{\mathcal{D}t} = -\nabla p + \mathbf{J}\times\mathbf{B} + \rho\nu\nabla^2\mathbf{v} \ , \tag{1.2}$$

where p is the thermal pressure, $\mathbf{J}$ is the current density, $\mathbf{B}$ is the magnetic field, and ν is the kinematic viscosity of fluid.

- Electromagnetic induction equation

$$\nabla\times\mathbf{E} = -\frac{\partial\mathbf{B}}{\partial t} \ , \tag{1.3}$$

where $\mathbf{E}$ is the electric field.

- Ampere's law

$$\nabla\times\mathbf{B} = \mu_0\mathbf{J} \ , \tag{1.4}$$

where μ_0 is the permeability of vacuum.

- Ohm's Law

$$\mathbf{E} + \mathbf{v}\times\mathbf{B} = \mathbf{N} \ , \tag{1.5}$$

where $\mathbf{N}$ includes the forcing terms which will be discussed shortly.

- Solenoidality of magnetic field

$$\nabla\cdot\mathbf{B} = 0 \ , \tag{1.6}$$

- Energy equation

$$\frac{\mathcal{D}}{\mathcal{D}t}\left(\frac{p}{\rho^\gamma}\right) = 0 \ , \tag{1.7}$$

where $\gamma = \frac{5}{3}$ is the specific heats ratio for an adiabatic equation of state.

Combining Faraday-Maxwell's equation (Equation 1.3) and Ohm's law (Equation 1.5) essentially gives one of the fundamental MHD equation, namely, *induction equation*. The induction equation for ideal Ohm's law $\mathbf{E} + \mathbf{v} \times \mathbf{B} = 0$ can be written as :

$$\frac{\partial \mathbf{B}}{\partial t} = \nabla \times (\mathbf{v} \times \mathbf{B}) \ . \tag{1.8}$$

If the resistive Ohm's law is considered $\mathbf{E} + \mathbf{v} \times \mathbf{B} = \eta \mathbf{J}$, where η is the electrical resistivity, then the induction equation takes the following form

$$\frac{\partial \mathbf{B}}{\partial t} = \nabla \times (\mathbf{v} \times \mathbf{B}) + \lambda \nabla^2 \mathbf{B} \ , \tag{1.9}$$

where $\lambda \equiv \dfrac{\eta}{\mu_0}$ is the magnetic diffusivity. The first term on right hand side of the above equation is convective or advection term and the second term is resistive diffusion. The ratio of advection to resistive diffusion terms is known as magnetic Reynold's number, given by $R_M = L_0 V_0/\lambda$; L_0 being the length scale over which magnetic field varies and V_0 being the characteristic speed. It provides the useful information about the flow and magnetic field coupling in plasma, e.g. if $R_M >> 1$ (ideal limit) the advection processes govern the dynamics while the diffusion becomes unimportant, but if $R_M << 1$ (non-ideal limit) then the diffusive processes become significant.

1.2.2 Ideal limit ($R_M >> 1$)

The concepts of magnetic flux and magnetic field line conservation are essential to understand magnetic reconnection. Central to ideal MHD limit, both the magnetic flux and magnetic field lines are conserved which is discussed in the following.

1.2.2.1 Conservation of magnetic flux

In the limit of large magnetic Reynold's number ($R_M >> 1$), Alfvén's theorem (Alfvén, 1942) states that if magnetic flux through any closed curve is conserved then the magnetic field moves with the plasma as if the field is "frozen-in" or tied to the plasma parcels (Priest, 2014). Proof of this theorem can be presented by considering magnetic flux Φ through an area S of plasma restricted by a closed curve Γ :

$$\Phi = \iint_S \mathbf{B} \cdot \mathbf{da} \, , \tag{1.10}$$

where $d\mathbf{a}$ is an infinitesimal area S. If $\mathbf{B}$ is an explicit function of time or/and the contour line of this plasma element change, then the change in total magnetic flux can be due to the change of magnetic field strength following from the MHD equations (Φ') and due to the area change of plasma element (Φ'') so that :

$$\frac{d\Phi}{dt} = \frac{d\Phi'}{dt} + \frac{d\Phi''}{dt} \, , \tag{1.11}$$

where

$$\frac{d\Phi'}{dt} = \iint_S \frac{\partial \mathbf{B}}{\partial t} \cdot \mathbf{da}. \tag{1.12}$$

Now, let us consider a small change of the area $\mathbf{da}$ due to plasma motion withe $\mathbf{v}$ velocity in time interval dt, then:

$$\mathbf{da} = \mathbf{v} \; dt \times \mathbf{dl} \, , \tag{1.13}$$

where $\mathbf{dl}$ is an infinitesimal length element on contour Γ. Then, the change in magnetic flux due to area change can be given as

$$d\Phi'' = \mathbf{B} \cdot \mathbf{da} \, , \tag{1.14}$$

$$d\Phi'' = \mathbf{B}.\mathbf{v} \times \mathbf{dl} \; dt \, , \tag{1.15}$$

using the vector identities $\mathbf{A} \cdot (\mathbf{B} \times \mathbf{C}) = \mathbf{B} \cdot (\mathbf{C} \times \mathbf{A}) = \mathbf{C} \cdot (\mathbf{A} \times \mathbf{B})$ and $\mathbf{A} \times \mathbf{B} = -\mathbf{B} \times \mathbf{A}$ leads to

$$d\Phi'' = -dt(\mathbf{v} \times \mathbf{B}) \cdot \mathbf{dl} \, , \tag{1.16}$$

then the rate of change of flux due to area change is

$$\frac{d\Phi''}{dt} = -\int_\Gamma (\mathbf{v} \times \mathbf{B}) \cdot \mathbf{dl} \, , \tag{1.17}$$

employing Stoke's curl theorem in Equation 1.17 and substituting values of $\dfrac{d\Phi'}{dt}$ from Equation 1.12 and $\dfrac{d\Phi''}{dt}$ in Equation 1.11

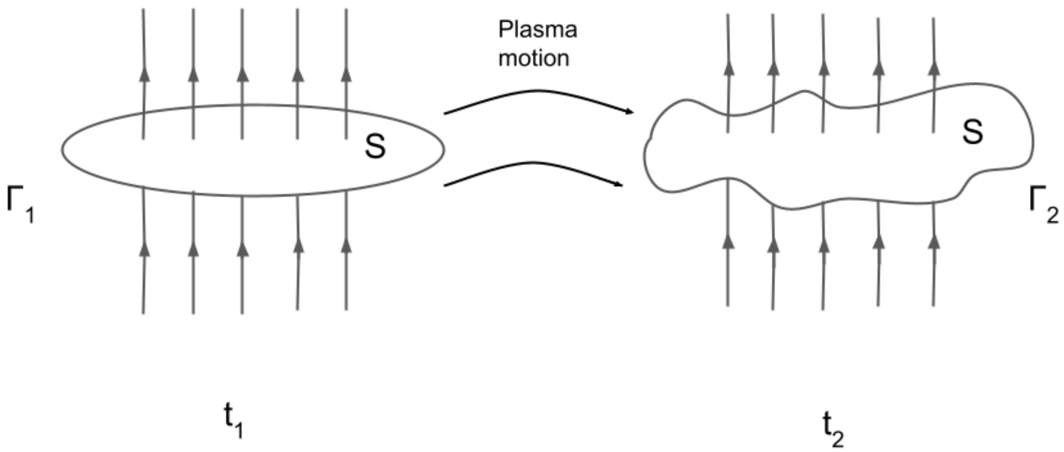

Figure 1.1: Conservation of magnetic flux through surface S, if the contour Γ_1 is deformed by plasma flow to make contour Γ_2, then the flux through Γ_1 at t_1 is equals to flux through Γ_2 at t_2.

$$\frac{d\Phi}{dt} = \iint_S \left(\frac{\partial \mathbf{B}}{dt} - \nabla \times (\mathbf{v} \times \mathbf{B})\right) \cdot \mathbf{da}\ . \tag{1.18}$$

For an ideal plasma ($R_M >> 1$), the right hand side vanishes in the above equation, therefore implying the *conservation of magnetic flux* through S. Figure 1.1 depicts the flux-conservation through a surface S, where the field lines lying on surface S within contour Γ_1 at t_1 remain on the same surface even after the deformation of Γ_1 into Γ_2 at t_2 by plasma motions.

1.2.2.2 Conservation of magnetic field lines

In ideal plasmas, conservation of magnetic field lines follows from the conservation of magnetic flux. Concept of magnetic field lines can be illustrated by writing induction equation in convenient form; using the vector identity* along with the solenoidality condition on magnetic field ($\mathbf{B}$)

$$\frac{\partial \mathbf{B}}{\partial t} + (\mathbf{v}\cdot\nabla)\mathbf{B} = (\mathbf{B}\cdot\nabla)\mathbf{v} - \mathbf{B}(\nabla\cdot\mathbf{v})\ , \tag{1.19}$$

*$\nabla \times (\mathbf{v}\times\mathbf{B}) = (\mathbf{B}\cdot\nabla)\mathbf{v} + \mathbf{v}(\nabla\cdot\mathbf{B}) - (\mathbf{v}\cdot\nabla)\mathbf{B} - \mathbf{B}(\nabla\cdot\mathbf{v})$

and combining it with the mass continuity Equation 1.1. In Equation 1.19, the first term on right-hand side indicates the magnetic field strength increases owing to either accelerating plasma motion along the field or the shearing motion normal to the field causing field to change direction by increasing the field component along the flow direction. The second term on right-hand side suggests the decrease and increase in the field strength depending upon the expansion ($\nabla \cdot \mathbf{v} > 0$) and compression $\nabla \cdot \mathbf{v} < 0$) of plasma respectively. Substituting the value of $\nabla \cdot \mathbf{v}$ in Equation 1.19 from mass-continuity equation

$$\frac{d}{dt}\left(\frac{\mathbf{B}}{\rho}\right) = \left(\frac{\mathbf{B}}{\rho} \cdot \nabla\right) \mathbf{v} \ , \tag{1.20}$$

To visualize Equation 1.20 resulting in field lines co-moving with plasma, let us take a length element $\delta\mathbf{r}$ along the magnetic field line moving with plasma. The plasma velocity at one end of length segment be $\mathbf{v}$ and at another end let velocity be $\mathbf{v}+\delta\mathbf{v}$; then $\delta\mathbf{v}= (\delta\mathbf{r} \cdot \nabla)\mathbf{v}$. Then, the rate of change of length element ($\delta\mathbf{r}$) within time interval dt can be expressed as

$$\frac{d\delta\mathbf{r}}{dt} = \delta\mathbf{v} = (\delta\mathbf{r} \cdot \nabla)\mathbf{v} \ , \tag{1.21}$$

which has the same form as of Equation 1.20, thus indicating that if vector $\dfrac{\mathbf{B}}{\rho}$ and length element $\delta\mathbf{r}$ are parallel at any time, will remain to do so for all the time. Hence, implying any two plasma parcels connected by the magnetic field line will remain connected for all the time in ideal plasmas—conservation of magnetic field lines.

1.2.3 Nonideal/diffusive limit ($R_M << 1$)

Any non-ideal term like resistive diffusion having form; $\mathbf{N} = \eta\mathbf{J} = \eta\nabla \times \mathbf{B}$ on the right-hand side of Equation 1.5, leads to the induction equation of form Equation 1.9. In the nonideal limit ($R_M << 1$), the induction equation has the following form

$$\frac{\partial \mathbf{B}}{\partial t} \approx \lambda\nabla^2\mathbf{B}. \tag{1.22}$$

A straightforward integration of Equation 1.22 yields

$$B = B_0 \exp\left(-\frac{t}{\tau_D}\right) \tag{1.23}$$

where $\tau_D \approx ({L_0}^2/\lambda)$ represents the diffusion time scale over which magnetic field lines diffuse out of the concerned plasma volume. Generalizing for non-ideal plasmas, further a flux transport velocity can be defined with a constraint that it should have same flux-preserving characteristics as that of ideal MHD, i.e., $\mathbf{w}$ should follow

$$\frac{\partial \mathbf{B}}{\partial t} = \nabla \times (\mathbf{w} \times \mathbf{B}) \ , \tag{1.24}$$

Nevertheless, using non-ideal Ohm's law (Equation 1.5) in Equation 1.3 leads to

$$\frac{\partial \mathbf{B}}{\partial t} = \nabla \times (\mathbf{v} \times \mathbf{B} - \mathbf{N}) \ . \tag{1.25}$$

On comparison of right-hand sides of above two equations the nonideal term can be expressed as

$$\mathbf{N} = \mathbf{u} \times \mathbf{B} + \nabla\Phi \ , \tag{1.26}$$

where $\mathbf{u}$ is the slippage velocity given by $\mathbf{u} = \mathbf{v} - \mathbf{w}$ and Φ is a scalar potential. Combining Equation 1.5 and Equation 1.26 gives

$$\mathbf{E} + \mathbf{w} \times \mathbf{B} = \nabla\Phi \ , \tag{1.27}$$

such that the flux velocity $\mathbf{w}$ is

$$\mathbf{w} = \mathbf{v} + \frac{(\mathbf{N} - \nabla\Phi) \times \mathbf{B}}{B^2} \ , \tag{1.28}$$

Since the flux transport velocity is not unique, its behavior depends on the particular magnetic field configuration under consideration which will be discussed in detail in Section 1.4. In ideal case, $\mathbf{w} = \mathbf{v}$, but for any nonideal term $\mathbf{w} \neq \mathbf{v}$. The reconnection involves a localized region where diffusion occurs having global effects.

1.3 Magnetic reconnection in two-dimensions (2D)

According to the historical overview presented in Section 1.1, features central to the concept of 2D magnetic reconnection are current sheets and magnetic neutral points. Current sheet is characterized as a narrow layer of current about which direction of magnetic field change. Collapse of magnetic X-type neutral points leads to the formation of current sheet. We describe both the magnetic null point and current sheet one by one subsequently.

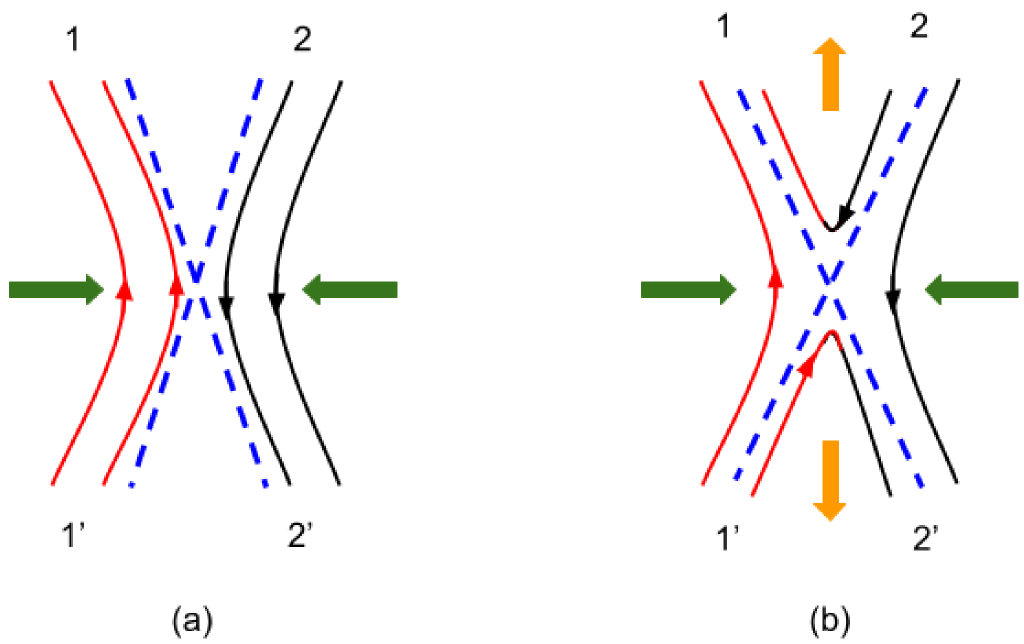

Figure 1.2: Panels (a) and (b) show the red and black field lines prior to and after the reconnection. In panel (a), red field lines connect region $1 \rightarrow 1'$ and black field lines connect region $2 \rightarrow 2'$. The blue dashed line is separatrix which separates topologically distinct regions. X-type null point is represented by the intersection of two separatrices in both the panels. The green arrows depict the converging plasma flow perpendicular to the magnetic field lines. Panel (b) depicts the topology of magnetic field lines after reconnection where the newly reconnected field lines connect the regions $2 \rightarrow 1$ and $1' \rightarrow 2'$.

Hyperbolic X-type null points are the preferential sites of magnetic reconnection in 2D. Figure 1.2 (a) and (b) depict the red and black field lines having different connectivities before and after the reconnection. Red field lines, directed from $1 \rightarrow 1'$ and black field lines, directed from $2 \rightarrow 2'$ (in panel (a)) are pushed by the converging plasma flows perpendicular to field lines. The blue dashed line, namely separatrix, separates the two distinct magnetic connectivity regions. Intersection of two separatrices is an X-type magnetic null point, where all components of magnetic field vanish implying $|\mathbf{B}| = 0$. After reconnection at X-point, the resulting field lines connect the region $2 \rightarrow 1$ and $1^{'} \rightarrow 2^{'}$. Therefore, the reconnection is topological re-arrangement of magnetic field lines in 2D.

Generally, current-sheets are tangential discontinuities, arising due to the failure of smooth magnetic field in an infinitely conducting plasma. Through current-sheets, magnetic field is tangential. To understand current-sheets in magnetized plasma, let us consider the magnetic field varying along x direction and directed towards z, i.e., $\mathbf{B} = B_z(x)\hat{\mathbf{z}}$ then the associated current density from Ampere's law becomes

$$J_y = \frac{1}{\mu_0}\frac{\partial B_z}{\partial x} , \tag{1.29}$$

which signifies that a steep gradient in B_z with x gives rise to a strong current density along the sheet ($z-$ direction) and perpendicular to the field lines. Spontaneous development of current sheets in an infinitely conducting plasma at equilibrium is expected from Parker's magnetostatic theorem (Parker, 1994). According to this theorem the current sheets develop in the limit $L_0 \rightarrow 0$, causing the volume current density to intensify and gets confined in a surface across which the magnetic field is discontinuous. A decrease in L_0 in the presence of finite but non-zero diffusivity λ locally reduces R_M and makes the plasma resistive; indicating the current sheets to be potential site for magnetic field diffusion which can host reconnection.

1.3.1 Steady-state models of magnetic reconnection in 2D: MHD framework

As discussed in Section 1.1, primarily, the efforts to model magnetic reconnection theoretically were purely in 2D within MHD framework. Here, we describe two famous models of magnetic reconnection; Sweet-Parker and Petschek.

1.3.1.1 Sweet-Parker Model

The first ever theoretical model of magnetic reconnection in 2D describing the scaling laws for reconnection rate was developed by Sweet and Parker independently. This model uses an *order-of-magnitude* approach to derive the reconnection rate. Basic assumptions of the model consist the incompressibility of fluid, low plasma$-\beta$ (where β is the ratio of kinetic pressure to magnetic pressure) and steady-state $\left(\frac{\partial}{\partial t} = 0\right)$ (Choudhuri, 1998), which leads to the reduced set of MHD equations given as following

$$\begin{aligned}
\mathbf{v} \cdot \nabla \rho &= 0 && (1.30)\\
\rho(\mathbf{v} \cdot \nabla)\mathbf{v} &= \mathbf{J} \times \mathbf{B} && (1.31)\\
0 &= \nabla \times (\mathbf{v} \times \mathbf{B}) + \lambda \nabla^2 \mathbf{B} && (1.32)\\
\nabla \cdot \mathbf{B} &= 0 && (1.33)
\end{aligned}$$

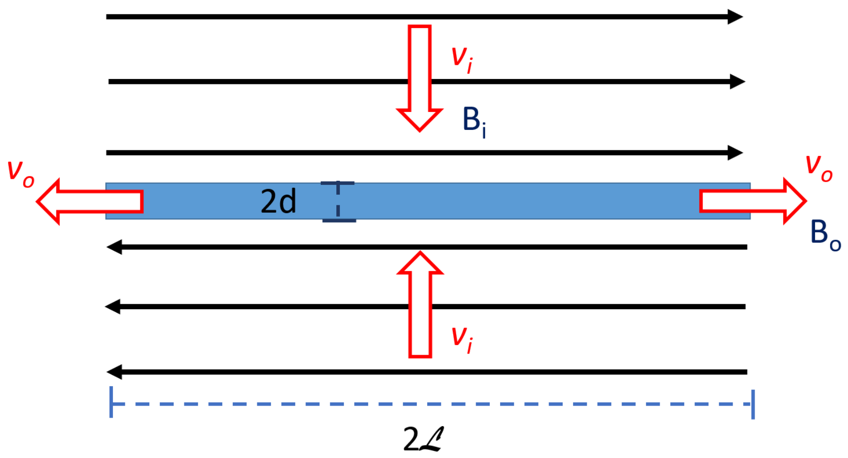

Figure 1.3: A schematic representation of Sweet-Parker mechanism of magnetic reconnection. The blue shaded rectangular region is the diffusion region of width $2d$ and length $2\mathcal{L}$. Black lines represent magnetic field lines and the red arrows represent the plasma flow directions.

A diffusion region or current sheet of length $2\mathcal{L}$ and width $2d$, sandwiched between the oppositely directed magnetic field $\pm B_i$ was considered. The plasma flow v_i is assumed in such a way that it pushes the oppositely directed magnetic field lines toward the diffusion region from both the sides (see Figure 1.3) and v_o is the outflow speed at both ends of the sheet. For an uniform mass density ρ, conservation of mass (from Equation 1.30) suggests that the rate at which mass enters the sheet $\rho(4\mathcal{L})v_i$ from both sides must be equal to the rate at which it leaves at both ends of the sheet $\rho(4d)v_o$, i.e.,

$$\mathcal{L}v_i = dv_o \ . \tag{1.34}$$

From the flux balance, we have

$$v_i B_i = v_o B_o \tag{1.35}$$

By order-of-magnitude analysis, the current density is J$\approx \dfrac{B_i}{\mu_o d}$ and the Lorentz force along the diffusion region is $(\mathbf{J}\times\mathbf{B})_x \approx JB_o = \dfrac{B_o B_i}{(\mu_o d)}$. Lorentz force accelerates the plasma from rest at the neutral point to v_o over a distance $\mathcal{L}$ and so, by Equation 1.31 where the plasma pressure gradient is neglected, we have

$$\rho\frac{v_o^2}{\mathcal{L}} \approx \frac{B_o B_i}{\mu_o d} \ . \tag{1.36}$$

Since the $\nabla \cdot \mathbf{B} = 0$ and dividing Equation 1.35 by Equation 1.34, gives

$$\frac{B_i}{\mathcal{L}} \approx \frac{B_o}{d} \ , \tag{1.37}$$

and Equation 1.36 then gives

$$v_o = \frac{B_i}{\sqrt{\rho\mu_o}} \approx v_A \ . \tag{1.38}$$

which is the expression for Alfvén speed v_A. From Equation 1.32, the advection term having order $\dfrac{v_i B_i}{\mathcal{L}}$ in the inflow region has to be balanced by the diffusion term of the order $\dfrac{\lambda B_o}{d^2}$ in the outflow region and using Equation 1.37 leads to

$$v_i = \frac{\lambda}{d} \ . \tag{1.39}$$

From Equation 1.34, Equation 1.38 and Equation 1.39, the reconnection rate is defined as the ratio of inflow speed to outflow speed, given as

$$\boxed{\frac{v_i}{v_o} = \frac{1}{\sqrt{S}}}$$

where $S = \mathcal{L}v_A/\lambda$ is the Lundquist number†. For typical solar coronal parameters, i.e., $\mathcal{L} \equiv 10^8$m, $v_A \equiv 10^6$ ms^{-1}, and $\lambda \equiv 1$ m^{2}s^{-1} (Aschwanden, 2005), the reconnection rate is 10^{-7} which is too slow to explain the observed explosive transients on the Sun, such as solar flare.

1.3.1.2 Petschek Model

Petschek (1964) proposed that the rate at which magnetic flux enters the diffusion region can be much faster, if the extent of diffusion region between the oppositely directed magnetic field is much smaller than the system or global length scale. He suggested that if L is the length of diffusion region and L_e is the system scale length then $L << L_e$. Let v_i and B_i be the plasma flow and magnetic field in

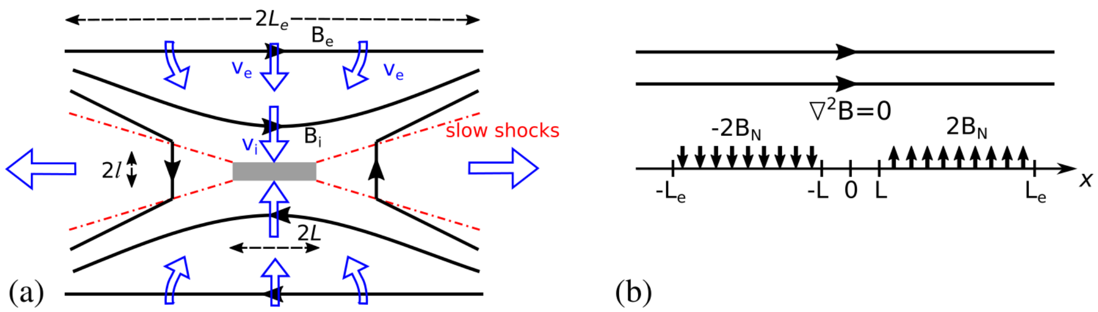

Figure 1.4: (a) A sketch of Petschek reconnection mechanism. The external magnetic field (B_e) over a large distances L_e is carried towards the diffusion region (grey shaded) by a flow v_e towards a diffusion region (shaded) of width 2l and length 2L. Near diffusion region, the inflow field is B_i and inflow speed is v_i. The slow shocks (red) heat and accelerate the plasma on the left and right sides of the diffusion region. (b) A schematic of upper inflow region. (Figure adapted from Pontin & Priest (2022))

the inflow region. Diffusion region is surrounded by an external region where the plasma flow is v_e and magnetic field is B_e. Then the reconnection rate (M_e) and Lundquist number (S_e) in the external region will be

$$M_e = \frac{v_e}{v_{Ae}}\,, \tag{1.40}$$

$$S_e = \frac{L_e v_{Ae}}{\lambda}\,. \tag{1.41}$$

Assuming steady-state, magnetic flux conservation leads to $v_iB_i = v_eB_e$. There-

†For $v_o = v_A$, the Magnetic Reynolds number R_M is called as Lundquist number.

fore,

$$\frac{M_i}{M_e} = \frac{B_e^2}{B_i^2} \ . \tag{1.42}$$

The magnetic field in the inflow region is assumed to be uniform and potential (current-free $\mathbf{J} = 0$). Specialty of Petschek model is that the four slow-mode MHD shock waves (standing in the flow) are responsible for the plasma acceleration parallel to the shock front (as shown in Figure 1.4),i.e., $v_e = v_s$ where v_s is the shock speed.

As shown in Figure 1.4, B_i is weakly curved near diffusion region in comparison to uniform B_e (far away from diffusion region) due to the normal component B_n of shocks on both sides. Let the shock speed be v_s which is given by $v_s = \dfrac{B_n}{\sqrt{\rho\mu_o}}$. Owing to shock in the region between L and L_e, $B_y = 2B_n$ and in the region between $-L$ and $-L_e$, $B_y = -2B_n$ on x axis (Figure 1.4(b)), the shock inclination is negligible elsewhere. At the diffusion region (between $-L$ to L), B_n vanishes. The total magnetic field in inflow region is the sum of two components, one is B_e along x axis and the another is achieved by solving Laplace's equation in the upper half of diffusion region. Magnetic field at the inflow region (B_i) can be given as

$$B_i = B_e - \frac{4B_n}{\pi} \log \frac{L_e}{L} \tag{1.43}$$

Using $v_e = v_s$ relation and dividing the numerator and denominator of the second term on the right hand side of above expression by $\sqrt{\rho\mu_o}$ leads to

$$B_i = B_e \left(1 - \frac{4M_e}{\pi} \log \frac{L_e}{L}\right) \ . \tag{1.44}$$

An increase in reconnection rate M_e causes an increase in shock angle while the size of diffusion region decreases. Petschek suggested that if the value of M_e is large enough then the process seizes off. He derived the expression for reconnection rate ($M_e^{'}$)

$$M_e^{'} \approx \frac{\pi}{8 \log S} \ , \tag{1.45}$$

which is much faster than the reconnection rate given by Sweet-Parker model. For solar flares, $M_e^{'} \approx$ 0.1-0.001. Hence, Petschek model is also known as *fast* *reconnection model.*

1.4 Magnetic reconnection in three-dimensions (3D)

As described in Section 1.3, the 2D models of magnetic reconnection are primarily associated with the X-type null point geometry (Pontin & Priest, 2022), which is relatively simpler than the far more complex and richer variety of preferential reconnection sites in 3D. Toward the aim of this thesis to investigate the Hall effect in magnetic reconnection, an understanding of reconnection sites in 3D is essential. Therefore, in this section, we elaborate on the various aspects of 3D reconnection, which are essential for our works presented in Chapter 5 and Chapter 6. We begin with a brief historical development of definition for 3D reconnection, followed by the description of reconnection sites in 3D such as null points, separator, quasi-separatrix-layers (QSLs), and hyperbolic flux tubes (HFTs).

Several definitions of magnetic reconnection in 3D exist in literature. For example, the attempts to define reconnection in 3D were primarily made by Vasyliunas (1975), Sonnerup (1979), and Axford (1984). According to Vasyliunas (1975) plasma flow across a separatrix surface is required for reconnection whereas Sonnerup (1979) suggested the electric field along the X-type neutral line or separator in 3D is necessary for reconnection. On the other hand, Axford (1984), proposed a change in magnetic field line "connection" between plasma elements owing to the localized breakdown of the "frozen-in field" as the basis of magnetic reconnection. Here "connection" means that plasma elements which are at one time connected by a single magnetic field line remain connected at subsequent times. Vasyliunas's and Sonnerup's definitions of magnetic reconnection require the identification of separatrix surface in 3D which needs the magnetic field line tracing to their origin. Identifying separator field line in 3D and distinguishing it from the surrounding field lines in realistic scenarios is difficult (Birn et al., 1997). Nevertheless, Axford's definition is general since it is not based on magnetic topology and does not require the tracing of field lines to their origin. However, it requires to track the temporal evolution of magnetic field line connection (Figure 1.5(a)) between plasma elements over a short time and possibly small distances. Axford's definition

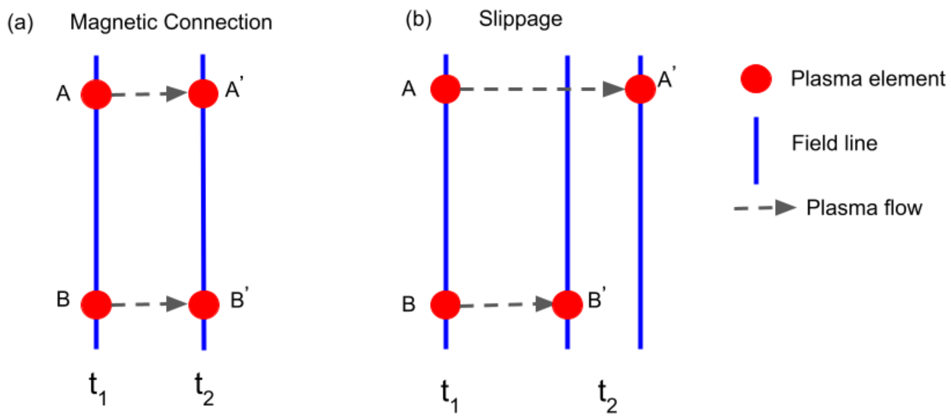

Figure 1.5: (a) Magnetic connection: Two plasma elements A and B connected by a magnetic field line at time t_1 remain ~~to be~~ connected by a magnetic field line at any other time t_2 under the plasma displacement. (b) Slippage: at time t_1 the plasma elements A and B are connected by a magnetic field line but at time t_2 plasma elements exchange the magnetic field lines and do not remain connected by a magnetic field line.

emphasizes on the exchange of magnetic field lines between the plasma elements, i.e., the breakdown of magnetic connections—slippage of plasma elements from magnetic field line. Later in 1988, this lead to the concept of general magnetic reconnection (GMR) (Schindler et al., 1988) which assumes the localized nonidealness. According to GMR, reconnection in 3D is classified into two categories: 1. Zero-B reconnection ($|B| = 0$ in the diffusion region), and 2. Finite-B reconnection ($|B| \neq 0$ in the diffusion region).

Following the aforementioned categorization of reconnection and central to the results presented in Chapter 5 and Chapter 6, further we discuss the 3D magnetic null (site for Zero-B reconnection) and its structure and QSLs (site for Finite-B reconnection).

- **3D null** A linear 3D null is a point in three-dimensional vector space, where all components of magnetic field vanish ($\mathbf{B} = 0$) and the field increases linearly away from the null point (Parnell et al., 1996). For example, in Cartesian coordinates, the magnetic field $\mathbf{B}$ for a linear 3D null can be given as

$$\mathbf{B} = x\hat{i} + y\hat{j} - 2z\hat{k} \ , \tag{1.46}$$

such that $\nabla \cdot \mathbf{B} = 0$. The magnetic structure around a linear 3D null point

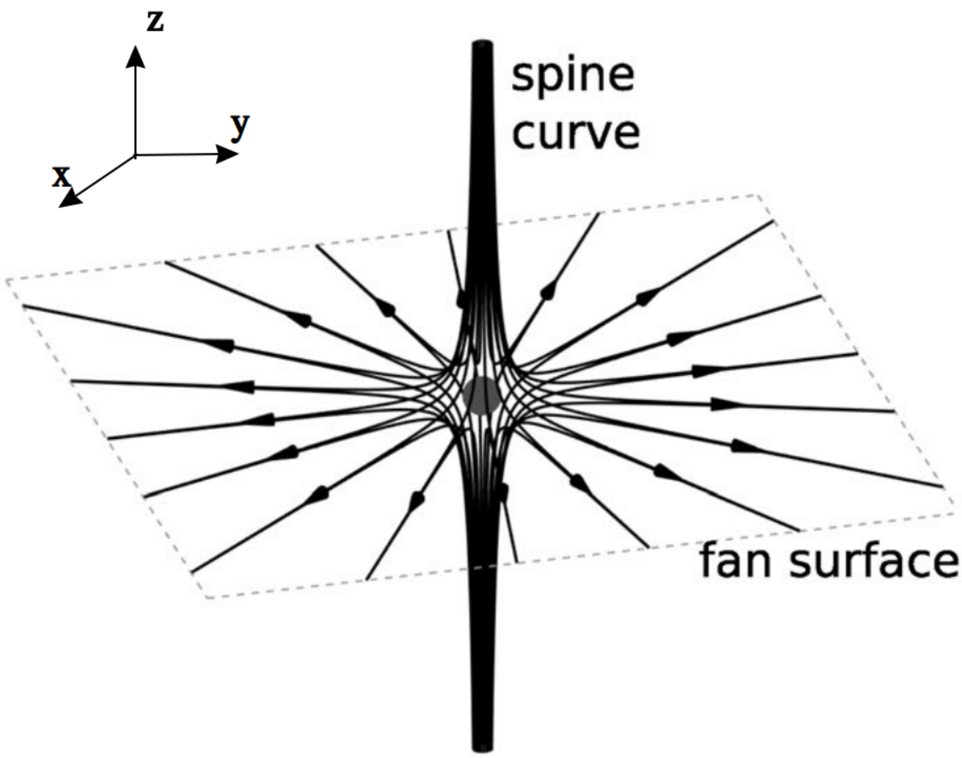

Figure 1.6: Magnetic structure around a 3D null point along with the spine curve and fan surface. (adapted from Pontin & Priest (2022))

consists two families of field lines, namely, spine and fan (Priest & Titov, 1996). A schematic representation of magnetic field line structure around a linear 3D null point is shown in Figure 1.6. Spine for the aforementioned field is along $z-$axis along which the bundle of magnetic field lines approach asymptotically whereas the receding field lines are tangential to a surface known as fan plane (xy plane). Fan plane acts as separatrix surface since it separates the distinct topological domains of magnetic field lines connectivities. If the field lines on fan plane radiate away from the null point then it is referred as a positive null point while if they approach toward the null point then it is referred as a negative null point (Pontin & Priest, 2022).

- **QSL** Reconnection in 3D can also take place without the null point. This idea was already conceptualized by Schindler et al. (1988) where the reconnection in the absence of null points was termed as finite-B reconnection. Following Schindler et al. (1988), if ~~the~~ Ohm's law given by Equation 1.5 is considered where $\mathbf{N}$ is a finite non-ideal term due to either collisions, fluctuations or particle inertia then this non-idealness can be important in a localized region with sharp gradients. In the convenient form, $\mathbf{N} = \eta \mathbf{J}$ can be assumed for Ohmic dissipation.

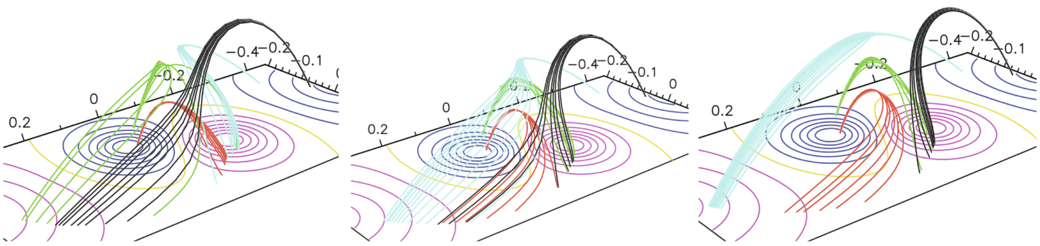

Figure 1.7: Illustration of the slip running or slipping reconnection of magnetic field lines in a numerical simulation of quasi-separator reconnection by Aulanier et al. (2006). Positive and negative polarities of magnetic field are represented by the pink and blue contours respectively on the bottom boundary. Four sets of magnetic field lines (red, black, cyan and green lines) are integrated from fixed footpoints and their conjugate footpoints gradually slip along arc-shaped trajectories from one positive to another positive polarities.

For the finite-B reconnection to take place in 3D, the necessary and sufficient condition is that the magnetic field be nonzero in the diffusion region and $\mathbf{B} \times (\nabla \times \mathbf{N}) = 0$ (Schindler et al., 1988; Hornig & Schindler, 1996) at a given point located in the diffusion region. These locations of enhancement in current density (current-sheets) can host the reconnection. Owing to the drastic change in magnetic field line connectivity (Demoulin et al., 1996, 1997; Titov, 2007) strong currents may arise, therefore, QSLs serve as preferential sites for 3D reconnection. In principle, this drastic change is quantified by the $Q-$value known as squashing factor. For the explanation of Q-value calculation, let us consider two footpoints $P_1(x_1, y_1)$ and $P_2(x_2, y_2)$. The footpoints are mapped from P_1 to P_2 and the associated Jacobian is given by

$$D_{1,2} = \begin{pmatrix} \dfrac{\partial x_2}{\partial x_1} & \dfrac{\partial x_2}{\partial y_1} \\ \\ \dfrac{\partial y_2}{\partial x_1} & \dfrac{\partial y_2}{\partial y_1} \end{pmatrix} = \begin{pmatrix} a & b \\ \\ c & d \end{pmatrix} , \tag{1.47}$$

owing to

$$Q = \frac{a^2 + b^2 + c^2 + d^2}{|\mathbf{B}_{n,1}(x_1, y_1)/\mathbf{B}_{n,2}(x_2, y_2)|} . \tag{1.48}$$

where $\mathbf{B}_{n,1}(x_1, y_1)$ and $\mathbf{B}_{n,2}(x_2, y_2)$ are the components normal to the target planes. According to Liu et al. (2016), $Q > 2$ is a criteria on squashing degree to represent the location of QSLs. The regions having large $Q-$values are prone to *slip-running* or *slipping reconnection* (Aulanier et al., 2006). The illustration of slipping reconnection is given in Figure 1.7. Following, the work of Aulanier et al. (2006), it can be seen in Figure 1.7 that the four sets of magnetic field lines (red, black, green, and cyan) change the connectivity from one positive to another positive polarity at the bottom boundary exhibiting the slipping reconnection.

1.5 Observed manifestations of magnetic reconnection

As mentioned in Section 1.1, the discovery of magnetic reconnection was primarily motivated from the spectacular observations of explosive transient events on the Sun and auroral substorms in Earth's magnetosphere. Since, these events are manifestation of magnetic reconnection, therefore we present the brief overview of properties and nature of such phenomena on the Sun as well as on Earth.

1.5.1 Explosive activities on the Sun

For this thesis, the solar coronal plasma has been selected as a prototype astrophysical plasma which exhibit diffusive behavior in the form of solar flares and CMEs. Solar flares are observed as intense brightening of any emission across the electromagnetic spectrum occurring at a time scale of minutes (Benz, 2008). Typically, energy ranging from $10^{28} - 10^{32}$ ergs is released during the solar flares within

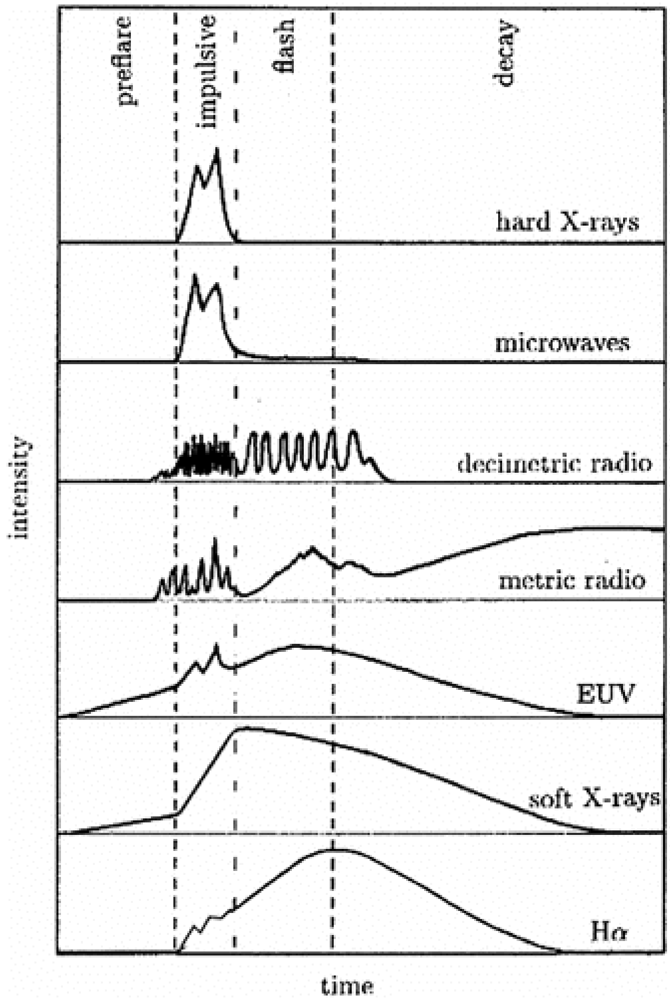

Figure 1.8: Illustration of intensity profile during flare for several wavelengths. The four phases, namely, pre-flare, impulsive, flash, and decay phases are indicated at the top. The different phases have different temporal durations.

a time span of few minutes (Benz, 2008). Temporal evolution of a flare is classified into four phases, namely the pre-flare, impulsive, flash, and decay phases. This characterization of different phases is based upon the temporal evolution of different emission profiles across the electromagnetic spectrum during a flare. Pre-flare phase is characterized by the energy build along with the slow heating of coronal plasma for which EUV and soft X-ray emission is detected. Impulsive phase of the flare is marked by the sudden peak in the hard X-ray emission where most of the energy is released and energetic particles are accelerated. Some high-energy particles get trapped and produce intensive emissions in the radio. The thermal soft X-ray and H_α emissions finally attain maxima after the impulsive phase, when energy is more smoothly released, manifest in decimetric pulsations. Flash phase is identified as the rapid increase in H_α intensity and line width and mostly coincides with the impulsive phase, although sometimes H_α may peak later. During the decay phase the coronal plasma reaches the relaxed state except at the high corona ($> 1.2R_\odot$, where $R_\odot$ is the radius of Sun), where plasma ejections and shock waves continue to accelerate particles, causing meter wave radio bursts. Aforementioned phases of solar flare have been shown in Figure 1.8, adapted from Benz (2008). Generally, magnetic reconnection is suggested to be responsible for such

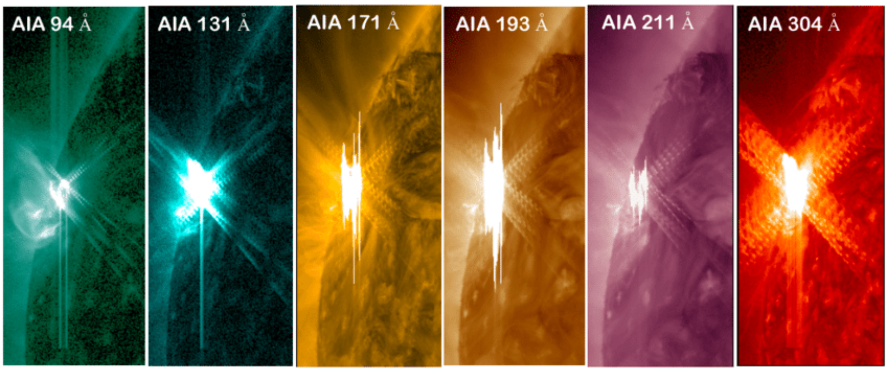

Figure 1.9: Multiwavelength observations of a solar flare as observed by SDO/AIA in six extreme ultraviolet (EUV) filters on eastern limb of the Sun on March 9, 2011.

sudden, rapid and intense energy release (Shibata & Magara, 2011). The strong enhancement of H_α, ultraviolet (UV), and EUV emissions are the signature of reconnection driven processes in solar corona. For example, one such enhancement in EUV emissions from Sun during a solar flare is shown in Figure 1.9.

Coronal Mass Ejections are gigantic clouds of magnetized plasma erupting from the solar corona into interplanetary space. The total mass and energy released during a typical CME ranges from 10^{15}-10^{16} g and 10^{27}-10^{33} ergs respectively (Vourlidas et al., 2002; Gopalswamy et al., 2004). Generally, CMEs show up signatures in white light owing to Thomson scattering of photospheric light from the free electrons of coronal and heliospheric plasma (Vourlidas & Howard, 2006; Howard & Tappin, 2009) which can be observed using coronagraph. In white light observations, mostly, CMEs have a three-part structure: a bright frontal loop (i.e., a leading edge (Illing & Hundhausen, 1985; Vourlidas & Howard, 2006), a dark cavity (low density, high magnetic field region (Low, 1996; Vourlidas et al., 2013) and a bright core embedded in the cavity (Illing & Hundhausen, 1985); cf. Figure 1.10. A near-consensus is that the magnetic reconnection plays an important role in initiating CMEs (Low, 1996; Chen, 2011). It is widely accepted

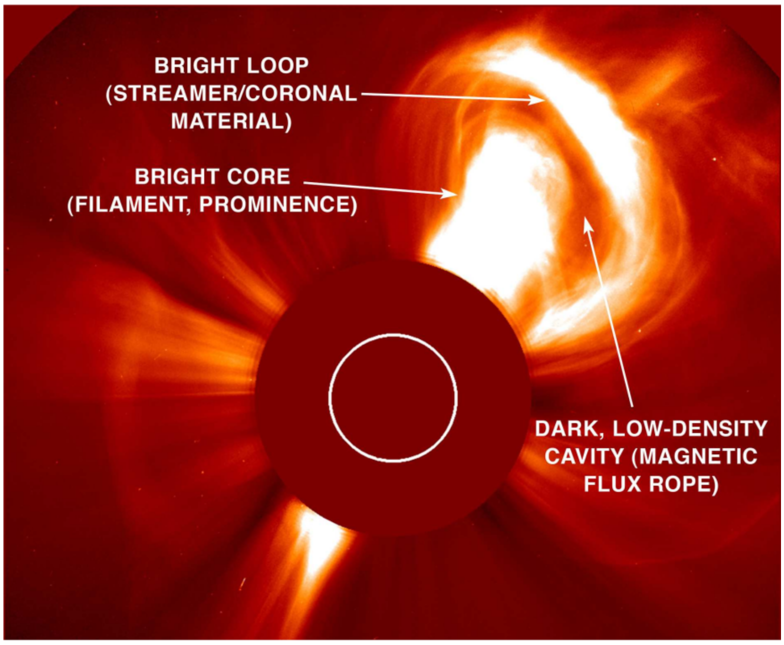

Figure 1.10: An observation of CME having classic three part structure: (a) bright frontal loop or edge, (b) a dark cavity, and (c) bright core region as viewed by Large Angle and Spectrometric Coronagraph Experiment (LASCO) on board Solar and Heliospheric Observatory (SOHO) spacecraft. This figure is adapted from Müller et al. (2013).

that most of the CMEs can be considered as erupting flux-rope systems, generating the classic three-part structure. Therefore, in this thesis, we study the evolution of magnetic flux ropes owing to magnetic reconnection and present the results in Chapter 5.

1.5.2 Geomagnetic activity on Earth

Intense geomagnetic storms and substorms, observed near Earth are caused mainly by large-scale solar eruptions (*viz.* flares, CMEs) and disturb the space weather. Naturally, the magnetic field carried by these eruptions from Sun, couple the solar, interplanetary and magnetospheric system as shown in Figure 1.11. Generally, if the Earth directed CMEs carrying southward magnetic field component (B_z) interact with the northward magnetic field of Earth on dayside (closest to the Sun), then the magnetic reconnection can take place (Dungey, 1961). Subsequently, the reconnected field is dragged by the solar wind—a continuous flow of plasma and magnetic field away from the Sun into interplanetary space, where it gets stretched on the night-side. Here it deposits magnetic energy to the magnetotail—

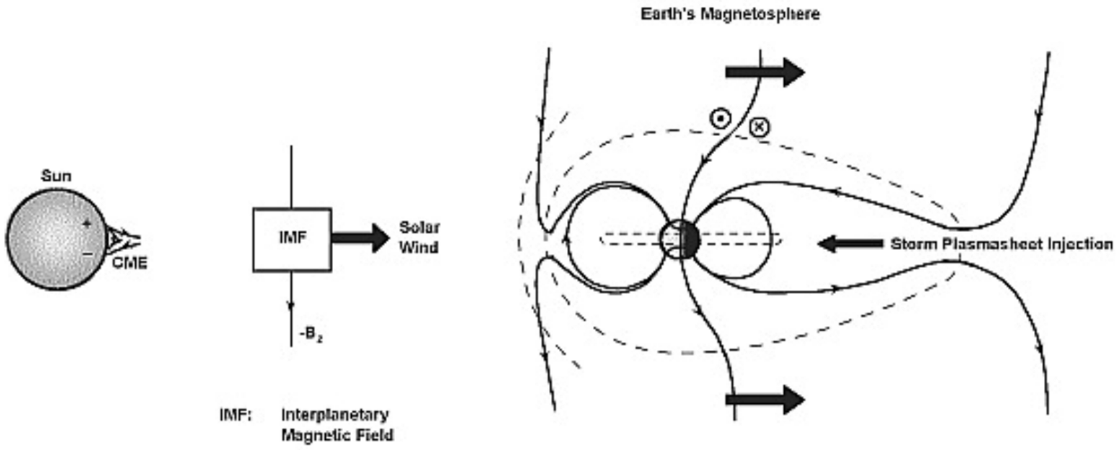

Figure 1.11: An illustration of coupling between magnetospheric and interplanetary magnetic field (IMF), depicting the magnetic reconnection and energy injection into the night side magnetosphere. This energy injection causes the development of ring current. (Figure adapted from Gonzalez & Tsurutani (1992).

the thin elongated region not facing the Sun. Consequently, on nightside the magnetic fields are configured in such a way that they are oppositely directed about magnetotail, (on the right hand side of Figure 1.11), so that they can reconnect. Then the superheated plasma from maggnetotail region flows back toward Earth, where it can penetrate all the way down to Earth's atmosphere and dissipate its energy to give rise *aurorae*. This cyclic process of magnetic reconnection at the magnetopause to reconnection at magnetotail is specified as the "Dungey cycle". The magnetotail reconnection causes the charge particles to get trapped in Earth's magnetic field where they gyrate following the Earth's magnetic field curvature and tend to move along the equatorial plane. The ions move westward (i.e. from midnight toward dusk) and electrons move eastward (i.e. from midnight toward dawn) ultimately generating the toroidal shaped ring current in westward direction surrounding the Earth. This ring current, in turn, induces the magnetic field which tends to reduce the horizontal component of Earth's magnetic field, responsible for the geomagnetic storm.

1.6 Importance of the Hall effect during magnetic reconnection: Hall MHD

As mentioned in Section 1.3, Sweet-Parker model is too slow to explain the reconnection rates for solar flare at the same time it does not account for the impulsive nature owing to steady-state assumption. While the Petschek model being steady-state gives fast reconnection rates but it can not explain the impulsive nature too and remains debatable since it is not realizable in the natural plasmas; see e.g., Biskamp (2000); Wang et al. (2000). Previous works (Terasawa, 1983; Scudder, 1997) suggest that in high-S plasmas, single-fluid MHD framework does not differentiate between the relative motions of different species. Considering Hall term ($\mathbf{J} \times \mathbf{B}$) in the Ohm's law can be useful attempt in this direction which leads to the Hall MHD description. In various astrophysical bodies, *viz.* dense molecular clouds, white dwarfs, or accretion disks, Hall effect plays a key role in the magnetic field dynamics; see, e.g., Mininni et al. (2003) and references therein. Over the past few years many studies (Ma & Bhattacharjee, 2001; Birn et al., 2001; Hesse et al., 2001; Otto, 2001) employing numerical simulation of Hall reconnection have found the fast reconnection rate or increase in reconnected flux. In work of Bhattacharjee et al. (2003), the Hall MHD simulation exhibits impulsiveness.

Hall MHD recognizes the importance of Hall effect in a generalized Ohm's law. Fundamentally magnetic reconnection is a multiscale process, so the identification of reconnection scale length is important which depends upon the particular system under consideration. To elucidate this, the reconnection scale length for a solar flare can be calculated by approximating the diffusion timescale (τ_d) with the impulsive rise time in hard X-ray emission which is of the order $10^2 - 10^3$ s. Thus, the reconnection scale length $L_\eta = \sqrt{\tau_d \lambda}$, for solar flare is ≈ 32 m where diffusion or reconnection time $\tau_d = 10^3$ s and $\lambda = 1$ m^{2}s^{-1}. Then the Lundquist number becomes $S \approx 10^7$. In solar corona, the ion-inertial scale length is $\delta_i = c/\omega_{pi} \approx 2.25$ m (Priest & Forbes, 2000) where $\omega_{pi} = \sqrt{\dfrac{ne^2}{m\epsilon_0}}$ being the plasma ion frequency, n is number density, m is mass and ϵ_0 is the permittivity of free space. For an electric field of form

$$\mathbf{E} + \mathbf{v} \times \mathbf{B} = \eta \mathbf{J} + \frac{\mathbf{J} \times \mathbf{B}}{ne} \,, \tag{1.49}$$

where $\left(\frac{\mathbf{J}\times\mathbf{B}}{ne}\right)$ is the Hall term, the dimensionless induction equation can be written as following

$$\frac{\partial \mathbf{B}}{\partial t} = \nabla \times (\mathbf{v} \times \mathbf{B}) - \frac{1}{S}\nabla \times \mathbf{J} - \frac{\delta_i}{L_\eta}\nabla \times (\mathbf{J} \times \mathbf{B}) \ , \tag{1.50}$$

using the following normalizations

$$\mathbf{B} \longrightarrow B_0\mathbf{B}, \quad \mathbf{v} \longrightarrow v_A\mathbf{v}, \quad t \longrightarrow \tau_A t, \quad \nabla \longrightarrow \frac{\nabla}{L_0}, \quad \mathbf{J} \longrightarrow \frac{B_0}{\mu_0 L_0}\mathbf{J} \ . \tag{1.51}$$

An order analysis of the above dimensionless induction equation (Equation 1.50) at reconnection scale length (i.e., $L_0 = L_\eta$) leads to the order of dissipation term $1/S \approx 10^{-7}$ being much smaller than the order of Hall term $\delta_i/L_0 \approx 10^{-2}$. Magnetic reconnection being the underlying reason behind solar flare and other coronal transients, Hall effect may play important role during reconnection. From Equation 1.50, it can be emphasized that the resistive dissipation term and Hall terms are important only when the strong current densities or magnetic field gradients exist. Since the order of magnitude for current density can be written as $J \approx B/L$ and the current (J) will be large only if the length scale L is sufficiently small. In case of solar coronal plasma, if the characteristic scale length L is of the order of megameter (Mm) then the currents are very small and ignorable but if it is reconnection scale length the currents have sufficiently large values. This reduction in length scale in turn leads to the reduction in Lundquist number signifying the diffusion to be important and the order of Hall effect being higher than diffusion term should not be ignored.

1.7 Properties of Hall effect on magnetic reconnection

Standardly, if the magnetic field is applied to a current carrying conductor in the direction perpendicular to current then a transverse electric field is developed in the conductor and this phenomenon is known as the *Hall effect* (Ramsden, 2006). Hall effect in the reconnection physics is well known to give fast reconnection rates.

In literature, the famous Geospace Environment Modelling (GEM) reconnection challenge by Birn et al. (2001) depicted the fast reconnection rates of the order of near Alfvènic inflow velocities with the Hall effect included in the different models ranging from fully particle-in-cell (PIC) codes to traditional resistive MHD codes. Numerical simulations in GEM challenge assumed an initial Harris current

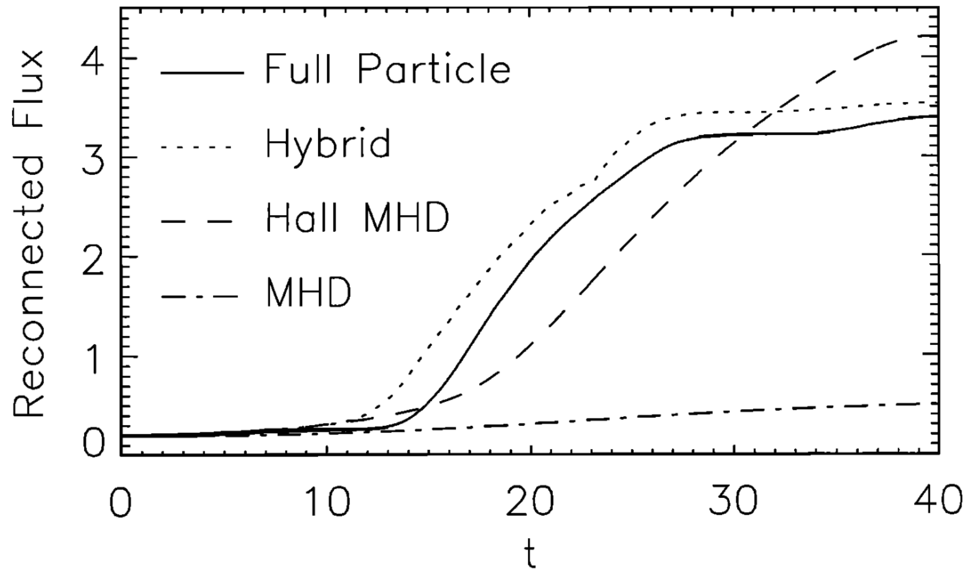

Figure 1.12: The temporal variation of reconnected magnetic flux from a range of numerical simulations with different models including full particle, hybrid, Hall MHD, and MHD, adapted from Birn et al. (2001).

sheet equilibrium perturbed by the magnetic island to initiate the dynamics. The Figure 1.12, taken from Birn et al. (2001), shows the temporal variation of reconnected magnetic flux for different simulations from fully particle, hybrid, Hall MHD and MHD models. The slope of reconnected magnetic flux versus time curve gives the reconnection electric field. As evident from Figure 1.12, all the models including Hall effect give the approximately same and larger reconnection rate as compared to MHD. Noticeably, simulation results for the models including Hall effect emphasize that the reconnection rate is almost insensitive to the particular mechanism (thermal motion of particle, electron inertia or resistivity) responsible for the breakdown of frozen-in condition.

According to Bhattacharjee et al. (2003), the observed impulsive phase of a solar flare imposes an important constraint on any magnetic reconnection model explaining flare that not only the timescale of growth rate of current density and electric field has to be fast but the time derivative should also increase abruptly.

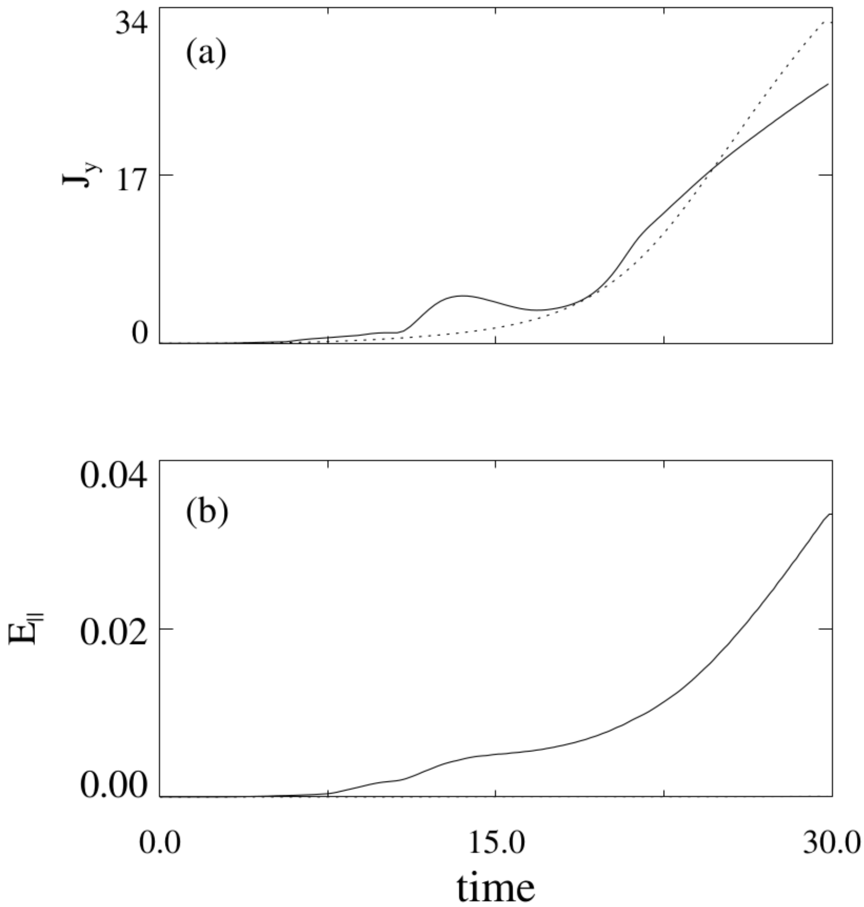

Figure 1.13: Growth rate (time evolution) of amplitudes of (a) current density J_y and (b) electric field $E_{||}$ for the Hall MHD and MHD simulations depicted by solid and dotted curves respectively from Bhattacharjee et al. (2003).

In their work, a comparative study of Hall MHD and MHD simulations initiated with a 2D solar like magnetic arcade configuration revealed the sudden and fast growth rate of current density and electric field during the Hall MHD evolution—signifying greater degree of impulsiveness, as shown in Figure 1.13 (adapted from Bhattacharjee et al. (2003)).

Hall effect being important at ion-inertial length scale cause the decoupling of ion and electron motion. Consequently, in the ion diffusion region the ions diffuse out from the magnetic field line and plasma flow is frozen into the electron fluid only. To elucidate, let us consider the induction equation (Equation 1.50) and ignoring the resistive diffusion term, then a velocity can be defined as $\left(\mathbf{v} - \frac{\delta_i}{L_\eta}\mathbf{J}\right)$ by combining first and last terms on the right hand side and then, the induction equation can be written as

$$\frac{\partial \mathbf{B}}{\partial t} = \nabla \times (\mathbf{w} \times \mathbf{B}) \tag{1.52}$$

where $\mathbf{w} = \left(\mathbf{v} - \frac{\delta_i}{L_\eta}\mathbf{J}\right)$ is the electron flow velocity. Hall term, being ideal, does not cause any change in the magnetic energy and helicity rates (Priest & Forbes, 2000; Liu et al., 2022). However, following Hornig & Schindler (1996), the velocity $\mathbf{w}$ conserves magnetic flux (Schindler et al., 1988) and topology (Hornig & Schindler, 1996) since field lines are tied to it. Consequently, field lines slip out from the fluid parcels advecting with velocity $\mathbf{v}$ to which the lines are frozen in ideal MHD. Importantly, the resulting breakdown of the flux freezing is localized to the region where current density is large and the Hall term is effective. Because of the slippage, two fluid parcels do not remain connected with the same field lines over time—a change in field line connectivity. Quoting Schindler et al. (1988), such localized breakdown of flux freezing, along with the resulting change in connectivity, can be considered as the basis of reconnection Axford (1984). Additional slippage of field lines occurs in the presence of resistive diffusion term, but with a change in magnetic topology.

Apart from modeling efforts to explore the role of Hall effect on magnetic reconnection, efforts have also been made to observe the magnetic reconnection in Earth's magnetosphere with an aim to probe the ion diffusion region physics. The Magnetospheric Multiscale Mission (MMS) has provided important insights into the ion diffusion region physics. Mozer et al. (2002) proposed a model of magnetic reconnection including Hall effects which is purely based on the observations. A schematic picture of the diffusion region (Mozer et al., 2002) surrounding the reconnection site is depicted in Figure 1.14. In Figure 1.14, the magnetosheath on left and magnetosphere on right side have oppositely directed magnetic field lines (thick black lines directed along z) pointing southward (down) on left and northward (up) on right side. The magnetic field lines are convected along x direction toward magnetopause by inflow. When the field lines are in white part (away from diffusion region), the ideal MHD is satisfied and the electric field have dominant contribution from convection term such that the resultant electric field $-v_x B_z$ is in

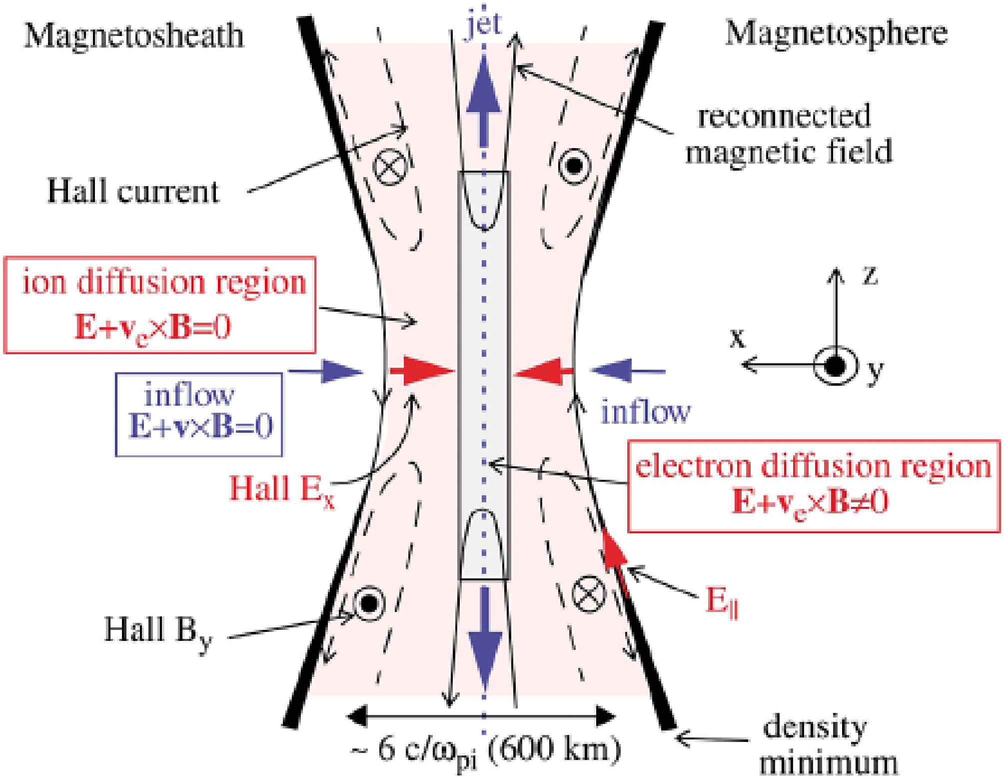

Figure 1.14: A sketch of the diffusion region around the magnetic reconnection site for a symmetric system (adapted from Mozer et al. (2002)). The green line shows the approximate trajectory of the Polar satellite for an observed event shown in Figure.

positive y direction and this out-of-reconnection plane field is known as reconnection electric field. In a region where the gyrating ions reach a distance apart which is equal to their gyroradius, they get demagnetized and decouple from magnetic field but the electrons continue to be frozen to the magnetic field due to their gyroradius being smaller than that of ions, is known as ion diffusion region. There is a net current $\mathbf{J} = nq(\mathbf{v}_i - \mathbf{v}_e)$ generated by the bulk flow of electrons (shown by dashed curves in Figure 1.14) in the ion diffusion region along x direction, also known as *Hall current*. This in-plane (xz plane) Hall current generates an out-of-reconnection plane magnetic field component along y direction which is known as *Hall magnetic field*. The nature of this out-of-reconnection plane Hall magnetic field is quadrupolar owing to the in-plane current which wraps the associated magnetic field around it according to the Ampere's law. Consequently, it causes the Hall magnetic field to point out of the plane (along positive y direction) on upper right and lower left while pointing into the plane (along negative y direction) on upper left and lower right. Since, the ion diffusion region has a width equal to the ion-inertial scale length δ_i, the Hall term $\mathbf{J} \times \mathbf{B}$ gives rise to an electric field in positive y direction which is equal to $J_x B_z$ which is in the same direction as that of convective electric field. Alongside, the Hall magnetic field along y direction and current along z direction together produce *Hall electric field* along x direction which is depicted by two oppositely directed red arrows pointing toward the magnetopause on either side of it. In summary, the Hall effect play a crucial role during magnetic reconnection by giving fast reconnection rates, greater degree of impulsiveness, and altering the dynamics. Main properties of Hall-assisted reconnection are the generation of an out-of-reconnection plane quadrupolar Hall magnetic field, in-plane Hall current and Hall electric field. Although, the Hall effect in 2D or 2.5D magnetic reconnection is well studied but the understanding on its role in 3D reconnection lacks.

1.8 Motivation and Organization of the Thesis

In the above backdrop, presented in Section 1.6 and Section 1.7, the motivation of this thesis is to study the role of Hall effect on magnetic reconnection in astrophysical plasmas, in general, and particularly in solar coronal plasma. To fulfill the aim, the specific objectives of this thesis are outlined below:

1. Development of a 3D Hall MHD solver by modifying the existing computational model EULAG MHD and benchmark the model to validate the properties of Hall reconnection.

2. Understanding the Hall-assisted reconnection dynamics of a magnetic flux rope by means of Hall MHD simulation and its comparison with the MHD evolution.

3. Comparative study of the possible magnetic reconnections in 3D causing the observed flare brightening in the lower solar atmosphere employing the data-constrained Hall MHD and MHD simulations.

Based on the work carried out to accomplish the above mentioned objectives, the thesis is organized into seven chapters. A brief description of each chapter is given below.

Chapter 1: Introduction

This Chapter starts with the historical overview of magnetic reconnection followed by introduction to the concept of magnetic reconnection. A revisit of the existing 2D models of magnetic reconnection and reconnection rates within the MHD framework is presented. Their limitation to explain the impulsive and fast nature of explosive events are described. Subsequently, the 3D magnetic reconnection and sites for reconnection in 3D are discussed. Then the observational manifestations of reconnection on Sun and Earth are presented as examples. A brief overview of the previous efforts to achieve the fast reconnection rate is discussed briefly. Later, the motivation behind Hall MHD is described with the emphasis on inevitability of Hall effect in magnetic reconnection in the solar corona. The properties of Hall effect on magnetic reconnection are described in detail. Lastly, the chapterwise organization is presented.

Chapter 2: Solar Coronal Magnetic Field Models and Coronal Transient Observations

The solar coronal plasma has been selected as a prototype astrophysical plasma due to the wealth of observational data. This Chapter focuses on the coronal magnetic field models depending upon the zero and non-zero Lorentz force ($\mathbf{J} \times \mathbf{B}$) on photosphere, i.e., force-free and non force-free approaches are discussed in detail. To study reconnection the vector magnetic field is required which is obtained using the non force-free extrapolation technique to initiate the data-based simulations in Chapter 6. The flare observations and magnetic field data utilized for extrapolations in this thesis are obtained from the Atmospheric Imaging Assembly (AIA) and Heliseismic Magnetic Imager (HMI) instruments onboard Solar Dynamic Observatory (SDO).

Chapter 3: Numerical model

In this Chapter, the detailed description of the EULAG MHD—a widely used computation model is presented. EULAG uses MPDATA advection and Implicit Large Eddy Simulation (ILES) schemes which are discussed in detail. Utilizing the ILES property and the flux conservative form of EULAG solver the Hall forcing term is incorporated in the model and discussed in detail in this Chapter.

Chapter 4: Benchmarking the 3D EULAG HMHD solver

This Chapter documents the benchmarking results of the 3D EULAG HMHD solver. As emphasized in the introduction, the focus here is to explore reconnection dynamics in the Hall MHD with its properties such as faster reconnection and impulsiveness. Both the properties are verified along with the key highlights of 3D nature of magnetic field line evolution. Additionally, only the whistler wave modes are investigated. Since the model assumes incompressibility and homogeneous plasma density, Hall drift wave modes are not considered. There is a good agreement between the numerical and analytical whistler wave modes frequency, detailed in this Chapter. The description of the 3D Hall MHD solver and benchmark validation results are published in Bora et al. (2021).

Chapter 5: Investigation of the Hall effect on magnetic reconnection during the evolution of a magnetic flux rope

In this Chapter, the influence of the Hall forcing on generation and ascend of a magnetic flux rope generated from bipolar sheared magnetic arcades is discussed for two cases. The first case uses initially axisymmetric (2.5D) while the second case uses initially 3D bipolar sheared magnetic arcade configurations for the simulations. The details of reconnection during the Hall MHD and MHD evolution of the rope along with the energetics are highlighted. The results of the first case of this work have been published in Bora et al. (2021). The results of the second case study are presently under preparation toward communication in a peer-reviewed journal.

Chapter 6: Comparison of the magnetic reconnection in a flaring solar active region using data-constrained Hall MHD and MHD simulations

This Chapter contains a comparative study of possible magnetic reconnections causing the flare brightening in the lower solar atmosphere. The data-constrained

Hall MHD model is employed to simulate a C1.3 class flare in active region NOAA 12734 as a test bed. The Chapter starts with the description of salient spatiotemporal features observed in the SDO/AIA multi wavelength channel images. Further, the non force-free-field (non-FFF) extrapolation utilizing the SDO/HMI vector magnetogram is discussed. A detailed numerical analysis to detect the favorable topologies for magnetic reconnections is presented. Finally, the differences in the magnetic reconnection dynamics during the Hall MHD and MHD evolution are presented. The results of this work have been published in Bora et al. (2022).

Chapter 7: Summary and Future Work

This Chapter presents the summary of the work carried out focusing on the major findings of the thesis. Further scope for the future work is also discussed.

Chapter 2

Solar Coronal Magnetic Field Models and Coronal Transient Observations

2.1 Introduction

The importance of Hall effect in magnetic reconnection has been illustrated in Chapter 1. The central aim of this thesis is to investigate the Hall effects on magnetic reconnection in astrophysical plasmas. Toward such an aim, magnetic reconnections leading to solar coronal transients can be used as testbed. As an initial exploration, we select a solar flare (more details in Chapter 6) and perform data-constrained numerical simulations to explore the underlying mechanism of reconnection. In this regard, solar observations play an important role because: (a) multiwavelength imaging of the transient activity helps in the understanding various spatial features and it's temporal evolution, (b) measurements of magnetic field allow one to understand the magnetic topology and field line dynamics in the solar corona. However, most of the ground and space based observatories, provide the routine measurements of vector magnetic field only on the photosphere. Such extensive and accurate measurements are not available for the solar corona, leading to the necessity of coronal magnetic field modeling. Such model based approaches are referred to as extrapolation techniques. In this thesis, the multi-wavelength observations have been obtained from the Atmospheric Imaging

Assembly (AIA) instrument and the photospheric magnetic field is acquired from the Helioseismic Magnetic Imager (HMI) instrument, both onboard the Solar Dynamics Observatory. In this Chapter, the description of coronal magnetic field extrapolation models is presented in detail and a brief description of the aforementioned instruments along with the details of their data acquisition techniques is also provided.

2.2 Coronal magnetic field models

Since, the routine measurements of magnetic field are possible for photosphere only, the modeling of coronal magnetic field is an essential and indispensable tool for the understanding of complex magnetic morphologies. Generally speaking, the successful measurements of magnetic field in the solar atmosphere have been possible with the technique of spectropolarimetry, which relies on the principle of Zeeman effect. It is based on the concept that in the presence of high strength magnetic field, magnetically sensitive spectral lines split into their components. The splitting is given by $\Delta\lambda \propto \lambda^2 g B$ where λ is the wavelength, g is the Lande's g-factor and B is the magnetic field strength. Measuring magnetic field in the solar corona is challenging because (a) magnetic field strength is very low ($\sim 10 - 100$ G) as compared to the photosphere ($\sim 10^3$ G), (b) The million degree Kelvin temperature in corona (Aschwanden, 2005) results in thermal broadening. The extrapolation techniques have emerged as feasible and alternate solution to provide the quantitative information about coronal magnetic field. Such schemes are broadly classified into force-free and nonforce-free, dependng on whether they allow a zero or non-zero Lorentz-force ($\mathbf{J} \times \mathbf{B}$) at the bottom boundary. We present a detailed description of these models in the following sections.

2.2.1 Force-free models

It is well established that the dynamical evolution of the coronal magnetofluid is given by the magnetohydrodynamics (MHD) description (see Chapter 1). Then, for a physical system characterized by length scale L and Alfvén transit time $\tau_A = L/v_A$ (in SI units), where $v_A = \dfrac{B_o}{\sqrt{\mu_0 \rho}}$ is the Alfvén speed, the normalized force-balance equation along with the other MHD equations can be written as following:

$$
\begin{aligned}
\frac{L}{\tau_o v_o}\frac{\partial\bar{\rho}}{\partial\bar{t}} + \bar{\nabla}\cdot(\bar{\mathbf{v}}) &= 0\ , &(2.1)\\
\bar{\rho}\left(\frac{\tau_A}{\tau_o}\frac{\tau_o}{\tau_A}\frac{\partial\bar{v}}{\partial\bar{t}} + \frac{{v_o}^2}{{v_A}^2}\bar{\mathbf{v}}\cdot\bar{\nabla}\bar{\mathbf{v}}\right) &= \bar{\mathbf{J}}\times\bar{\mathbf{B}} - \frac{\beta}{2}\bar{\nabla}\bar{p} - \frac{\beta_g}{2}\bar{\rho}\bar{\nabla}\bar{\psi}\ , &(2.2)\\
\frac{L}{\tau_o v_o}\frac{\partial\bar{\mathbf{B}}}{\partial\bar{t}} &= \bar{\nabla}\times(\bar{\mathbf{v}}\times\bar{\mathbf{B}})\ , &(2.3)\\
\bar{\nabla}\cdot\bar{\mathbf{B}} &= 0\ , &(2.4)
\end{aligned}
$$

where bars represent the dimensionless quantities. τ_o and v_o are the typical characteristic time scale and flow speed respectively, $\beta = 2\mu_o p_o/{B_o}^2$ is the plasma-β parameter which is the ratio of kinetic pressure (p_o) and magnetic pressure (${B_o}^2/2\mu_o$), $\beta_g = 2\mu_o\rho_o\psi_o/{B_o}^2$ is the ratio of gravitational energy density and magnetic pressure where $\mathbf{g} = \nabla\psi$, ψ being the gravitational potential. However, if the characteristic timescale over which the magnetic morphology of a region varies, is large compared to the Alfvén transit time, then the magnetohydrostatic approximation can be considered appropriate (Wiegelmann & Sakurai, 2021). In the limit of sub-Alfvénic flows, Equation 2.2 becomes

$$
0 = \bar{\mathbf{J}}\times\bar{\mathbf{B}} - \frac{\beta}{2}\bar{\nabla}\bar{p} - \frac{\beta_g}{2}\bar{\rho}\bar{\nabla}\bar{\psi}\ , \qquad (2.5)
$$

Therefore, Equation 2.1 and Equation 2.3 now become inconsequential and Equation 2.5 is known as the magnetohydrostatic equation. Terms in this equation have varying strengths relative to each other in different layers of the solar atmosphere, which can be understood using the work of Gary (2001). In his work, a simple one-dimensional model for magnetically and density stratified solar atmosphere was constructed. As shown in Figure 2.1, this model constrains the magnetic and plasma pressures based on the various observations at different heights in the solar atmosphere. Evidently, the magnetic field dominates the plasma dynamics in the mid-corona (β <1), whereas on the photosphere, the plasma dominates the dynamics (β >1), except in the active regions. According to Gary (2001)'s plasma β profile (Figure 2.1), for the region between 10-100 Mm height in the solar at-

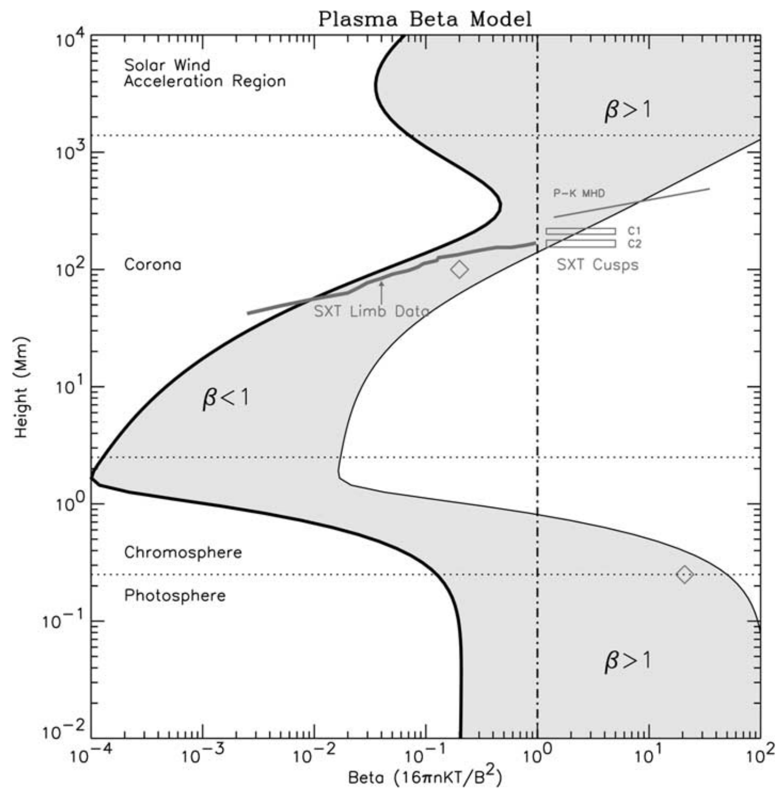

Figure 2.1: Plasma β variation in the solar atmosphere over an active region from Gary (2001).

mosphere, $\beta << 1$, which indicates that the Lorentz force is large compared to both plasma pressure gradient as well as gravitational force terms in Equation 2.5. Consequently, $\bar{\mathbf{J}} \times \bar{\mathbf{B}} = 0$, which implies that the force-free approximation is satisfied. Force-free assumption leads to two cases: either the current density $\mathbf{J}$ is zero (potential field) or the current density $\mathbf{J}$ is parallel to the magnetic field $\mathbf{B}$ (linear and nonlinear force-free fields). The solutions to force-free equations are discussed as follows.

2.2.1.1 Potential field

The easiest solution to $\mathbf{J} \times \mathbf{B} = 0$ is the current-free ($\mathbf{J} = 0$) magnetic field which is also known as the potential field. The current-free magnetic field, i.e., $\nabla \times \mathbf{B} = 0$, can be expressed as $\mathbf{B} = -\nabla \chi$ where χ is the scalar potential. The solenoidal condition $\nabla \cdot \mathbf{B} = 0$ leads to the partial differential equation (PDE), $\nabla^2 \chi = 0$— the Laplace equation. Imposing Neumann boundary condition, i.e., the normal component of the magnetic field $\left(\dfrac{\partial \chi}{\partial n} = B_n\right)$ on the boundary of an enclosed volume leads to an unique solution of the PDE. It can be readily visualized that the magnetic energy, $W = \int \frac{B^2}{2\mu_o} dV$ associated with the potential fields is the smallest. The magnetic energy of the non-potential magnetic fields ($\mathbf{J} \neq 0$) with the same B_n on the boundary is more than that of the potential fields (Priest, 2014). This holds good for a semi-infinite region, assuming no sources at infinity so that the magnetic field at the large distances R falls of faster than R^{-2}. A good example of such system is the solar atmosphere above the photosphere where the normal field at the photosphere (line-of-sight component) is known, thus potential field extrapolations require only the line-of-sight magnetic field data.

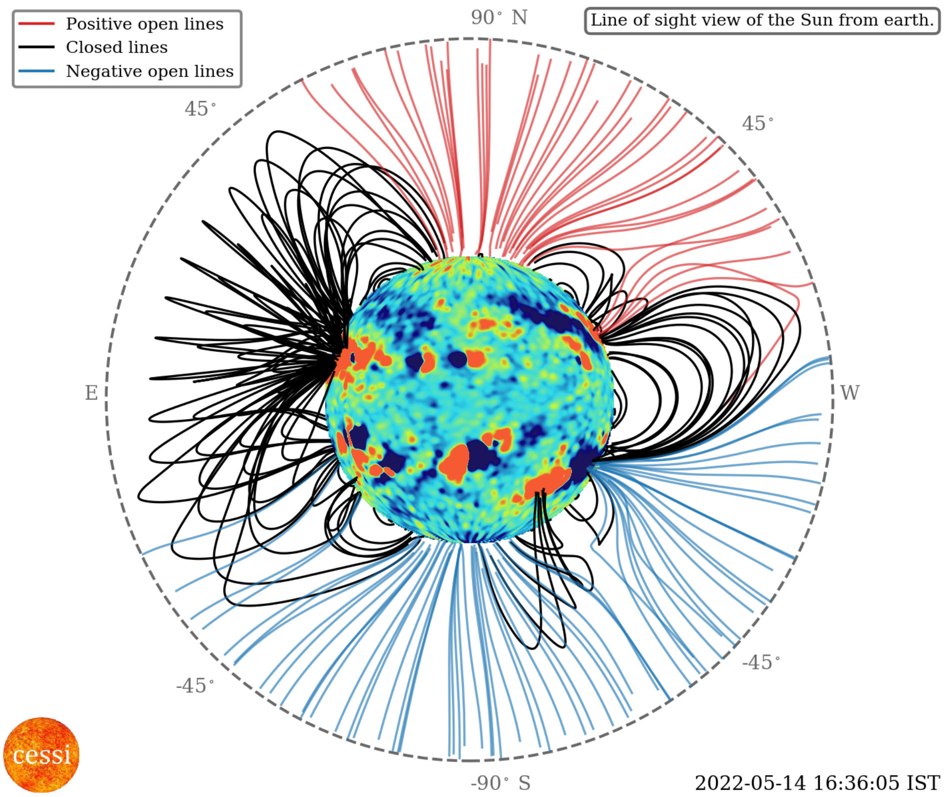

Figure 2.2: PFSS modeled magnetic field configuration of the Sun. Image courtesy: http://www.cessi.in/spaceweather/images/big/ori_corona_logo.png

A simplified but popular extrapolation model based on the current-free field approximation is known as the Potential Field Source Surface (PFSS) model. PFSS computes the magnetic field in the region bounded between photosphere and an outer "source surface", i.e. between $R_\odot \leq r \leq R_s$ where $R_\odot$ is the radius of Sun and R_s is the distance of the source surface from photosphere. The boundary conditions are imposed at R_s, and this is the only single free parameter in the PFSS model. Value of R_s is usually decided in accordance with either the observations of white-light corona, coronal hole boundaries (in X-ray) or through the extrapolations from in situ interplanetary magnetic field (IMF) observations. Generally adopted value of R_s is equals to $2.5R_\odot$ but it can vary with the temporal variation of magnetic activity (Lee et al., 2011). Although the PFSS models are helpful in reconstructing the large-scale global structures in the corona but it has two major limitations: First, the transient phenomena can not be explained using PFSS due to its current-free nature since it does not account for the twist which plays a crucial role in coronal transients, and second is that actual coronal magnetic field is not entirely radial within the radius where electric currents may be ignored. Figure 2.2 shows an example of the magnetic field configuration obtained using the PFSS model.

2.2.1.2 Linear force-free

A simplest scenario for the force-free approximation ($\mathbf{J} \times \mathbf{B} = 0$) follows by considering non-zero current density. This is possible if current density is taken parallel to the magnetic field, satisfying the following relation

$$\mathbf{J} = \alpha_0 \mathbf{B} \quad \text{or} \quad \nabla \times \mathbf{B} = \alpha_0 \mathbf{B} \tag{2.6}$$

where α_0 is a constant representing twist of magnetic field lines. If, we consider the curl of Equation 2.6 and use the condition that $\nabla \cdot \mathbf{B} = 0$, we obtain the following vector Helmholtz equation

$$(\nabla^2 + \alpha_0^2)\mathbf{B} = 0 \tag{2.7}$$

The theoretical and mathematical aspects of Equation 2.7 have been explored in earlier works such as Chandrasekhar & Kendall (1957) and Woltjer (1958). Further, the solution techniques for the determination of linear force-free field (LFFF) have been investigated in several previous works such as Nakagawa & Raadu (1972), followed by Chiu & Hilton (1977) and Seehafer (1978) using Green's function approach and by Alissandrakis (1981) employing the method of Fast Fourier transforms. Generally, linear force-free field extrapolation requires transverse field components in addition to the line-of-sight magnetogram for unique solution (Gary, 1989). However, in special cases, using only line-of-sight magnetogram along with the estimation of α_0 provides physically realizable solutions. One of the methods for estimating α_0 utilizes the vector magnetic field data (in Cartesian coordinate) as

$$\alpha_0(x, y) = \mu_0 \frac{{J_z}^0}{{B_z}^0} \,, \tag{2.8}$$

where

$${J_z}^0 = \frac{\partial {B_y}^0}{\partial x} - \frac{\partial {B_x}^0}{\partial y} \tag{2.9}$$

Though the linear force-free fields contain more energy than the potential magnetic field (Sakurai, 1981), their application to active region dynamics is limited. The reasoning behind this is the spatially varying α_0 in observations which contradicts the assumption of a constant α_0 force-free field. Additionally, due to continuous injection of helicity from photospheric surface, the magnetic field cannot relax to a linear force-free field (Wiegelmann & Sakurai, 2021). Therefore, the necessity of nonliear force-free fields cannot be overlooked, which we will now discuss in the following section.

2.2.1.3 Nonlinear force-free

Having discussed the case of constant α force-free field and it's limitations, now we consider the case where α is a function of position vector $\mathbf{r}$, satisfying the equation

$$\nabla \times \mathbf{B} = \alpha(\mathbf{r})\mathbf{B} \tag{2.10}$$

Using solenoidality and taking divergence on both sides of Equation 2.10, we see that

$$\nabla\alpha.\mathbf{B} = 0 \tag{2.11}$$

which suggests that along each particular field line, the value of α is a constant but can vary among the field lines. Previous works such as Bineau (1972) and Amari et al. (2006) have explored the mathematical structure of Equation 2.10 regarding uniqueness and existence of solutions. In the past two decades, several techniques have been developed to obtain a nonlinear force-free field such as the upward integration method (Nakagawa, 1974), the Grad-Rubin method (Sakurai, 1981, Amari et al., 1997 and Amari & Aly, 2010) and the optimization approach (Wheatland et al., 2000 and Wiegelmann, 2004). In general, the problem is challenging due to intrinsic nonlinearity of the problem and the fact that transverse components of magnetic field are required on photosphere, which have more error compared to the line-of-sight field. Further, it should be emphasized that the photospheric boundary is not force-free, which contradicts Equation 2.10. To deal with this, particularly within the optimization approach, routines have been developed which artificially process the bottom boundary to make it compatible with the force-free assumption (e.g. Wiegelmann et al., 2006a) while ensuring that the changes are within the limit of measurement errors. Similarly, additional effort has been directed to deal with regions of lacking observational data in the vector magnetograms (Wiegelmann & Inhester, 2010). Due to existence of several methods to obtain nonlinear force-free fields, many studies such as Schrijver et al. (2006) and De Rosa et al. (2009) have presented a comparative study of models, highlighting the differences and similarities. The nonlinear force-free model has been widely accepted as suitable for modeling of active region dynamics. The success is due to adequate accounting of twisted magnetic field lines and the free magnetic energy, which is thought to be released during transient phenomenon such as flares. A comapartively newer and alternate model to nonlinear modeling is the non force-free model, which we now discuss in the next section.

2.2.2 Non force-free model

As discussed previously, the observed vector magnetograms do not satisfy the force-free assumption. Therefore, a non force-free model where the Lorentz force i.e. $\mathbf{J} \times \mathbf{B} \neq 0$ on the photospheric boundary but decreases with height, becoming force-free at coronal heights would be an apt choice for modeling of magnetic fields in the solar atmosphere. The model that we are going to discuss in this section is based on the principle of Minimum Dissipation Rate (MDR) hypothesis (see Bhattacharyya & Janaki, 2004 and reference therein for details). The fundamental idea behind MDR principle is that during an irreversible process, any system naturally evolves to those states (or relaxed states) in which energy dissipation rate is minimum. In the context of coronal plasma, one can apply the MDR principle in the framework of single fluid MHD as well as two fluid formalism. However, the two fluid formulation is preferred due to the natural flow-field coupling and the inherent generality over single fluid MHD description. Further, to avoid the loss of relaxed state in time, we also need to take into account the fact that the solar corona is an open system and is continuously driven by photospheric motions. Toward such an aim, in accordance with the selective decay principle (Hasegawa, 1985), by chosing total dissipation rate (ohmic and viscous) as the minimizer and generalized helicty dissipation rates (for ion and electron fluid) as invariants, Bhattacharyya & Janaki (2004) applied the MDR priciple to obtain the corresponding relaxed state, represented by an inhomogenous double-curl Beltrami equation as

$$\nabla \times (\nabla \times \mathbf{B}) + a\nabla \times \mathbf{B} + b\mathbf{B} = \nabla\phi \tag{2.12}$$

where a and b are constants and ϕ is a scalar potential. The application of this idea in solar coronal context was to model coronal arcades as minimum dissipative relaxed states (Bhattacharyya et al., 2007). Notice that Equation 2.12 can be recasted into a homogenous equation either by taking curl on both sides, which gives

$$\nabla \times [\nabla \times (\nabla \times \mathbf{B})] + a\nabla \times (\nabla \times \mathbf{B}) + b\nabla \times \mathbf{B} = 0 \tag{2.13}$$

or be redefining the magnetic field vector as $\mathbf{B} = \mathbf{B}' + \dfrac{\nabla\phi}{b}$, which gives

$$\nabla \times (\nabla \times \mathbf{B}') + a\nabla \times \mathbf{B}' + b\mathbf{B}' = 0 \tag{2.14}$$

In principle, Equation 2.13 and Equation 2.14 are equivalent. This can be seen by looking at the form of solution for Equation 2.13, given by

$$\mathbf{B} = \sum_{i=1}^{3} \mathbf{B}_i \tag{2.15}$$

where $\mathbf{B}_i$ are the linear force-free Chandrasekhar-Kendall eigenfunctions (Chandrasekhar & Kendall, 1957), satisfying the relations

$$\nabla \times \mathbf{B}_i = \alpha_i \mathbf{B}_i \tag{2.16}$$

where α_i are the constant twists and $\mathbf{B}_i$ form a complete set of orthonormal vectors for real eigenvalues (Yoshida & Giga, 1990). Using Equation 2.15 and Equation 2.16 in Equation 2.13, we have

$$\sum_{i=1}^{2} \alpha_i \left[\alpha_i^2 + a\alpha_i + b\right] \mathbf{B}_i = 0 \tag{2.17}$$

which suggests that one of the $\alpha_i = 0$, thus corresponding to a potential field. Since, $(\nabla\phi)/b$ is also a potential field, the equivalency is established. For more details, see Hu & Dasgupta (2008). Therefore, a superposition of two linear force-free fields with a potential magnetic field gives the required non force-free solution. A practical approach toward obtaining such a solution in the case of solar corona has been outlined in Hu et al. (2010). The stepwise methodology and procedure is described in detail as follows

Step-1 : Construction of the Vandermonde matrix

Consider Equation 2.15, then by taking additional curl operations, we have the following set of three equations

$$\mathbf{B} = \mathbf{B}_1 + \mathbf{B}_2 + \mathbf{B}_3 \tag{2.18}$$

$$\nabla \times \mathbf{B} = \alpha_1\mathbf{B}_1 + \alpha_2\mathbf{B}_2 + \alpha_3\mathbf{B}_3 \tag{2.19}$$

$$\nabla \times (\nabla \times \mathbf{B}) = \alpha_1^2\mathbf{B}_1 + \alpha_2^2\mathbf{B}_2 + \alpha_3^2\mathbf{B}_3 \tag{2.20}$$

which can be transformed into a matrix form as follows

$$\begin{pmatrix} \mathbf{B} \\ \nabla \times \mathbf{B} \\ \nabla \times (\nabla \times \mathbf{B}) \end{pmatrix} = \begin{pmatrix} 1 & 1 & 1 \\ \alpha_1 & \alpha_2 & \alpha_3 \\ \alpha_1^2 & \alpha_2^2 & \alpha_3^2 \end{pmatrix} \begin{pmatrix} \mathbf{B}_1 \\ \mathbf{B}_2 \\ \mathbf{B}_3 \end{pmatrix} = \mathcal{V} \begin{pmatrix} \mathbf{B}_1 \\ \mathbf{B}_2 \\ \mathbf{B}_3 \end{pmatrix}$$

where $\mathcal{V}$ is said to be the Vandermonde matrix. Now, the constituent fields may be expressed as

$$\begin{pmatrix} \mathbf{B}_1 \\ \mathbf{B}_2 \\ \mathbf{B}_3 \end{pmatrix} = \mathcal{V}^{-1} \begin{pmatrix} \mathbf{B} \\ \nabla \times \mathbf{B} \\ \nabla \times (\nabla \times \mathbf{B}) \end{pmatrix} \tag{2.21}$$

Step-2 : Obtain the z component of constitutent fields using the observed line-of-sight magnetogram

As evident from the term $\nabla \times (\nabla \times \mathbf{B})$ in the righthand column of Equation 2.21, double derivatives are required for calculation. In the context of solar corona, this translates into the requirement of two layers of magnetogram in the solar atmosphere. This criterion is not often met because routine observations of magnetic field are available only for photosphere and hence only one layer of magnetogram is possible. In order to get around this problem, Hu et al. (2008) introduced the following decomposition

$$\mathbf{B} = \mathbf{B}_1 + \mathbf{B}_2 + c\mathbf{B}_{\text{pot}} \tag{2.22}$$

where $\mathbf{B}_1$ and $\mathbf{B}_2$ are linear force-free fields, $\mathbf{B}_{\text{pot}}$ is a potential magnetic field obtained using the line-of-sight magnetogram and c is an undetermined multiplier. Then, the z components of $\mathbf{B}_1$ and $\mathbf{B}_2$ can be obtained by taking curl of Equation 2.22, as follows

$$\begin{aligned}
(\nabla \times \mathbf{B})_z &= \alpha_1 \mathbf{B}_{1,z} + \alpha_2 \mathbf{B}_{2,z} \\
(\nabla \times \mathbf{B})_z &= \alpha_1 \mathbf{B}_{1,z} + \alpha_2 (\mathbf{B}_z - \mathbf{B}_{1,z} - c\mathbf{B}_{\text{pot,z}}) \\
\mathbf{B}_{1,z} &= \frac{1}{\alpha_1 - \alpha_2} [(\nabla \times \mathbf{B})_z - \alpha_2 \mathbf{B}_z + \alpha_2 c \mathbf{B}_{\text{pot,z}}] \qquad (2.23) \\
\mathbf{B}_{2,z} &= \frac{1}{\alpha_2 - \alpha_1} [(\nabla \times \mathbf{B})_z - \alpha_1 \mathbf{B}_z + \alpha_1 c \mathbf{B}_{\text{pot,z}}] \qquad (2.24)
\end{aligned}$$

Step-3 : Computation of transverse components of constituent fields and minimization of error

Having obtained the z components, we require the transverse fields i.e. the x and y components for complete specification of the modeled field. For an initial choice of α_1, α_2 and c, Equation 2.24 and Equation 2.24 are solved. Then using a linear force-free solver, transverse components i.e. $\mathbf{B}_{1,x}$, $\mathbf{B}_{1,y}$ and $\mathbf{B}_{2,x}$, $\mathbf{B}_{2,y}$ are obtained. Now, denoting the modeled field as $\mathbf{b} = \mathbf{B}_1 + \mathbf{B}_2 + c\mathbf{B}_{\text{pot}}$, the deviation between the modeled and observed magnetic field is evaluated by computing E_n, defined as

$$E_n = \sum_{i=1}^{M} \left(|\mathbf{B}_{t,i} - \mathbf{b}_{t,i}| \times |\mathbf{B}_{t,i}|\right) / \sum_{i=1}^{M} |\mathbf{B}_{t,i}| \tag{2.25}$$

By varying the possible values of α_1, α_2 and c (see Hu & Dasgupta, 2008 for details), the process of calculating z components, followed by computation of transverse components and E_n is repeated unti a minimum is obtained in the error. This state of minimum error corresponds to the optimized pair (α_1, α_2) and c. Hence, in principe, the non force-free field in solar atmosphere is obtained. However, further improvement was introduced by Hu et al. (2010) as described in the nest step.

Step-4 : Improvements in the modeled field as described by Hu et al. (2010)

Considering the fact that the sum of potential fields is a potential field, Hu et al. (2010) proposed to modeify the potential field $\mathbf{B}_2$ as

$$\mathbf{B}_2 = c\mathbf{B}_{\text{pot}} + \mathbf{B}_2^{(1)} + \mathbf{B}_2^{(2)} + ... + \mathbf{B}_2^{(k)} + ... \tag{2.26}$$

where $\mathbf{B}_2^{(k)}$ are iterative improvements of $\mathbf{B}_2$. Note that $\mathbf{B}_2^{(0)} = c\mathbf{B}_{\text{pot}}$. Now, to calculate $\mathbf{B}_2^{(k)}$, first, a difference in transverse components of modeled and observed field is computed as

$$\triangle\mathbf{b}_t = \mathbf{B}_t - \mathbf{b}_t$$

Then, the z component of $\mathbf{B}_2^{(k)}$ is computed (Venkatakrishnan & Gary, 1989) as

$$\mathbf{B}_{2,z}^{(k)} = \mathcal{F}^{-1}\left[\frac{iv\mathcal{F}(\triangle\mathbf{b}_y) + iu\mathcal{F}(\triangle\mathbf{b}_x)}{\sqrt{(u^2+v^2)}}\right] \tag{2.27}$$

where $\mathcal{F}(\mathcal{F}^{-1})$ denote the Fourier(inverse Fourier) transforms with u and v as frequency domain variables. Having obtained z components, transverse component of $\mathbf{B}_2^{(k)}$ can be obtained easily using Fast Fourier Transforms. Now, in an iterative scheme, $\mathbf{B}_2$ is improved and E_n is evaluated until an acceptable minimum is achieved. The number of iterations can be set manually until the profile of E_n saturates and no significant change is observed further.

2.3 Coronal Transient Observations

The coronal magnetic field extrapolation models described in the previous sections use observations of magnetic field vector at the photoshere as input. Further, multi-wavelength observatios of the Sun such as in X-ray and EUV wavelength ranges allow us to study the temporal evolution of a transient activity at various heights in the solar atmosphere. The simulataneous use of multiwavelength observations and magnetic field provide a complete data set for effective analysis of any transient activity. Toward such an aim, we have extensively used the observations from a space-based satellite, namely the Solar Dynamics Observatory (SDO).

2.3.1 Solar Dynamic Observatory (SDO)

The Solar Dynamics Observatory (SDO; Pesnell et al., 2012a) mission was launched on 11 February, 2010 and it was the first space based mission comissioned under the Living With a Star (LWS) program of NASA. The satellite is placed in a circular geosynchronous orbit, at an approximate altitude of 36,000 km and an inclination of 28°. The primary objective of this mission is to investigate the magnetic field of Sun, it's generation, evolution and role in transient activities such as solar flares and coronal mass ejections. Toward such an aim, it transmits nearly $\sim$ 1.5 Terabytes of data every day to the ground staion, which is later processed into various data products such as Dopplergrams, magnetograms and spectra. Primarily, it consists of three instruments, namely the Atmospheric Imaging Assembly (AIA), Extreme Ultraviolet Variability Experiment (EVE) and the Helioseismic Magnetic Imager (HMI). In this thesis, we have used observations from AIA and HMI, which we discuss in the following.

2.3.1.1 Atmospheric Imaging Assembly (AIA)

The Atmospheric Imaging Assembly (AIA: Lemen et al., 2012) observes the full-disk Sun in multiple wavelengths channels. It provides multiple and simultaneous

Channel	Primary ion(s)	Region of atmosphere	Char. log(T)
4500 Å	continuum	photosphere	3.7
1700 Å	continuum	photosphere	3.7
304 Å	He II	chromosphere, transition region	4.7
1600 Å	C IV + continuum	transition region, upper photosphere	5.0
171 Å	Fe IX	quite corona, upper transition region	5.8
193 Å	Fe XII, XXIV	corona and hot flare plasma	6.2, 7.3
211 Å	Fe XIV	active-region corona	6.3
335 Å	Fe XVI	active-region corona	6.4
94 Å	Fe XVIII	flaring corona	6.8
131 Å	Fe VIII, XXI	transition region, flaring corona	5.6,7.0

Table 2.1: Different channels of AIA centered on specific lines and corresponding regions of solar atmosphere with different characteristic temperatures (Lemen et al., 2012)

high-resolution images of the solar corona and transition region up to 0.5 $R_\odot$ above the solar limb with $0.6''$ pixel^{-1} spatial resolution and 12-second temporal resolution. Normal incidence and multi-layer coated optics based telescopes of AIA allow narrow-band imaging in seven EUV channels, as summarized in Table 2.1. For each line, it describes the corresponding ion and region of the solar atmosphere, with characteristic temperature in log scale. In this thesis, we have used the AIA images to understand the evolution of flaring activity in active region NOAA 12734, to identify salient features of the transient activity at different heights, and to correlate the observations with data-based MHD and HMHD simulations. Particularly, we have used the 94 Å to study the evolution of hot plasma in flare and to identify the location of flare. We have used 171 Å to identify post flare loops and coronal loops in general. Other channels such as 131 Å and 304 Å have been used to define a W-shaped brightening (see Chapter 6) in the active rgion, which describes the overall geometry of the flaring region.

2.3.1.2 The Helioseismic and Magnetic Imager (HMI)

The Helioseismic Magnetic Imager (HMI; Scherrer et al., 2012) instrument onboard SDO began operations from May, 2010 and since then, it has been observing the Sun's entire visible disk continuously. Essentially, it has three components - optics package, electronic box and a harness to connect the two (for details, see Schou et al., 2012). Broadly speaking, the HMI data is categorized into three levels

(a) Level 0 - raw HMI images (b) Level 1 - data from Level 0 at a particular wavelength and polarization, which has been corrected for various instrumental effects and (c) Level 1.5 - the HMI observables, computed using Level 1 data (Couvidat et al., 2016). Further, some higher-level data products such as vector magnetic field maps (Hoeksema et al., 2014) and active region patches (Bobra et al., 2014) are also produced. The HMI instrument acquires a series of polarized filtergrams at fixed cadence, using six wavelengths, centered on the Fe I spectral line (6173 Å). These observations are accomplished with the help of two cameras, each of which take full-disk images at roughly 3.75 seconds and have 4096 $\times$ 4096 pixels along the x and y directions. Further, using two different processing pipelines (a) LoS Pipeline and (b) Vector Pipeline, the filtergrams are utilized to compute various observables corresponding to the photopsheric surface. The LoS pipeline uses filtergrams (left or right circular polarization) from the HMI front camera to compute the Dopplergrams, magnetograms and continuum intensity at a cadence of 45 seconds in definite and near real time modes. On the other hand, the Vector Pipeline uses filtergrams (linear and circular polarization) from the side camera to primarily compute the Stokes-vector elements, supplemented with line-of-sight Dopplergrams, magnetograms and continuum intensity, all at cadence of 12 minutes (Couvidat et al., 2016). In this thesis, we have used the SHARP (Bobra et al., 2014) data series from HMI to obtain the vector magnetic field corresponding to the photospheric surface for active region NOAA 12734. It provides the magnetic field in a Cartesian coordinate system, which has been used as bottom boundary to perform magnetic field extrapolation.

2.4 Summary

In this Chapter, we have discussed the importance of solar observations to understand transient activities, such as solar flares and coronal mass ejections. The multi-wavelength imaging data from SDO/AIA and photospheric vector magnetic field measurements from SDO/HMI have been used to explore the C1.3 class solar flare in active region NOAA 12734, using data-constrained MHD and HMHD simulations (more details in Chapter 6). In this regard, we have briefly mentioned the details and working of the aforementioned instruments, along with the data acquired from them. We have also emphasized on the fact that since routine observations of magnetic field are available for photopshere only, extrapolation models are needed to obtain the magnetic field topology in solar corona. Such models are broadly categorized into force-free and nonforce-free models depending on whether they allow a zero or non-zero Lorentz force. Within the category of zero Lorentz force, three solutions are possible, namely (a) Potential field (b) Linear force-free field and (c) Non linear force-free field. The three solutions differ with respect to the force-free parameter (α), zero in Potential field model, constant throughout the computational domain for LFFF model and variable but constant for each individual field line in the NLFFF model. We have also discussed the theoretical and numerical aspects of the non force-free model, which is based on the Minimum Dissipation Rate principle. We conclude this chapter with the idea that multi wavelength observations and magnetic field measurements (for magnetic field extrapolation) are an essential tool for exploration and understanding of transient activities, which are in turn a consequence of magnetic reconnection.

Chapter 3

Numerical model

3.1 Introduction

As mentioned in Chapter 1, to fulfill the aim of this as a first step we develop a 3D HMHD* solver. Therefore, in this Chapter, we document the advancement of an already well-established MHD model to include Hall effects. A numerical model consistent with physics of astrophysical plasma must accurately preserve the flux-freezing by minimizing numerical dissipation and dispersion errors away from the reconnection regions characterized by steep gradients of the magnetic field (Bhattacharyya et al., 2010). Such minimization is a signature of a class of inherently nonlinear transport methods that preserve field extrema along flow trajectories, while ensuring higher-order accuracy away from steep gradients in advected fields. As discussed in Section 1.6, the Hall forcing term is only effective and localized to the regions of steep gradients of magnetic field. Consequently, we incorporate the Hall forcing in the established high-resolution EULAG-MHD model (Smolarkiewicz & Charbonneau, 2013; Charbonneau & Smolarkiewicz, 2013), a specialized version of the general-purpose hydrodynamic model EULAG predominantly used in atmospheric and climate research (Prusa et al., 2008). Central to the EULAG is the spatio-temporally second-order-accurate nonoscillatory forward-in-time (NFT) advection scheme MPDATA, a.k.a Multidimensional Positive Definite Advection Transport Algorithm, (Smolarkiewicz, 2006). MPDATA mimics the action of explicit subgrid-scale turbulence models. It has proven effectiveness

*Everywhere in this thesis the acronym HMHD is used for model name.

in generating an intermittent and adaptive residual dissipation whenever the concerned advective field is under-resolved—a property inherent to implicit large eddy simulations (ILES) (Grinstein et al., 2007). The generation of steep gradients of magnetic field in absence of magnetic diffusion provides an unbound sharpening of the corresponding field gradient and inevitably generates under-resolved scales. The unbound increase in field gradient is then smoothed out by this MPDATA produced locally effective residual dissipation of the second order, sufficient to sustain the monotonic nature of the solution. Consequently, the physical reconnections are mimicked at locations of maximal gradients by ILES property of MPDATA. The ILES property of MPDATA has proven instrumental in a series of advanced numerical studies across a range of scales and physical scenarios, including studies related to the coronal heating along with data-based simulations of solar transients (Bhattacharyya et al., 2010; Kumar & Bhattacharyya, 2011; Kumar et al., 2015b, 2017; Prasad et al., 2017, 2018; Nayak et al., 2019, 2020). Our development of a 3D HMHD solver benefits from the ILES property of MPDATA where we have tied the Hall term with dissipation scale so that the increased local gradients cause the Hall term to be effective locally.

In this Chapter, we present the important features of advection scheme MPDATA in Section 3.2, numerics of EULAG MHD and the advancement to include Hall forcing term in Section 3.3, and ILES property of MPDATA in Section 3.4.

3.2 Advection solver MPDATA scheme

MPDATA (Smolarkiewicz, 1983, 1984; Smolarkiewicz & Clark, 1986), a finite difference scheme, was originally designed by P. K. Smolarkiewicz in the early 1980's. The algorithm is at least second-order accurate, positive definite, conservative, and computationally efficient. The iterative use of upstream or upwind schemes allow for the second order accuracy in MPDATA, where the first iteration is simply a donor cell differencing. Subsequently, the MPDATA algorithm improves the accuracy of solution by compensating the truncation error, obtained in the second iteration. In a similar fashion, further iterations may be executed to deal with the residual errors, resulting from previous iterations, which further enhance the accuracy. In the past decades, MPDATA has been extended to accommodate curvilinear coordinates, full monotonicity preservation, third-order accuracy and variable sign fields; for details cf. reviews Smolarkiewicz & Margolin (1998); Smolarkiewicz (2006). Here, by using Cartesian coordinates. we discuss the fundamental concepts underlying MPDATA design.

3.2.1 Derivation of MPDATA

To fix ideas, we consider a simple one-dimensional advection equation,

$$\frac{\partial \varphi}{\partial t} + \frac{\partial (k\varphi)}{\partial x} = 0, \tag{3.1}$$

for a scalar variable φ. The velocity k may also be a function of space and time. The donor cell discretization of the advection equation is given by,

$$\varphi_i^{n+1} = \varphi_i^n - \frac{\delta t}{\delta x}(k_{i+\frac{1}{2}}\varphi_r^n - k_{i-\frac{1}{2}}\varphi_l^n), \tag{3.2}$$

where φ_r^n and φ_l^n are chosen depending on the sign of $k_{i+\frac{1}{2}}$ and $k_{i-\frac{1}{2}}$:

$$\varphi_r^n = \begin{cases} \varphi_i^n, & k_{i+\frac{1}{2}} > 0, \\ \varphi_{i+1}^n, & k_{i+\frac{1}{2}} < 0, \end{cases} \tag{3.3}$$

and

$$\varphi_l^n = \begin{cases} \varphi_{i-1}^n, & k_{i-\frac{1}{2}} > 0, \\ \varphi_i^n, & k_{i-\frac{1}{2}} < 0, \end{cases} \tag{3.4}$$

with the integer and half-integer indices correspond to cell centers and cell walls. In Equation 3.2, φ_i^{n+1} on the LHS is the solution sought at the grid point (t^{n+1}, x_i) with $\delta t = t^{n+1} - t^n$ and $\delta x = x_{i+1} - x_i$ representing temporal and spatial increments respectively. The above case distinctions can be avoided by writing the Equation 3.2 in the following form,

$$\varphi_i^{n+1} = \varphi_i^n - \frac{\delta t}{2\delta x}[k_{i+\frac{1}{2}}(\varphi_i^n + \varphi_{i+1}^n) - k_{i-\frac{1}{2}}(\varphi_{i-1}^n + \varphi_i^n) \\ + \mid k_{i+\frac{1}{2}} \mid (\varphi_i^n - \varphi_{i+1}^n) - \mid k_{i-\frac{1}{2}} \mid (\varphi_{i-1}^n - \varphi_i^n)]. \tag{3.5}$$

Notably, if the sign of k determines the flow direction, this scheme always chooses the values of φ (for a given time) which lies in the upstream direction (Griebel et al., 1998). The donor cell approximation in flux form is expressed as,

$$\varphi_i^{n+1} = \varphi_i^n - [F(\varphi_i^n, \varphi_{i+1}^n, U_{i+\frac{1}{2}}) - F(\varphi_{i-1}^n, \varphi_i^n, U_{i-\frac{1}{2}})], \tag{3.6}$$

where the flux function F is

$$F(\varphi_L, \varphi_R, U) \equiv [U]^+\varphi_L + [U]^-\varphi_R, \tag{3.7}$$

with $U \equiv \dfrac{a\delta t}{\delta x}$ represents the dimensionless local Courant number while, $[U]^+ \equiv 0.5(U + \mid U \mid)$ and $[U]^- \equiv 0.5(U - \mid U \mid)$ denoting the nonnegative and nonpositive parts of the Courant number (Smolarkiewicz & Margolin, 1998; Smolarkiewicz, 2006).

The donor cell scheme is conditionally stable and the corresponding stability condition, for every time step, has a form

$$\max\left(\frac{\mid k_{i+\frac{1}{2}} \mid \delta t}{\delta x}\right) \leq 1 \quad \forall i. \tag{3.8}$$

Moreover, under the condition Equation 3.8, the scheme is also positive definite, implying: if $\varphi_i^0 \geq 0 \quad \forall i$ then $\varphi_i^n \geq 0 \quad \forall i$ and n. These two properties as well as low computational cost and low phase error make the scheme Equation 3.6 attractive for the numerical evaluation of the advection equation. However, the scheme being first-order accurate (both in space and time) produces large implicit numerical diffusion.

Towards quantifying the diffusion in Equation 3.6, for simplicity we assume the k to be constant and φ to be nonnegative. A straightforward truncation analysis, expanding all dependent variables in a second-order Taylor series about the time level n and spatial point i, reveals that the scheme more accurately approximates the advection-diffusion equation

$$\frac{\partial \varphi}{\partial t} + \frac{\partial (k\varphi)}{\partial x} = \frac{\partial}{\partial x}\left(K\frac{\partial \varphi}{\partial x}\right), \tag{3.9}$$

where the diffusion coefficient

$$K = \frac{\delta x^2}{2\delta t}(\mid U \mid - U^2). \tag{3.10}$$

In other words, the scheme estimates the solution of the advection equation with a second-order truncation error. To enhance the accuracy, it is necessary to construct a numerical estimate of the error and subtract it from Equation 3.6. The basic strategy, fundamental to all MPDATA schemes, is then to once again utilize a donor cell approximation to calculate the error term in order to preserve the properties of donor cell scheme. To do so, the error term, the right hand side term of Equation 3.9, is rewritten as

$$e^1 \equiv \frac{\partial}{\partial x}\left(K\frac{\partial \varphi}{\partial x}\right) = \frac{\partial (k^1 \varphi)}{\partial x}, \tag{3.11}$$

where e^1 symbolizes error term and $k^1 \equiv \dfrac{K}{\varphi}\dfrac{\partial \varphi}{\partial x}$ is ~~termed as~~ pseudo velocity. The superscript (1) is used to mark the first iteration for subtracting the error. To compensate the error, we again use the donor cell scheme but this time with the pseudo velocity k^1 and the φ^{n+1} already available from Equation 3.6 in lieu of the physical velocity k and the φ^n. A first-order accurate estimate of the pseudo velocity is

$$k^1_{i+\frac{1}{2}} \equiv \frac{2K}{\delta x}\frac{\varphi^{(1)}_{i+1} - \varphi^{(1)}_i}{\varphi^{(1)}_{i+1} + \varphi^{(1)}_i} \tag{3.12}$$

where $\varphi^{(1)}$ represents the first-order accurate φ^{n+1} estimated from Equation 3.6. The modified Courant number is $V^1_{i+\frac{1}{2}} \equiv \dfrac{k^1_{i+\frac{1}{2}}\delta t}{\delta x}$. In the second iteration, we subtract a donor cell estimate of the error to improve the accuracy. The equation of the second iteration is

$$\varphi^2_i = \varphi^1_i - [F(\varphi^1_i, \varphi^1_{i+1}, V^1_{i+\frac{1}{2}}) - F(\varphi^1_{i-1}, \varphi^1_i, V^1_{i-\frac{1}{2}})], \tag{3.13}$$

which estimates φ^{n+1} which is the second-order accurate while preserving the sign of φ. It is an easy matter to show that, like the donor cell scheme, MPDATA is consistent and conditionally stable (Smolarkiewicz, 1983; Smolarkiewicz & Margolin, 1998; Smolarkiewicz, 2006). But, in contrast to the donor scheme, MPDATA does not contain strong numerical implicit diffusion because of the improved accuracy.

The extension of MPDATA to multiple dimension is straightforward. To demonstrate, we consider a simple two-dimensional advection equation,

$$\frac{\partial \varphi}{\partial t} + \frac{\partial (k\varphi)}{\partial x} + \frac{\partial (l\varphi)}{\partial y} = 0, \tag{3.14}$$

where k and l are velocities in x and y directions. The corresponding donor cell approximation is then

$$\begin{aligned}\varphi_{i,j}^{n+1} = \varphi_{i,j}^{n} - [F(\varphi_{i,j}^{n}, \varphi_{i+1,j}^{n}, U_{i+\frac{1}{2},j}) - F(\varphi_{i-1,j}^{n}, \varphi_{i,j}^{n}, U_{i-\frac{1}{2},j})] \\ -[F(\varphi_{i,j}^{n}, \varphi_{i,j+1}^{n}, V_{i,j+\frac{1}{2}}) - F(\varphi_{i,j-1}^{n}, \varphi_{i,j}^{n}, V_{i,j-\frac{1}{2}})],\end{aligned} \tag{3.15}$$

where the flux function is similar to Equation 3.7 and, $U \equiv \dfrac{k\delta t}{\delta x}$ and $V \equiv \dfrac{l\delta t}{\delta y}$ are Courant numbers. Further, the Taylor's series expansion of Equation 3.15 about the cell point (i, j) and the time level n with constant velocities yields the following advection-diffusion equation,

$$\frac{\partial \varphi}{\partial t} + \frac{\partial (k\varphi)}{\partial x} + \frac{\partial (l\varphi)}{\partial y} = K\frac{\partial^2 \varphi}{\partial x^2} + L\frac{\partial^2 \varphi}{\partial y^2} - \frac{UV\delta x \delta y}{\delta t}\frac{\partial^2 \varphi}{\partial x \partial y}, \tag{3.16}$$

with $K \equiv \dfrac{\delta x^2}{2\delta t}(\mid U \mid - U^2)$ and $L \equiv \dfrac{\delta y^2}{2\delta t}(\mid V \mid - V^2)$. To estimate the truncation error using the donor cell scheme, we rewrite the error terms, the right hand side terms of Equation 3.16, in the following form

$$K\frac{\partial^2 \varphi}{\partial x^2} + L\frac{\partial^2 \varphi}{\partial y^2} - \frac{UV\delta x \delta y}{\delta t}\frac{\partial^2 \varphi}{\partial x \partial y} = \frac{\partial}{\partial x}(k^1 \varphi) + \frac{\partial}{\partial x}(l^1 \varphi) \tag{3.17}$$

where

$$k^1 \equiv \frac{K}{\varphi}\frac{\partial \varphi}{\partial x} - \frac{UV\delta x \delta y}{2\delta t}\frac{1}{\varphi}\frac{\partial \varphi}{\partial y} \quad \text{and} \quad l^1 \equiv \frac{L}{\varphi}\frac{\partial \varphi}{\partial y} - \frac{UV\delta x \delta y}{2\delta t}\frac{1}{\varphi}\frac{\partial \varphi}{\partial x} \tag{3.18}$$

are pseudo velocities in x and y directions. Utilizing these velocities and updated value of φ^{n+1} from Equation 3.15, the donor cell scheme is used to estimate the error. In the second iteration, the error is subtracted to enhance the accuracy.

3.2.2 Extension to generalized transport equation

The general transport equation is

$$\frac{\partial \varphi}{\partial t} + \nabla \cdot (\mathbf{k}\varphi) = R, \tag{3.19}$$

where R combines all forcing and source terms. In general, both R and velocity $\mathbf{k}$ depend on variable φ. The forward-in-time discretization of Equation 3.19 is assumed as,

$$\frac{\varphi^{n+1} - \varphi^{n}}{\delta t} + \nabla \cdot (\mathbf{k}^{n+\frac{1}{2}}\varphi^{n}) = R^{n+\frac{1}{2}}. \tag{3.20}$$

Expansion of Equation 3.20 into the second-order Taylor series about the time level n shows that the scheme Equation 3.20 approximates to the equation

$$\frac{\partial \varphi}{\partial t} + \nabla \cdot (\mathbf{k}\varphi) = R - \nabla \cdot \Big[0.5\delta t\mathbf{k}(\mathbf{k} \cdot \nabla\varphi) + 0.5\delta t\mathbf{k}\varphi(\nabla \cdot \mathbf{k})\Big] + \nabla \cdot (0.5\delta t\mathbf{k}R) + \mathcal{O}(\delta t^2). \tag{3.21}$$

In right hand side of Equation 3.21, all $\mathcal{O}(\delta t)$ truncation errors originated by uncentered time differencing in Equation 3.20 are already expressed by spatial derivatives. Specification of the time levels of both the advective velocity and the forcing term as $n + 1/2$ in Equation 3.20 eliminates $\mathcal{O}(\delta t)$ truncation errors which are proportional to their temporal derivatives (Smolarkiewicz & Clark, 1986). From Equation 3.21, it is clear that the formulation of second-order accurate forward-in-time scheme for Equation 3.19 requires the compensation of $\mathcal{O}(\delta t)$ truncation errors to at least the second-order accuracy.

For such a formulation, we note $\mathcal{O}(\delta t)$ error terms in Equation 3.21 have two distinct components. The first component is merely due to advection and does not involve the forcing R. In contrast, the second component depends on the forcing R. Towards compensating the first component, notable is the reduction of Equation 3.19 to homogeneous transport equation for $R = 0$. Then, MPDATA scheme retains the form of the basic scheme (Section 3.2.1) where the first donor cell iteration utilizes the advective velocity $\mathbf{k}^{n+\frac{1}{2}}$ and φ^n, and subsequent iterations use pseudo velocities and φ calculated from the preceding iteration; for details cf. (Smolarkiewicz, 1991; Smolarkiewicz & Margolin, 1993, 1998; Smolarkiewicz, 2006). Compensation of the second component requires subtracting of a first-order accurate approximation of the error from the right hand side of Equation 3.20. A simple, efficient, and second-order accurate MPDATA for Equation 3.19 can then be symbolically written as,

$$\varphi_i^{n+1} = \mathcal{A}_i(\varphi^n + 0.5\delta t R^n, \mathbf{k}^{n+\frac{1}{2}}) + 0.5\delta t R_i^{n+1}, \tag{3.22}$$

where $\mathcal{A}$ denotes the basic MPDATA advection scheme (Smolarkiewicz, 1991; Smolarkiewicz & Margolin, 1993). In this equation, we assume $R^{n+\frac{1}{2}} = 0.5(R^n + R^{n+1})$ with R^{n+1} representing $\mathcal{O}(\delta t^2)$ accurate approximation of R at time level $(n+1)$. Noticeably, first donor cell iteration in the MPDATA scheme uses the auxiliary variable $\varphi^n + 0.5\delta t R^n$ in lieu of the physical variable φ^n with a physical advective velocity $\mathbf{k}^{n+\frac{1}{2}}$. The advection of the auxiliary field is important for preserving the global accuracy and stability of the forward in time approximations (Smolarkiewicz, 1991; Smolarkiewicz & Margolin, 1993, 1997).

The advective velocity at intermediate $n + \frac{1}{2}$ time level may be approximated by linear interpolation or extrapolation

$$\mathbf{k}^{n+\frac{1}{2}} = \frac{1}{2}(\mathbf{k}^{n+1} + \mathbf{k}^n), \tag{3.23}$$

$$\mathbf{k}^{n+\frac{1}{2}} = \frac{1}{2}(3\mathbf{k}^n - \mathbf{k}^{n-1}), \tag{3.24}$$

either of which is sufficient to maintain second-order accuracy in Equation 3.22. For the subtleties involved in a particular choice of $\mathbf{k}^{n+\frac{1}{2}}$, readers are refereed to (Smolarkiewicz & Clark, 1986).

3.2.3 Nonoscillatory MPDATA

The basic MPDATA scheme discussed above preserves sign[†] but not monotonicity of the advected variables (Smolarkiewicz, 1983, 1984; Smolarkiewicz & Clark, 1986) and, in general, the solutions are not free of spurious oscillations particularly in presence of steep gradients (Smolarkiewicz & Grabowski, 1990; Smolarkiewicz, 1991). However, MPDATA is made fully monotone (Smolarkiewicz, 1991) by adapting the flux-corrected-transport (FCT) methodology (Boris & Book, 1973; Book et al., 1975; Boris & Book, 1976). Actually, MPDATA is well suited for this kind of approach for a number of reasons. First, the initial MPDATA iteration is the donor cell scheme—a low-order monotone scheme which is commonly used as the reference in the FCT design. Second, assuring monotonicity of subsequent iterations provides a higher-order accurate reference solution for the next iteration with the effect of improving the overall accuracy of the resulting FCT scheme. Third, since all MPDATA iterations have similar low phase errors characteristic of the donor cell scheme (Smolarkiewicz & Clark, 1986), the FCT procedure mixes solutions with consistent phase errors. This benefits significantly the overall accuracy of the resulting FCT scheme (Smolarkiewicz & Grabowski, 1990).

3.3 Advancement of EULAG-MHD to include Hall forcing

The numerical model EULAG is an established model for simulating fluid flows across a wide range of scales and physical scenarios (Prusa et al., 2008). The name EULAG alludes to the capability to solve the fluid equations in either an Eulerian (Smolarkiewicz & Margolin, 1993) or a Lagrangian (Smolarkiewicz & Pudykiewicz, 1992) mode. The numerics of EULAG are unique, owing to a combination of MPDATA advection schemes, robust elliptic solver, and generalized coordinate formulation enabling grid adaptivity. The EULAG-MHD is a spin-off of the numerical model EULAG (Smolarkiewicz & Charbonneau, 2013). Here, we describe the numerical apparatus of EULAG-MHD utilized for our calculations.

[†]For historical reasons, we refer to this property as positive-definiteness in the previous subsections.

3.3.1 Governing equations of EULAG-MHD

MHD equations (in cgs unit[‡]) for an incompressible magnetofluid with zero physical resistivity (infinite electrical conductivity) are cast in the following form

$$\frac{d\mathbf{v}}{dt} = -\nabla\phi + \frac{1}{4\pi\rho_0}\mathbf{B}\cdot\nabla\mathbf{B} + F_\nu, \tag{3.25}$$

$$\frac{d\mathbf{B}}{dt} = \mathbf{B}\cdot\nabla\mathbf{v}, \tag{3.26}$$

$$\nabla\cdot\mathbf{v} = 0, \tag{3.27}$$

$$\nabla\cdot\mathbf{B} = 0, \tag{3.28}$$

in a non-rotating Cartesian coordinate. The Lagrangian derivative is related the Eulerian derivative in the usual manner

$$\frac{d}{dt} \equiv \frac{\partial}{\partial t} + (\mathbf{v}\cdot\nabla). \tag{3.29}$$

On the right hand side of the momentum transport Equation 3.25, ϕ is a density normalized pressure in which thermodynamic pressure is subsumed to magnetic pressure. F_ν symbolizes the viscous drag force. All other symbols have their usual meaning.

On a general note, EULAG's governing equations are formulated and solved in transformed time-dependent generalized curvilinear coordinates

$$(\bar{t},\bar{\mathbf{x}}) \equiv (t, F(t,\mathbf{x})). \tag{3.30}$$

The physical domain (t,x), where the physical problem is posed, is assumed to be any stationary orthogonal coordinate system (i.e., Cartesian, spherical and cylindrical). Moreover, the transformed horizontal coordinates $(\bar{x},\bar{y})$ are assumed to be independent of the vertical coordinate z (Prusa & Smolarkiewicz, 2003). The calculations carried out in this thesis implement the physical domain to be Cartesian and, therefore both the computational domain and the physical domain are identical, i.e., $(\bar{t},\bar{x}) \equiv (t,x)$. Here, we present the details of the EULAG-MHD for Cartesian domain. The generalized coordinate formulation of EULAG-MHD

[‡]EULAG MHD code uses either cgs or dimensionless units

utilizes the rigorous tensorial exposition of MHD equations; cf. (Smolarkiewicz & Charbonneau, 2013).

3.3.2 Numerics

Utilizing Equation 3.27 and Equation 3.28, the momentum transport Equation 3.25 and the induction Equation 3.26 can be rewritten as,

$$\frac{\partial \mathbf{\Psi}}{\partial t} + \nabla \cdot (\mathbf{v}\mathbf{\Psi}) = \mathbf{R} \tag{3.31}$$

where

$$\mathbf{\Psi} = \{\mathbf{v}, \mathbf{B}\}^T \tag{3.32}$$

represents the vector of dependent variables and

$$\mathbf{R} = \{\mathbf{R_v}, \mathbf{R_B}\}^T \tag{3.33}$$

denotes the right hand side forcing terms in Equation 3.25 and Equation 3.26. Notably, in Equation 3.31, the Lorentz force term of the momentum transport equation and the convective term of the induction equation are cast in the conservative forms via relations,

$$\mathbf{B} \cdot \nabla \mathbf{B} = \nabla \cdot \mathbf{BB}, \qquad \mathbf{B} \cdot \nabla \mathbf{v} = \nabla \cdot \mathbf{Bv}. \tag{3.34}$$

In addition, an ad hoc term $-\nabla\phi^\star$ is added to right hand side of the induction equation, in the spirit of the pressure ϕ in the momentum transport equation, to ensure $\nabla \cdot \mathbf{B} = 0$ in numerical integrations.

The Equation 3.31 is integrated using nonoscillatory forward-in-time algorithm MPDATA. Following Section 3.2.2, an EULAG template algorithm for integration of the Equation 3.31 can be compactly written as,

$$\mathbf{\Psi}_i^{n+1} = \mathcal{A}_i(\mathbf{\Psi}^n + 0.5\delta t\mathbf{R}^n, \mathbf{v}^{n+\frac{1}{2}}) + 0.5\delta t\mathbf{R}_i^{n+1} \equiv \hat{\mathbf{\Psi}}_i + 0.5\delta t\mathbf{R}_i^{n+1}, \tag{3.35}$$

where $\mathbf{\Psi}_i^{n+1}$ is the solution sought at the grid point (t^{n+1}, x_i).

For an inviscid dynamics (F_ν=0), the model template algorithm Equation 3.35 is implicit for all dependent variables in Equation 3.25 and Equation 3.26 because all forcing terms are assumed to be unknown at time level $n+1$. To retain the proven structure of Equation 3.35 for the MHD system, EULAG-MHD template can be viewed as

$$\mathbf{\Psi}_i^{n+1,q} = \hat{\mathbf{\Psi}}_i + \frac{\delta t}{2}\mathbf{L}\mathbf{\Psi} \mid_i^{n+1,q} + \frac{\delta t}{2}\mathbf{N}(\mathbf{\Psi}) \mid_i^{n+1,q-1} - \frac{\delta t}{2}\nabla\mathbf{\Phi} \mid_i^{n+1,q}, \tag{3.36}$$

where the right hand side forcing $\mathbf{R}$ is decomposed into linear term $\mathbf{L\Psi}$ with $\mathbf{L}$ denoting a linear operator, non linear-term $\mathbf{N}(\mathbf{\Psi})$, and potential term $-\nabla\Phi$ with $\Phi \equiv (\phi, \phi, \phi, \phi^\star, \phi^\star, \phi^\star)$. In Equation 3.36, $q = 1, ..., m$ numbers fixed point iterations. The algorithm Equation 3.36 is still implicit with respect to the forcing terms $\mathbf{L\Psi}$ and $-\nabla\Phi$. Using straight-forward algebraic manipulations, the representation Equation 3.36 can be cast into a closed form

$$\mathbf{\Psi}_i^{n+1,q} = [\mathbf{I} - 0.5\delta t\mathbf{L}]^{-1}\left(\hat{\hat{\mathbf{\Psi}}} - 0.5\delta t\nabla\mathbf{\Phi}^{n+1,q}\right)_i, \tag{3.37}$$

where the explicit element is modified to

$$\hat{\hat{\mathbf{\Psi}}} \equiv \hat{\mathbf{\Psi}} + 0.5\delta t\mathbf{N}(\mathbf{\Psi}) \mid^{n+1,q-1}. \tag{3.38}$$

The viscous forcing within this algorithm frame work is incorporated by integrating explicitly to the first-order accuracy in time and then adding to the the auxiliary argument of MPDATA operator $\mathcal{A}$. Now the argument modifies as $\tilde{\mathbf{\Psi}} \equiv \mathbf{\Psi}^n + 0.5\delta t(\mathbf{R}^n + 2\tilde{\mathbf{R}})$ where $\tilde{\mathbf{R}}$ symbolizing the first-order time accurate viscous forcing. All the dependent variables being spatially co-located in Equation 3.37, the time updated $\mathbf{\Psi}$ is obtained by solving two the discrete elliptic equations for ϕ and ϕ^* generated by the solenoidality constraints (Equation 3.27) and Equation 3.28 discretized consistently with the divergence operator implied by $\mathcal{A}$; see (Prusa et al., 2008). Under appropriate boundary conditions, these elliptic equations are solved iteratively using a preconditioned generalized conjugate residual (GCR) algorithm (Eisenstat et al., 1983; Eisenstat, 1983; Smolarkiewicz et al., 1997). Because the GCR is an iterative scheme, to distinguish the iterations appearing in Equation 3.36 and in the GCR solver, the iteration in Equation 3.36 is refereed as "outer", while the iteration corresponds to GCR is termed as "inner". The convergence of the outer iteration is generally controlled by the time step of the model and monitored by the convergence of the inner iteration in the GCR solvers (Smolarkiewicz & Szmelter, 2009, 2011). With the completion of the outer iteration loop, the solution updates and, the total implicit forcing $\mathbf{RI} = \mathbf{L\Psi} - \nabla\Phi$ in Equation 3.36 is returned as $\mathbf{RI}_i^n = \frac{2}{\delta t}(\mathbf{\Psi}_i^n - \hat{\hat{\mathbf{\Psi}}}_i)$. While, the total explicit forcing $\mathbf{RE} = \mathbf{N}(\mathbf{\Psi}) + \tilde{\mathbf{R}}$ is calculated according to its definition using the updated solution, so $\mathbf{RE}_i^n = \mathbf{RE}_i(\mathbf{\Psi}^n)$. The total forcing $\mathbf{R} = \mathbf{RI} + \mathbf{RE}$ is then stored for the use in the subsequent time step in the auxiliary argument of MPDATA operator in Equation 3.35.

In the following, we briefly discuss the actual implementation of iterative formulation of Equation 3.35. The iterations progress stepwise such that the most current update of a dependent variable is used in the ongoing step, wherever possible. Each outer iteration has two distinct blocks. The first block involves the integration of the momentum transport equation where the magnetic field enters the Lorentz force and is taken as supplementary. Being at the half of a single outer iteration, it is denoted by the index $q-1/2$. This block ends with the final update of the velocity via the solution of the elliptic equation for ϕ. Hence, this block actually mirrors standard EULAG solution of hydrodynamic equations (Prusa et al., 2008), leading to the nomenclature "hydrodynamic block". The second block, referred as "magnetic block", uses the current updates of the velocities to integrate the induction equation. It ends with the final update of the magnetic field via the solution of the elliptic equation for $\phi^\star$ to clean the divergence of magnetic field. In the following we summarize sequence of steps fulfilled at each outer iteration for integrating the MHD equations Equation 3.25-Equation 3.28. For brevity, the superscripts n are dropped everywhere as by now there should be no ambiguity. Moreover, at $q = 1$ the initial guess for $\mathbf{v}$ and $\mathbf{B}$ is assumed as $\mathbf{v}^0 = 2\mathbf{v}^{n+1} - \mathbf{v}^n$ and $\mathbf{B}^0 = 2\mathbf{B}^{n+1} - \mathbf{B}^n$, respectively.

The first step of the hydrodynamic block starts with the estimation of the magnetic field $\mathbf{B}^{q-1/2}$ at time t^{n+1} by inverting the induction equation,

$$\mathbf{B}_i^{q-1/2} = \hat{\mathbf{B}}_i + 0.5\delta t\Big[\mathbf{B}^{q-1/2}\cdot\nabla\mathbf{v}^{q-1} - \mathbf{B}^{q-1/2}tr\{\nabla\mathbf{v}^{q-1}\}\Big]_i. \tag{3.39}$$

The subsequent step uses this latest magnetic field to obtain velocity following the standard EULAG procedure,

$$\mathbf{v}_i^q = \hat{\mathbf{v}}_i + \frac{0.5\delta t}{\rho_0\mu_0}(\nabla\cdot\mathbf{BB})_i^{q-1/2} - 0.5\delta t(\nabla\phi)_i^q. \tag{3.40}$$

Plugging this velocity in the discrete form of the Equation 3.27 produces the elliptic equation for the pressure ϕ, the solution of which provides the updated solenoidal velocity $\mathbf{v}$.

The first step of the magnetic block begins with estimation of magnetic field $\mathbf{B}^{q-1/4}$ at t^{n+1} using the update velocity, and the latest magnetic field is evaluated implicitly in analogy to Equation 3.39:

$$\mathbf{B}_i^{q-1/4} = \hat{\mathbf{B}}_i + 0.5\delta t\Big[\mathbf{B}^{q-1/4}\cdot\nabla\mathbf{v}^{q} - \mathbf{B}^{q-1/4}tr\{\nabla\mathbf{v}^{q}\}\Big]_i. \tag{3.41}$$

where the superscript $q-1/4$ symbolized as such for being a quarter of iteration away from the accomplishment. The subsequent step follows in the spirit of the momentum transport equation, using the conservative form of the forcing terms in the induction equation:

$$\mathbf{B}_i^q = \hat{\mathbf{B}}_i + 0.5\delta t(\nabla\cdot\mathbf{B}^{q-1/4}\mathbf{v}^q)_i - 0.5\delta t(\nabla\phi^\star)_i^q. \tag{3.42}$$

Implementing the magnetic field in the discrete form of the solenoidality condition Equation 3.28 produces the elliptic equation for auxiliary pressure term $\phi^\star$, the solution of which provides the updated solenoidal magnetic field $\mathbf{B}$.

Induction equation with the Hall term included, can be written in flux conservative form. To do so, let us start with the dimensionless generalized Ohm's law

$$\mathbf{E} + \mathbf{v}\times\mathbf{B} = \frac{\delta_i}{L}\mathbf{J}\times\mathbf{B}\ , \tag{3.43}$$

where $\mathbf{J} = \nabla\times\mathbf{B}$ is the dimensionless current density. The term $\mathbf{J}\times\mathbf{B} = (\nabla\times$

$\mathbf{B}) \times \mathbf{B} = -\mathbf{B} \times (\nabla \times \mathbf{B})$ can be simplified using the vector identity

$$-\mathbf{B} \times (\nabla \times \mathbf{A}) = \mathbf{A} \times (\nabla \times \mathbf{B}) - \nabla(\mathbf{A} \cdot \mathbf{B}) + (\mathbf{A} \cdot \nabla)\mathbf{B} + (\mathbf{B} \cdot \nabla)\mathbf{A} , \quad (3.44)$$
$$-\mathbf{B} \times (\nabla \times \mathbf{B}) = \mathbf{B} \times (\nabla \times \mathbf{B}) - \nabla(\mathbf{B} \cdot \mathbf{B}) + (\mathbf{B} \cdot \nabla)\mathbf{B} + (\mathbf{B} \cdot \nabla)\mathbf{B} , \quad (3.45)$$

using Equation 3.34, we get

$$-2\mathbf{B} \times (\nabla \times \mathbf{B}) = -\nabla(\mathbf{B} \cdot \mathbf{B}) + 2\nabla \cdot (\mathbf{BB}) , \quad (3.46)$$
$$-\mathbf{B} \times (\nabla \times \mathbf{B}) = -\nabla \left(\frac{B^2}{2} \right) + \nabla \cdot (\mathbf{BB}) . \quad (3.47)$$

Substituting Equation 3.47 in Equation 3.43 and taking curl leads to the induction equation of following form

$$\frac{\partial \mathbf{B}}{\partial t} = \nabla \times (\mathbf{v} \times \mathbf{B}) - \frac{\delta_i}{L} \nabla \times \nabla \cdot \mathbf{BB} . \quad (3.48)$$

In EULAG template or flux conservating form, the above equation for an incompressible flow can be written as

$$\frac{\partial \mathbf{B}}{\partial t} + \nabla \cdot \mathbf{vB} = \nabla \cdot \mathbf{Bv} - \frac{\delta_i}{L} \nabla \times \nabla \cdot \mathbf{BB} . \quad (3.49)$$

Incorporating the Hall forcing into the EULAG-MHD model follows the principles of the outlined standard MHD integrator above. Because the Hall term enters in induction equation as the curl of the Lorentz force, it can be judiciously updated and combined with the standard induction forcing, whenever the Lorentz force and/or the magnetic field are updated. In the current implementation it enters the explicit (lagged) counterpart of the induction force, and is updated after the inversion of the implicit evolutionary form of the induction equation in the "magnetic" block.

3.4 Implicit Large Eddy Simulation (ILES)

As discussed above, EULAG-MHD is based on MPDATA advection scheme. Notably, the higher-order truncation terms of MPDATA provide an implicit turbulence model (Domaradzki et al., 2003; Margolin et al., 2006) and hence, allow to conduct large eddy simulations (LESs) without using an explicit subgrid model (Smolarkiewicz & Prusa, 2002; Domaradzki et al., 2003; Domaradzki & Radhakrishnan, 2005; Rider, 2006; Prusa et al., 2008). In contrast to the standard LESs which filter out the under-resolved scales by applying explicit subgrid-scale models, MPDATA filter-outs the under-resolved scales by utilizing the residual dissipation—intermittent and adaptive to generation of under-resolved scales—produced via numerics which mimics the action of explicit subgrid scale turbulence models. In literature, such calculations relying on the properties of nonoscillatory numerics are referred as implicit large eddy simulations (ILESs). A comprehensive review of ILES with numerous examples are provided in the volume edited by Grinstein et al. (2007), including applications to local and global solar/stellar convection. In a simulation having fixed grid resolution, under-resolved scales appear at the reconnection regions. MPDATA then removes these under-resolved scales by producing locally effective residual dissipation, sufficient to sustain monotonic nature of the solution. Being intermittent and adaptive, the residual dissipation, as mentioned above, facilitate the model to perform ILESs. Such ILESs performed with the model have already been successfully utilized to simulate regu- lar solar cycles (Ghizaru et al., 2010), with the rotational torsional oscillations subsequently characterized and analyzed in (Beaudoin et al., 2013). The simulations conducted with EULAG-MHD continue relying on the effectiveness of ILES in regularizing the onset of magnetic reconnections, concurrent and collocated with the reconnection sites (Kumar et al., 2013, 2015a; Kumar & Bhattacharyya, 2016).

3.5 Summary

To summarize, in this Chapter, the important features of EULAG-MHD model such as MPDATA advection scheme and its dissipative property (ILES nature) have been discussed in detail. EULAG-MHD is based on (at least) second-order accurate (both in space and time) non-oscillatory forward in-time advection scheme MPDATA. MPDATA basically utilizes the donor-cell scheme in iterative manner to improve the accuracy of the solution while preserving the properties of the donor cell scheme. The derivation of MPDATA along with its important aspects relevant to our calculations has been discussed in detail. Then, the numerics of the numerical model EULAG-MHD are discussed. The model employs the established framework of EULAG with an additional magnetic block to solve the induction equation. Notably, the proven property of MPDATA to produce locally adaptive residual dissipations in response to generation of under-resolved scales, facilitates the numerical model to carry out computations in the spirit of implicit large eddy simulations. Our development of a 3D HMHD solver by incorporating the Hall forcing term in the numerical model EULAG-MHD, merits from the aforementioned property of the model.

The choice of the EULAG-MHD owes to its successful use in the simulation of solar coronal transients *viz.* flares and jets whereby the physical reconnections are mimicked using the residual dissipation of under-resolved scales at the locations of steep gradients. Away from steep-gradients, the flux-freezing is satisfied to the high fidelity. Since the Hall effect play a key role only at the locations where the gradients in magnetic field are strong, therefore the Hall term is incorporated in the model such that it is tied with the dissipation scale (of the order of spatial stepsize in the model). Thus, the Hall term is incorporated in the induction equation as an explicit forcing term which is solved using the standard MHD integrator discussed in this Chapter. This 3D HMHD solver is benchmarked in the Chapter 4 and further used to numerically simulate Hall effect on the evolution of magnetic flux ropes in Chapter 5 and an actual flaring active region in Chapter 6.

Chapter 4

Benchmarking the 3D HMHD solver

4.1 Introduction

With the EULAG MHD being extended to include Hall effect in the previous Chapter, the aim of this Chapter is to benchmark the developed 3D HMHD solver toward the known properties of Hall-assisted reconnection including the following:

- out-of-reconnection plane magnetic field component generation,
- in-plane current generation,
- sharp changes in the current density rate,
- magnetic energy dissipation unaffected by Hall forcing.

For the purpose, we select the initially unidirectional sinusoidal magnetic field with the non-zero initial Lorentz force. This initial condition differs from the traditional initial condition involving the Harris current-sheet or the GEM challenge (Birn et al., 2001). The developed 3D EULAG HMHD numerical model has been employed to simulate the evolution of magnetic field lines in the presence and absence of Hall forcing term (i.e., Hall MHD and MHD, respectively). It solves the dimensional set of Hall MHD and MHD equations in cgs units, invoked in Section 4.2. The magnetic reconnections in both the simulations are compared to investigate the Hall effect. Linear analysis of the Hall MHD equations leads to the two type of waves namely whistler and Hall drift waves (Huba, 2003). In this Chapter, we present the whistler wave modes analysis and compare the analytical frequency to numerical frequency.

4.2 Numerical Model

The two sets of numerical experiments presented in this Chapter use dimensional and dimensionless set of equations which we describe in this section. The numerical experiment to benchmark the 3D EULAG HMHD solver solves the dimensional equations while the wave exploration experiment utilizes the dimensionless equations. Using a conservative flux-form and dyadic notation, the dimensional Hall MHD equations are compactly written (in cgs units) as

$$\frac{\partial \mathbf{v}}{\partial t} + \nabla \cdot \mathbf{v}\mathbf{v} = -\nabla\phi + \frac{1}{4\pi\rho_0}\nabla \cdot \mathbf{B}\mathbf{B} + \mu_0 \nabla^2 \mathbf{v} \ , \tag{4.1}$$

$$\frac{\partial \mathbf{B}}{\partial t} + \nabla \cdot \mathbf{v}\mathbf{B} = \nabla \cdot \mathbf{B}\mathbf{v} - \frac{d_0}{4\pi}\left(\nabla \times \nabla \cdot \mathbf{B}\mathbf{B}\right) - \nabla\phi^* \ , \tag{4.2}$$

$$\nabla \cdot \mathbf{v} = 0 \ , \tag{4.3}$$

$$\nabla \cdot \mathbf{B} = 0 \ , \tag{4.4}$$

where ρ_0 and μ_0 denote constant density and kinematic viscosity respectively, $\phi = \left(p + \mathbf{B}^2/8\pi\right)/\rho_0$ is the density normalized total pressure, and $d_0 = \sqrt{4\pi}\delta_i/\sqrt{\rho_0}$; the $-\nabla\phi^*$ term on the right-hand-side (rhs) is already explained in Section 3.3.2. The dimensionless equations

$$\frac{\partial \mathbf{v}}{\partial t} + \nabla \cdot \mathbf{v}\mathbf{v} = -\nabla\phi + \nabla \cdot \mathbf{B}\mathbf{B} + \frac{\tau_A}{\tau_\nu}\nabla^2 \mathbf{v} \ , \tag{4.5}$$

$$\frac{\partial \mathbf{B}}{\partial t} + \nabla \cdot \mathbf{v}\mathbf{B} = \nabla \cdot \mathbf{B}\mathbf{v} - \frac{\delta_i}{L_0}\left(\nabla \times \nabla \cdot \mathbf{B}\mathbf{B}\right) - \nabla\phi^* \ , \tag{4.6}$$

$$\nabla \cdot \mathbf{v} = 0 \ , \tag{4.7}$$

$$\nabla \cdot \mathbf{B} = 0 \ , \tag{4.8}$$

are achieved using the following normalizations used in Equation 4.1 - Equation 4.4

$$\mathbf{B} \longrightarrow \frac{\mathbf{B}}{B_0}, \quad \mathbf{v} \longrightarrow \frac{\mathbf{v}}{v_A}, \quad L \longrightarrow \frac{L}{L_0}, \quad t \longrightarrow \frac{t}{\tau_A}, \quad p \longrightarrow \frac{p}{\rho {v_A}^2} \ , \tag{4.9}$$

The ratio τ_A/τ_ν is an effective viscosity of the system which, along with the other forces, influences the magnetofluid evolution. The constant B_0 is kept arbitrary, whereas L_0 is fixed to the system size. Further, $v_A \equiv B_0/\sqrt{4\pi\rho_0}$ is the Alfvén speed, where ρ_0 is a constant mass density. The τ_A and τ_ν are respectively the Alfvén transit time ($\tau_A = L_0/v_A$) and viscous diffusion time scale ($\tau_\nu = L_0^2/\nu$). The kinematic viscosity is denoted by ν. The equations are numerically integrated using the 3D HMHD solver and the model assumes the magnetofluid to be thermodynamically inactive and incompressible, having zero physical resistivity.

4.3 Results

4.3.1 Benchmarking the 3D HMHD solver

To benchmark the HMHD solver, the initial field is selected as

$$B_x = 0 \ , \tag{4.10}$$

$$B_y = 0 \ , \tag{4.11}$$

$$B_z = 2.5\sin(x) \ , \tag{4.12}$$

with $x, y, z \in [-2\pi, 2\pi]$, respectively, in each direction of a 3D Cartesian domain. This selection has two merits: first, the magnetic field reverses at x=0; and second, the Lorentz force

$$(\mathbf{J} \times \mathbf{B})_x = -6.25\cos(x)\sin(x) \ , \tag{4.13}$$

$$(\mathbf{J} \times \mathbf{B})_y = 0 \ , \tag{4.14}$$

$$(\mathbf{J} \times \mathbf{B})_z = 0 \ , \tag{4.15}$$

generates a converging flow that onsets magnetic reconnections.

Equation 4.1-Equation 4.4 are solved for $d_0 = 0, \ 2$. The latter selection of d_0 optimizes the computation time and a tractable development of magnetic structures for the employed spatio-temporal resolution. The corresponding $\delta_i = 0.56$ is slightly higher than the spatial stepsize $\delta\mathbf{x} \approx 0.40$ set for the simulation. Consequently, the Hall forcing kicks in near the dissipation scale, thereby directly affecting the overall dynamics only in vicinities of the reconnection regions. With the large scale $L = 4\pi$ of the magnetic field variability, the resulting $\delta_i/L \approx 0.04$ is of the order of solar coronal value. The simulations are then expected to capture dynamics of the Hall MHD and the intermittently diffusive regions of corona-like plasmas, thus shedding light on the evolution of neighboring frozen-in magnetic field lines. Moreover, $1/S < \delta_i/L$ as discussed in Introduction. The physical domain is resolved with $32 \times 32 \times 32$ grid. A coarse resolution is selected for an earlier onset of magnetic reconnections and to expedite the overall evolution. The kinematic viscosity and mass density are set to $\nu = 0.005$ and $\rho_0 = 1$, respectively. All three boundaries are kept open. The initial magnetic field is given by the Equation 4.10-~~Equation~~ 4.12 and the fluid is evolved from an initially static state having pressure $p = 0$.

The overall evolution is depicted in different panels of Figure 4.1. The initial Lorentz force, given by Equation 4.13 - Equation 4.15, pushes segments of the fluid on either sides of the field reversal layers—toward each other. Consequently, magnetic energy gets converted into kinetic energy of the plasma flow: panels (a) and (b). Panels (c) and (d) show history of grid-averaged magnitude of the the out-of-plane (along y) and in-plane (xz plane) magnetic fields. Notably, for $d_0 = 0$ (MHD) the out-of-plane field is negligibly small compared to its value for $d_0 = 2$ (Hall MHD). Such generation of the out-of-plane magnetic field is inherent to Hall MHD and is in conformity with the result of another simulation (Ma & Bhattacharjee, 2001). The panels (e) and (f) illustrate the variation of the rate of change of out-of-plane current density and total volume current density. Importantly, in contrast to the $d_0 = 0$ curve, the rate of change of volume current density shows an early bump at (≈ 7.5 s) and a well defined peak ($t \approx 9.75$ s) for $d_0 = 2$. Such peaks in the current density are expected in the impulsive phase of solar flares, and they manifest magnetic reconnections in the presence of the Hall term (Bhattacharjee, 2004).

Figure 4.2 plots magnetic field lines tangential to pre-selected planes during different instances of the evolution for $d_0 = 0$. The panel (a) plots the initial magnetic field lines for referencing. The initial Lorentz force pushes anti-parallel magnetic field lines (depicted in the inset) toward each other. Subsequently, X-type neutral

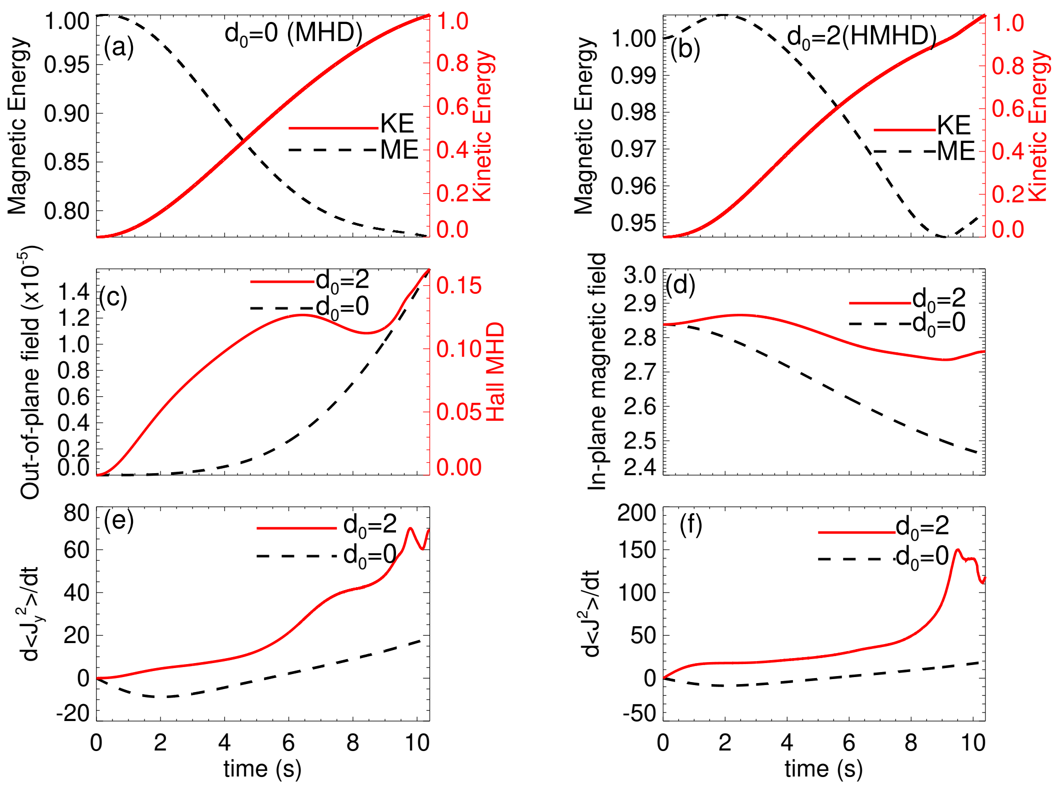

Figure 4.1: Panels (a) and (b) show the evolution of the magnetic energy (black dashed curve) and kinetic energy (red solid curve) for $d_0 = 0$ (MHD) and $d_0 = 2$ (Hall MHD) respectively. Panel (c) shows the evolution of out-of-plane magnetic field for $d_0 = 0$ (MHD) with black dashed curve and $d_0 = 2$ (Hall MHD) with red solid curve respectively. Also in panels (a) to (c), the scales for the solid and the dashed curves are spaced at right and left respectively. Panels (d) to (f) represent in-plane magnetic field, amplitudes of the rate of change of out-of-plane and total current densities for $d_0 = 0$ (black dashed curve) and $d_0 = 2$ (red solid curve) respectively. The variables in panels (a) and (b) are normalized with the initial total energies. All the variables are averaged over the computational domain. Important are the generation of the out-of-plane magnetic field along with sharp changes in time derivatives of the out-of-plane and total volume current densities in Hall MHD simulation.

points develop near $z = \pm 2\pi$. The consequent magnetic reconnections generate a complete magnetic island which maintains its identity for a long time. Such islands, stacked on each other along the y, generate an extended magnetic flux tube (MFT) at the center, which in its generality is a magnetic flux surface. Further evolution breaks the MFT such that the cross section of the broken tube yields two magnetic islands. The point of contact between the two tear-drop shaped magnetic field lines generates an X-type neutral point. Notably, within the computational time, no field is generated along the y direction and the corresponding symmetry is exactly preserved.

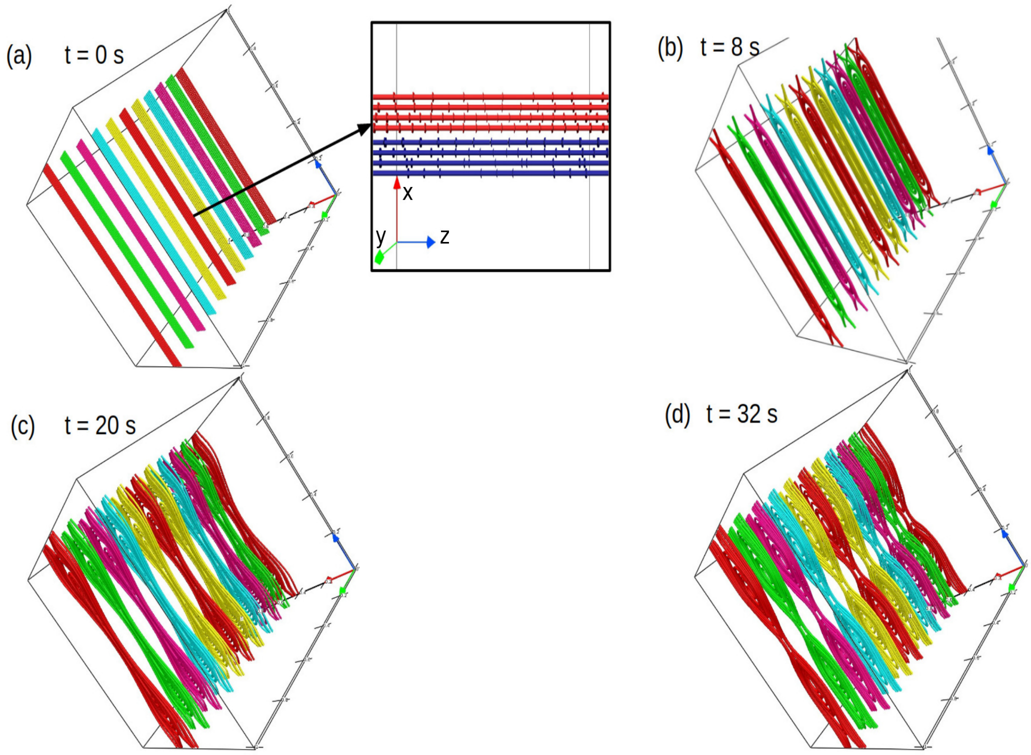

Figure 4.2: Snapshots of preselected magnetic field lines for the $d_0 = 0$ (MHD) simulation, plotted on equidistant y-constant planes. In all figures (this and hereafter), the red, green and blue arrows represent the x, y and z-axis respectively. The inset in panel (a) highlights the polarity reversal of the initial magnetic field lines. The plots illustrate the formation of a primary flux tube (panel (b)) made by stacking of the depicted magnetic field lines. Notably symmetry is preserved throughout evolution.

In Figure 4.3 we provide the 2D projection of the magnetic field lines on the $y = 0.5$ plane, for later comparison with similar projection for the $d_0 = 2$ case.

The panels (a) to (b) and (c) to (d) of Figure 4.4 show magnetic field lines evolution for $d_0 = 2$ from two different vantage points.

The field lines are plotted on different y constant planes centered at $x = 0.5$ and $x = 0.74435$. The planes are not connected by any field lines at $t = 0$. Importantly out-of-plane magnetic field is generated with time in both sets of field lines (at $x = 0.5$ and $x = 0.74435$), which connects two adjacent planes (cf. panel (b) of Figure 4.2 and Figure 4.4 and breaks the y symmetry that was preserved in the $d_0 = 0$ case — asymmetry in reconnection planes. Consequently the evolved $\mathbf{B}$ is three-dimensional. Also, the out-of-plane component (B_y) has a quadrupole structure, shown in Figure 4.5, which is in congruence with observations and models (Mozer et al., 2002).

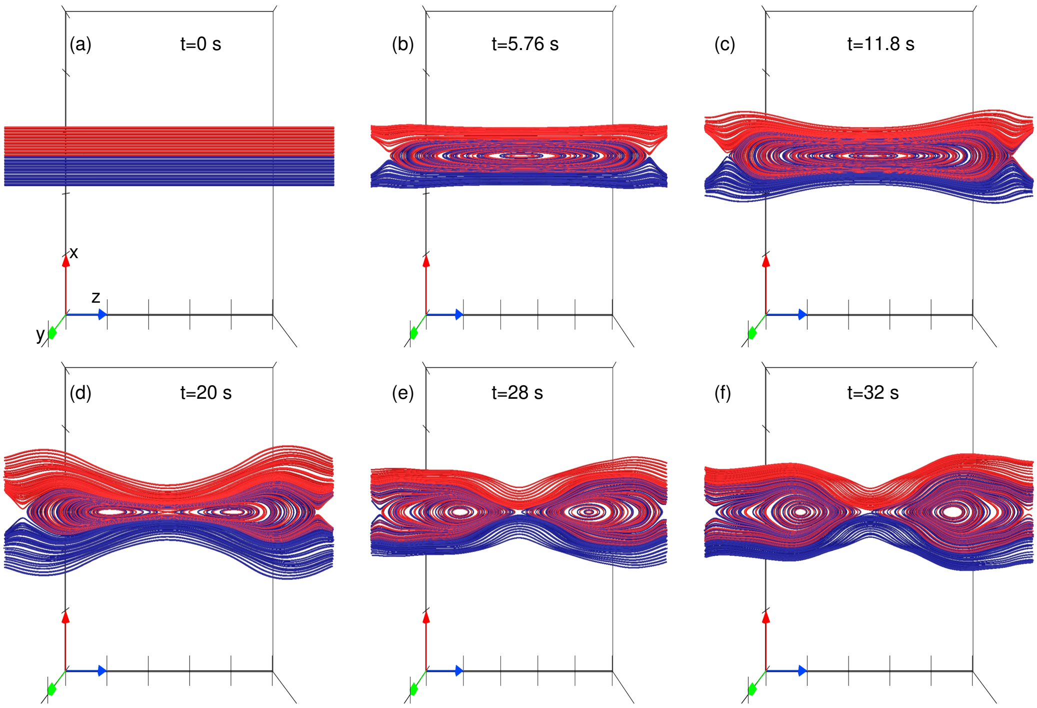

Figure 4.3: Projection of magnetic field lines depicted in Figure 4.2 on a y constant plane during their evolution. Notable is the formation of a primary magnetic island having a single O-type neutral point. Subsequently, the primary island breaks into two secondary islands which are separated by an X type neutral point.

For better clarity the magnetic field lines evolution is further detailed in Figure 4.6 and Figure 4.7. In Figure 4.6 important is the development of two MFTs constituted by disjointly stacked magnetic islands. The islands are undulated and appear much earlier compared to the $d_0 = 0$ case, indicating the faster reconnection. Notable is also the creation of flux ropes where a single helical field line makes a large number of turns as the out-of-plane field B_y develops (Figure 4.7). In principle, the magnetic field line may ergodically span the MFS, if the "safety factor" $q = rB_y/\mathcal{L}B_T$ is not a rational number (Freidberg, 1982); here r and $\mathcal{L}$ are the radius and length of the rope, respectively, and $B_T = \sqrt{B_x^2 + B_y^2}$. Further evolution breaks the flux rope into secondary ropes by internal magnetic reconnections—i.e., reconnections between magnetic field lines constituting the rope—shown in panels (a) to (d) of Figure 4.7, where two oppositely directed sections of the given magnetic field lines reconnect (location marked by arrows in the Figure 4.7). Since most of the contemporary Hall simulations are in 2D, in Figure 4.8 we plot the projection of field lines depicted in Figure 4.4 on $y = 0.5$ plane. The corresponding evolution is visibly similar to the generation of secondary islands (Shi et al., 2019),

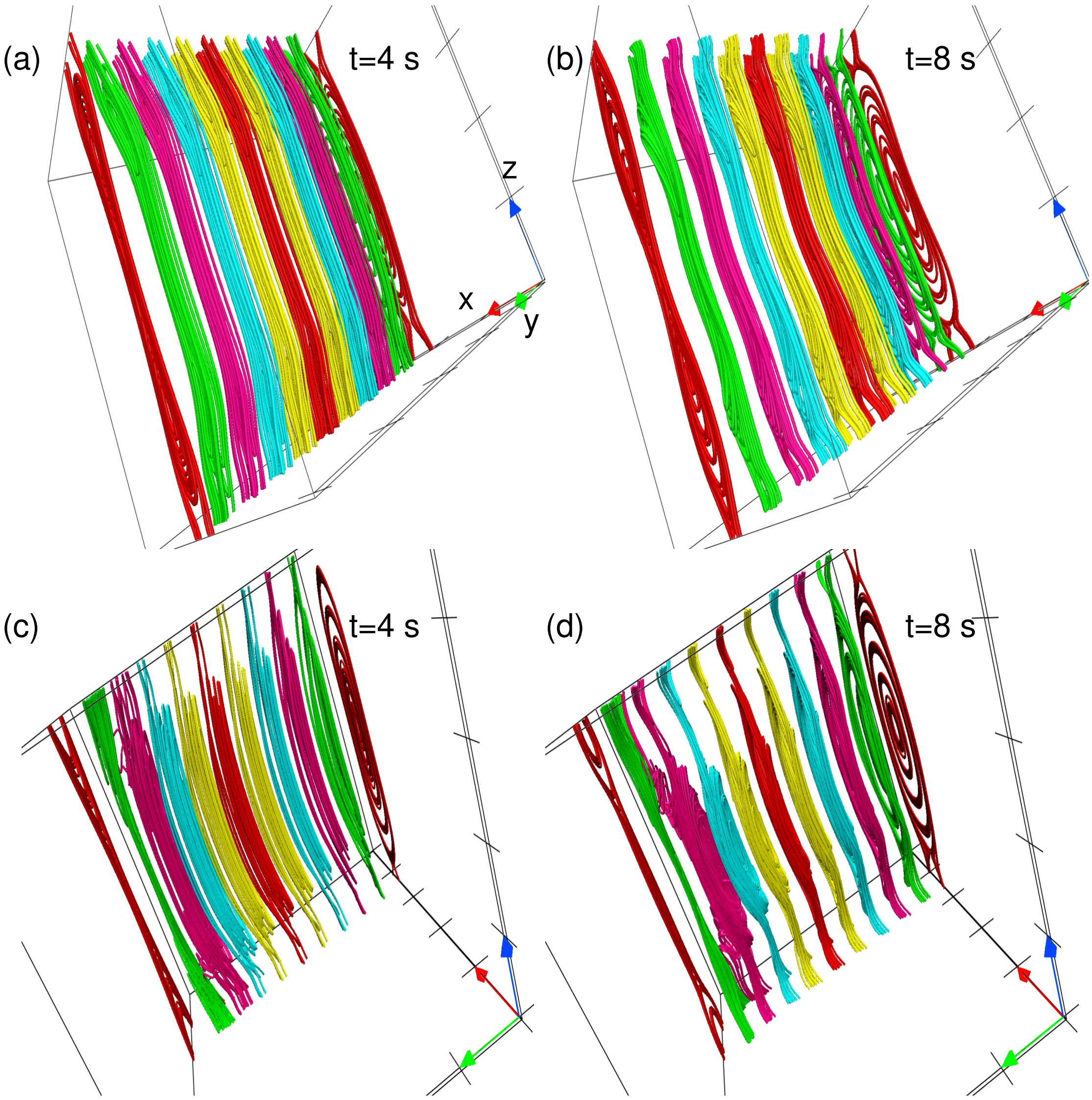

Figure 4.4: Magnetic field lines evolution for $d_0 = 2$ (Hall MHD) case, from two vantage points. The field lines are plotted on planes centered at $x = 0.5$ and $x = 0.74435$ and equidistant along y. Important is the symmetry breaking, cf. field lines at $y = -2\pi$ and $y = 2\pi$ of the panel (b) and (d). The out-of-plane magnetic field is generated throughout the domain.

and their later coalescence as envisioned by Shibata & Tanuma (2001).

4.3.2 Investigation of the whistler wave modes using the 3D HMHD solver

To complete the benchmarking, we repeat the numerical experiment described in Huba (2003), where wave propagation in the presence of the Hall forcing is explored. Notably, the EULAG-MHD being incompressible and plasma being homogeneous, we only concentrate on the whistler wave modes.

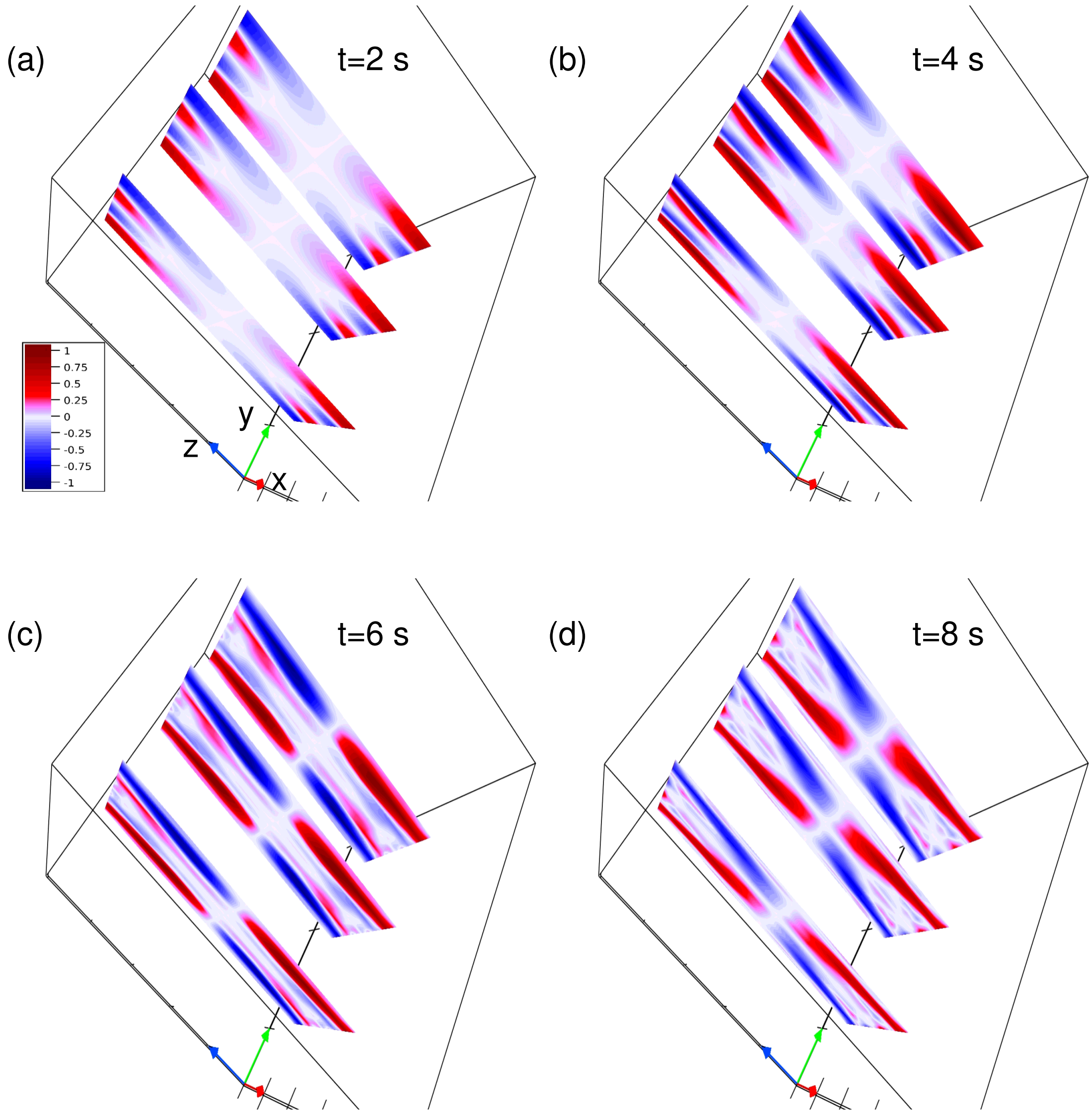

Figure 4.5: Contour plots of $B_y(x,z)$ (out-of-plane component) on y-constant planes for $d_0 = 2$ (Hall MHD), with time. The plots confirm the quadrupolar nature of the out-of-plane component of the magnetic field.

Let us consider the induction equation in it's dimensionless form

$$\frac{\partial \mathbf{B}}{\partial t} = -\frac{\delta_i}{L_0}\nabla \times (\mathbf{J} \times \mathbf{B}) \ ,$$

which can also be written as

$$\frac{\partial \mathbf{B}}{\partial t} = -\frac{\delta_i}{L_0}\nabla \times ((\nabla \times \mathbf{B}) \times \mathbf{B}) \ , \tag{4.16}$$

Now assuming that the time independent ambient magnetic field is in the z

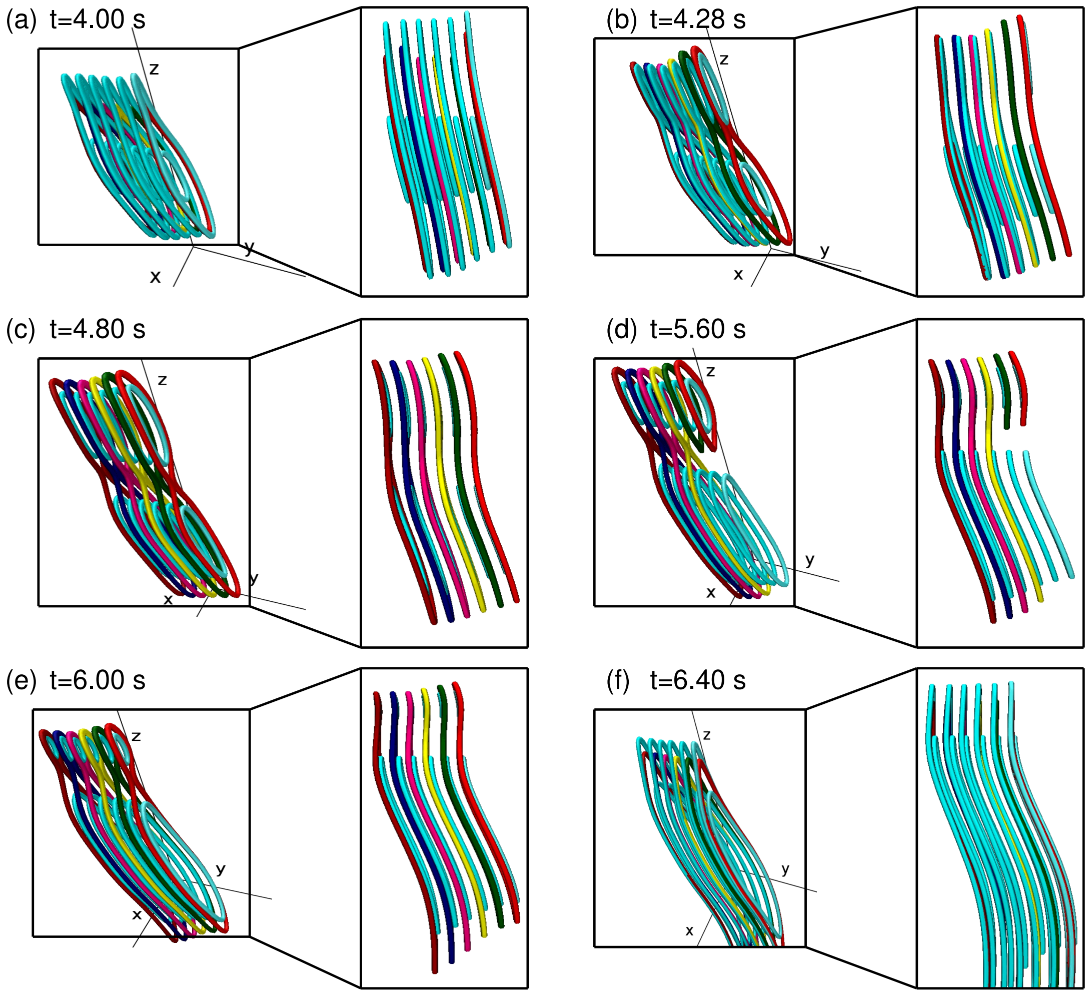

Figure 4.6: Panels (a) to (f) show the magnetic field lines evolution for $d_0 = 2$ (Hall MHD) case, from two different angles to highlight the generation of two MFTs constituted by disjoint field lines. The islands look like "figure 8" structure; Panels (b) to (d). The side view of the field lines are shown in the insets, highlighting their undulated geometry. The three black lines in the background represent the three axes.

direction and the perturbations are along x and y directions, we have

$$\mathbf{B} = \delta\boldsymbol{\mathcal{B}} + \boldsymbol{\mathcal{B}_z}$$

where $\delta\boldsymbol{\mathcal{B}} = \delta B_x\hat{\boldsymbol{i}} + \delta B_y\hat{\boldsymbol{j}}$ and $\boldsymbol{\mathcal{B}_z} = B_0\hat{\boldsymbol{k}}$.

and a first order linear analysis yields

$$\frac{\partial(\delta\boldsymbol{\mathcal{B}})}{\partial t} = -\frac{\delta_i}{L_0}\nabla\times[(\nabla\times\delta\boldsymbol{\mathcal{B}})\times\boldsymbol{\mathcal{B}_z}] \ , \tag{4.17}$$

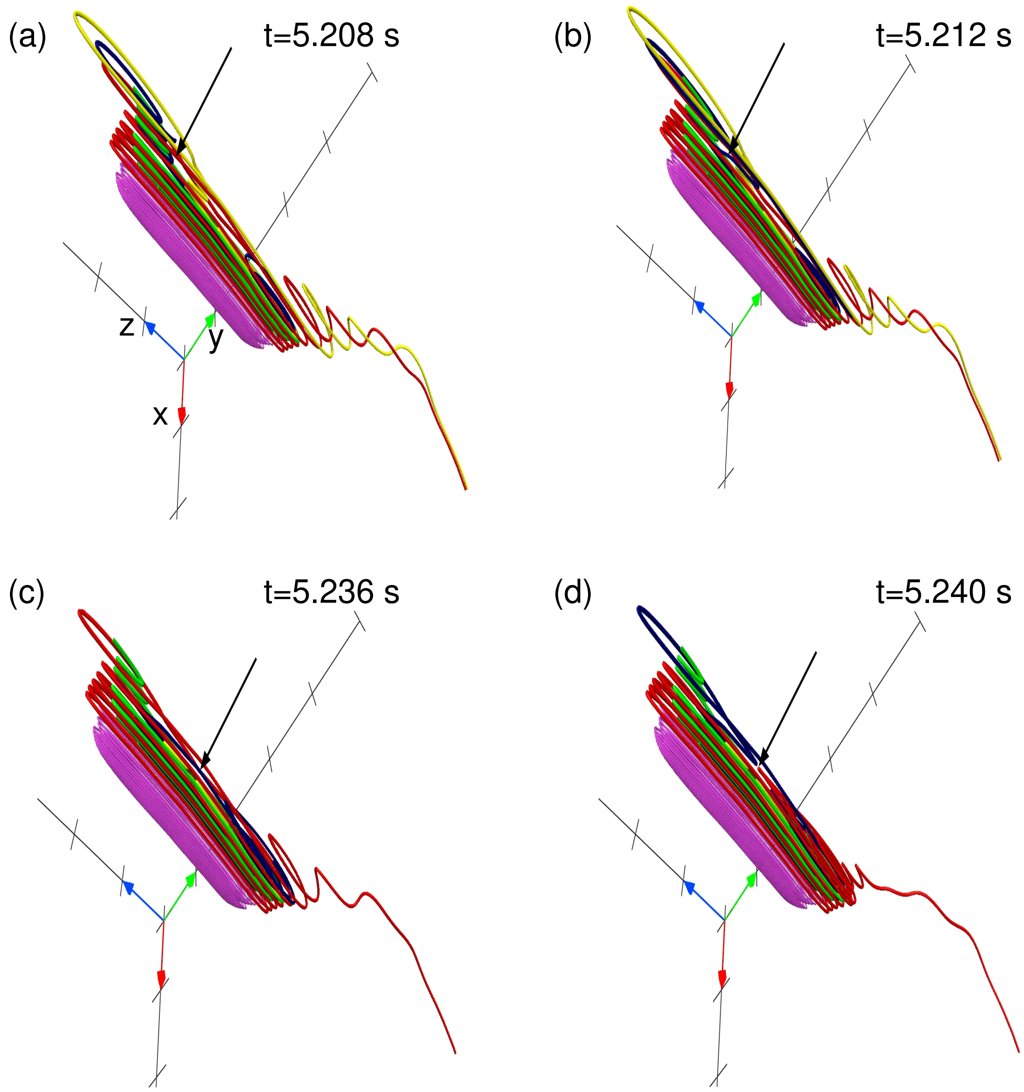

Figure 4.7: Panels (a) and (b) show the topology of the magnetic field lines for the $d_0 = 2$ (Hall MHD) evolution, prior and after the internal reconnection of the dark blue colored field line (marked by the arrow). Panels (c) and (d) depict the topology of field lines prior and after the internal reconnection of blue and red color field lines within rope, marked by arrow.

since

$$\nabla \times \delta\boldsymbol{\mathcal{B}} = -\hat{\boldsymbol{i}}\frac{\partial \delta B_y}{\partial z} + \hat{\boldsymbol{j}}\frac{\partial \delta B_x}{\partial z}$$

,

and

$$(\nabla \times \delta\boldsymbol{\mathcal{B}}) \times \boldsymbol{\mathcal{B}_z} = \hat{\boldsymbol{j}}B_0\frac{\partial \delta B_y}{\partial z} + \hat{\boldsymbol{i}}B_0\frac{\partial \delta B_x}{\partial z}$$

,

The right hand side of Equation 4.17 can be expressed by taking the curl of above equation

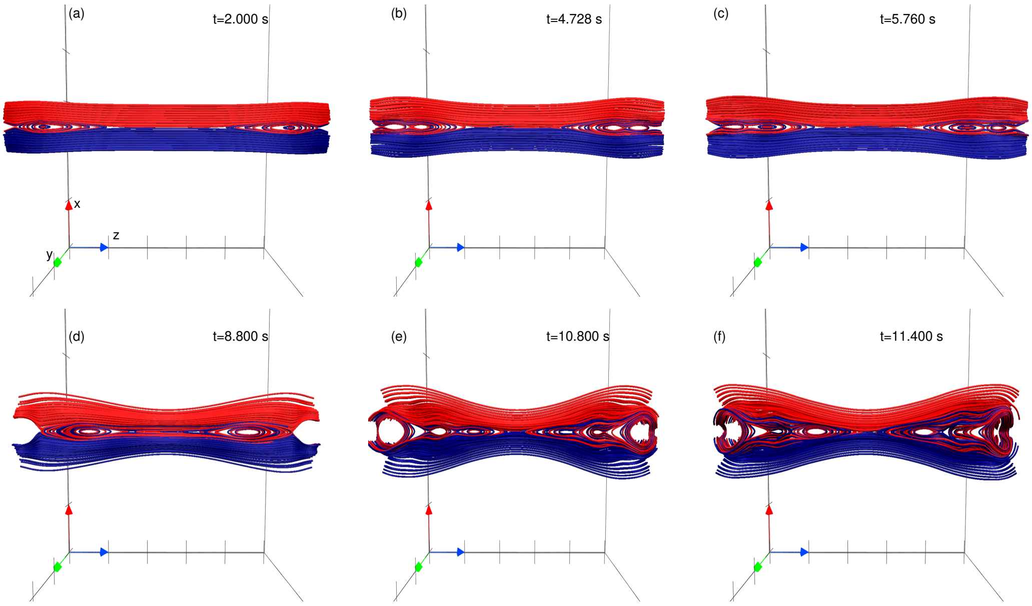

Figure 4.8: Magnetic field lines evolution for $d_0 = 2$ (Hall MHD), projected on y constant plane. Panel (a) depicts development of two primary magnetic islands. Panels (b) and (c) show their further breakage into secondary islands. Panels (d) to (f) show generation of an X type neutral point by subsequent merging of the two islands.

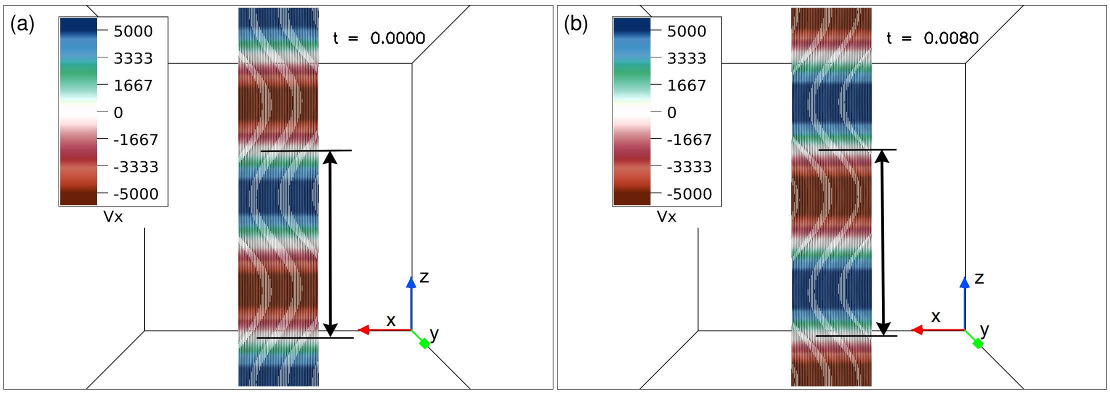

Figure 4.9: Whistler wave amplitude variation from t=0 (panel (a)) to t=0.0080 (panel (b)) for mode number m=2. The color bar on the left hand side depicts x component of velocity between -5000 to 5000. Length of the region between black arrows (in panel (a) and (b)), i.e., twice the distance between two consecutive nodes (white regions marked by horizontal black lines) is the wavelength λ_N. Notable is the amplitude variation from successive negative-positive (at t=0) to positive-negative (at t=0.0080) respectively. The red, green, and blue arrows on the bottom right of computational domain represent the x, y, and z axes of Cartesian coordinate system respectively in this figure and Figure 4.10 and Figure 4.11

$$\nabla \times [(\nabla \times \delta \boldsymbol{\mathcal{B}}) \times \boldsymbol{\mathcal{B}_z}] = -\hat{\boldsymbol{i}} B_0 \frac{\partial^2 \delta B_y}{\partial z^2} + \hat{\boldsymbol{j}} B_0 \frac{\partial^2 \delta B_x}{\partial z^2}$$

Now the Equation 4.17 can be written as

$$\frac{\partial(\delta\boldsymbol{\mathcal{B}})}{\partial t} = -\frac{\delta_i}{L_0}\left(-\hat{\boldsymbol{i}}B_0\frac{\partial^2\delta B_y}{\partial z^2} + \hat{\boldsymbol{j}}B_0\frac{\partial^2\delta B_x}{\partial z^2}\right)$$

The magnetic field perturbation is assumed to be a plane wave, with δB_x and $\delta B_y \propto \exp(ik_z z - i\omega t)$, then $\frac{\partial}{\partial t} \to i\omega$, $\nabla_z \to (-ik_z)$ and ${\nabla_z}^2 \to -{k_z}^2$.

$$i\omega\left(\delta B_x\hat{\boldsymbol{i}} + \delta B_y\hat{\boldsymbol{j}}\right) = -\frac{\delta_i}{L_0}\left(\hat{\boldsymbol{i}}B_0{k_z}^2\delta B_y - \hat{\boldsymbol{j}}B_0{k_z}^2\delta B_x\right) \ , \tag{4.18}$$

$$\omega\delta B_x = i\frac{\delta_i}{L_0}B_0{k_z}^2\delta B_y \ , \tag{4.19}$$

$$\omega\delta B_y = -i\frac{\delta_i}{L_0}B_0{k_z}^2\delta B_x \ , \tag{4.20}$$

$$\omega^2 = -i^2\left(\frac{\delta_i}{L_0}\right)^2{B_0}^2{k_z}^4 \ , \tag{4.21}$$

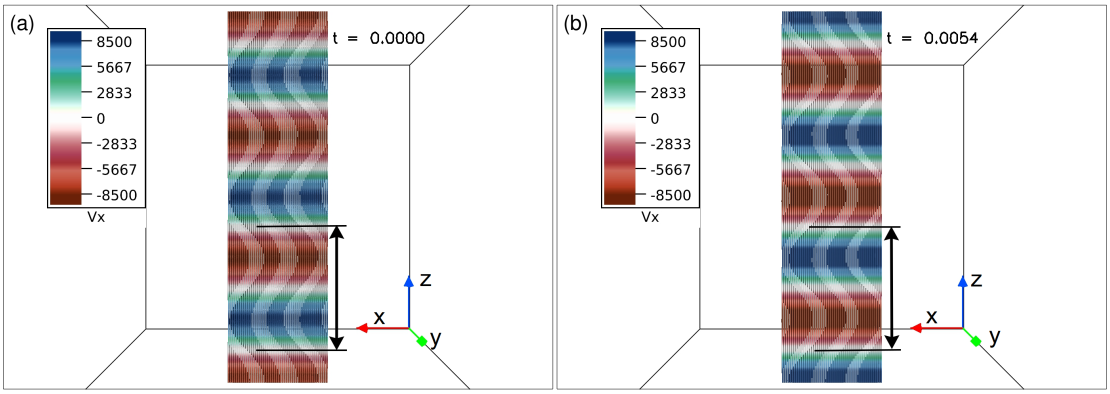

Figure 4.10: Whistler wave amplitude variation from t=0 (panel (a)) to t=0.0054 (panel (b)) for mode number m=3. The color bar on the left hand side depicts x component of velocity between -8500 to 8500. Length of the region between black arrows (in panel (a) and (b)), i.e., twice the distance between two consecutive nodes (white regions marked by horizontal black lines) is the wavelength λ_N. Notable is the amplitude variation from successive positive-negative (at t=0) to negative-positive (at t=0.0054) respectively.

Finally, the dimensionless dispersion relation of whistler wave is obtained as

$$\boxed{\omega = \left(\frac{\delta_i}{L_0}\right)B_0{k_z}^2}$$

Following Huba (2003), the ambient field is set up as

$$B_z = B_0 \ , \tag{4.22}$$

whereas the perturbations are

$$\delta B_x = \delta B_0 \sin\left(\frac{2\pi m z}{L_0}\right) \ , \tag{4.23}$$

$$\delta B_y = \delta B_0 \cos\left(\frac{2\pi m z}{L_0}\right) \ , \tag{4.24}$$

where L_0 is the size of system which is set equal in all three directions x, y, and z of a Cartesian coordinate system and m is the wave mode number. According to the perturbation expressions Equation 4.24, the total length (L_z) on each plane in computational domain will satisfy $L_z = m\lambda$. The parameters set for simulation are $B_0 = 1000$, $\delta B_0 = 10$ and $L_0 = 7\pi$. The simulations are carried out on a computational domain of size $128 \times 128 \times 128$ and the dimensionless Hall MHD equations are employed. The analytical wave propagation number is given by $k_z^A = \frac{2\pi m}{L_0}$ and the numerical wave propagation number is given by $k_z^N = \frac{2\pi}{\lambda_N}$. λ_N is the wavelength—twice the distance between two consecutive nodes—calculated from the simulation outcomes and shown in the Figure 4.9, Figure 4.10, and Figure 4.11.

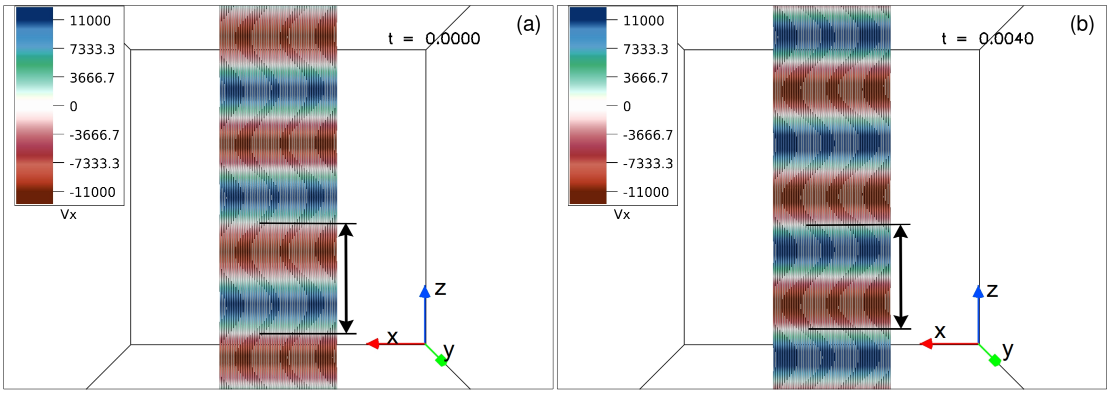

Figure 4.11: Whistler wave amplitude variation from t=0 (panel (a)) to t=0.0040 (panel (b)) for mode number m=4. The color bar on the left hand side depicts x component of velocity between -11000 to 11000. Length of the region between black arrows (in panel (a) and (b)), i.e., twice the distance between two consecutive nodes (white regions marked by horizontal black lines) is the wavelength λ_N. Notable is the amplitude variation from successive positive-negative (at t=0) to negative-positive (at t=0.0040) respectively.

The ratio of analytical to numerical frequencies obtained for few modes are listed in the Table 4.1, confirming the simulations to replicate the analytical calculations fairly well.

m	Analytical frequency (ω_A)	Numerical frequency (ω_N)
2	26.12	27.50
3	132.237	141.88
4	417.92	430.04

Table 4.1: List of parameters for the wave simulation.

4.4 Summary and Conclusion

In this Chapter, the developed 3D HMHD solver has been benchmarked with an initially sinusoidal magnetic field, symmetric in the y direction of the employed Cartesian coordinate system. The choice of the field is based on its simplicity and non-force-free property to exert Lorentz force on the magnetofluid at $t = 0$. Moreover, the selected field provides an opportunity to independently verify the physics of Hall MHD without repeating the more traditional computations related to the Harris equilibrium or the GEM challenge. Simulations are carried out in the absence and presence of the Hall term. In the absence of the Hall term the magnetic field maintains its symmetry as magnetic reconnections generate magnetic flux tubes made by disjoint magnetic field lines. With the Hall term, the evolution becomes asymmetric and 3D due to the development of magnetic field which is directed out of the reconnection plane. This is in concurrence with earlier simulations. Along with the flux tube, magnetic reconnections also generate magnetic flux rope in the Hall MHD. When viewed along the negative y direction, the rope and the tube appear as magnetic islands. Further evolution, leads to breakage of the primary islands into secondary islands and later, their coalescence. The results, overall, agree with the existing scenarios of Hall-reconnection based on physical arguments and other recent simulations including those on the GEM challenge. An important finding is the formation of complex 3D magnetic structures which can not be apprehended from 2D models or calculations although their projections agree with the latter. Alongside, we have numerically explored the Whistler mode propagation vis-a-vis its analytical model and found the two to be matching reasonably well.

The overall simulation results with the 3D HMHD solver give us the confidence to use it to model naturally observed magnetic structures further.

Chapter 5

Investigations of the Hall effect on magnetic reconnection during the evolution of a magnetic flux rope

5.1 Introduction

The results presented in Section 4.3.1 depict the magnetic flux rope (MFR) formation owing to the generation of an out-of-plane (reconnection plane) magnetic field component—one of the well known feature of the Hall-assisted magnetic reconnection. MFR is defined as a bundle of helically twisted magnetic field lines wrapped along a common axis (Zhong et al., 2021). MFR is often regarded the fundamental structure associated CMEs on the Sun. There are two concepts of MFR eruption associated to CMEs; one considers the pre-existing MFR in the solar atmosphere confining the plasma material and the another assumes MFR formation in consequence of magnetic reconnection from initially highly sheared magnetic arcades. Models based on observations, such as CSHKP **cite**, tether cutting **cite**, and breakout— irrespective of their applicability to explain successful CME—suggest that magnetic reconnections beneath the MFR essentially shape the on-the-fly MFR. In brief, the CME models require MFRs to confine plasma. Destabilized from its equilibrium, as the MFR ascends with height—it stretches the overlaying magnetic field lines. The ascend of the rope decreases the magnetic pressure below it which, in turn sucks in more field lines below the rope. These non-parallel field lines reconnect and the generated outflow further pushes the MFR up. It is then imperative to study the effects of Hall forcing on such magnetic reconnections during evolution of an MFR. For the purpose, in this Chapter, the developed 3D EULAG solver is employed to simulate the evolution of MFRs in the presence and absence of the Hall forcing. The aim of this work is to explore the topological changes owing to Hall effect on magnetic reconnections by investigating simulated magnetic field lines dynamics and their comparison in the Hall MHD and MHD. To ascertain the MFR generation, the simulations are initiated with the initial conditions of Kumar et al. (2016). The work presented in this Chapter is mainly divided in two case studies where the first one uses an axisymmetric (2.5D) and the second one uses fully 3D initial bipolar sheared magnetic field configurations. In this Chapter, the efficient and faster reconnections along with the magnetic topological changes during the Hall MHD simulations are reported. A comprehensive analysis of reconnection-assisted MFR evolution for the two cases is presented below.

5.2 Case-I: MFR generated from a 2.5D initial analytical magnetic field

The simulations are initiated with an axisymmetric (2.5D) magnetic field given in Kumar et al. (2016)

$$B_x = k_z \sin(k_x x) \exp\left(\frac{-k_z z}{s_0}\right) , \tag{5.1}$$

$$B_y = \sqrt{k_x^2 - k_z^2} \sin(k_x x) \exp\left(\frac{-k_z z}{s_0}\right) , \tag{5.2}$$

$$B_z = s_0 k_x \cos(k_x x) \exp\left(\frac{-k_z z}{s_0}\right) , \tag{5.3}$$

with $k_x = 1.0$, $k_z = 0.9$ and $s_0 = 6$.

Dynamical evolution of the above initial field is governed by the Equation 4.1 - Equation 4.4 given in the Section 4.2 of previous Chapter. The effective viscosity and mass density are set to $\tau_A/\tau_\nu = 2\times10^{-5}$ and $\rho_0 = 1$, respectively. Equation 4.1 - Equation 4.4 are numerically integrated using the 3D HMHD solver described in

Chapter 3.

The magnetic field lines are depicted in panel (a) of Figure 5.1 which are sheared bipolar loops having a straight Polarity Inversion Line (PIL) and no field-line twist. For simulations, a physical domain of the extent $[\{0, 2\pi\}, \{0, 2\pi\}, \{0, 8\pi\}]$ is resolved on the computational domain of size $64 \times 64 \times 128$, making the spatial step sizes $\delta x = \delta y = 0.0997$, $\delta z = 0.1979$. The temporal step size is $\delta t = 16 \times 10^{-4}$. The initial state is assumed to be motionless and open boundary conditions are employed. The simulations are carried out for $\delta_i/L_0 = 0$ and $\delta_i/L_0 = 0.04$, having a simulated physical time of $7000\tau_A\delta t$. The arbitrary B_0 can be selected such that the Alfvén transit time, $\tau_A \in \{1, 10\}$ s makes the simulated time, 11.2 s to 112 s consistent with the beginning of the impulsive phase of a flare 100 s to 1000 s.

The evolution onsets as the Lorentz force

$$(\mathbf{J} \times \mathbf{B})_x = \left[-k_x(k_x^2 - k_z^2) + k_x s_0 \left(s_0 k_x^2 - \frac{k_z^2}{s_0}\right)\right] \times \sin^2(k_x x) \exp\left(-\frac{2k_z z}{s_0}\right), \tag{5.4}$$

$$(\mathbf{J} \times \mathbf{B})_y = 0\ , \tag{5.5}$$

$$(\mathbf{J} \times \mathbf{B})_z = \left[\frac{k_z}{s_0}(k_x^2 - k_z^2) - k_z \left(s_0 k_x^2 - \frac{k_z^2}{s_0}\right)\right] \times \frac{\sin(2k_x x)}{2} \exp\left(-\frac{2k_z z}{s_0}\right) \tag{5.6}$$

pushes oppositely directed segments of magnetic field lines toward each other, generating the neck at $t = 3.264$, panel (b) of the Figure 5.1—demonstrating the magnetic field line dynamics for $(\delta_i/L_0) = 0$. The reconnections at the neck generate the MFR—which we refer as the primary MFR (panel (c) of the Figure 5.1). Further evolution preserves the primary MFR by not allowing it to go through any internal reconnections. Notably, the rope loses its initial symmetry along the y direction by a marginal amount which, we attribute to the open boundary conditions. Nevertheless, the rope rises uniformly about a slightly inclined axis.

The magnetic field line evolution for $\delta_i/L = 0.04$ is exhibited in Figure 5.2. The selected value is on the order of the coronal value quoted in Introduction and optimizes the computation. The primary MFR develops at $t = 4$, which is similar to the instant at which the primary MFR was generated for the $\delta_i/L = 0$ case. The overall dynamics leading to the primary MFR also remains similar to the one without the Hall forcing. The similar dynamics and the near-simultaneity in the onset of the the primary MFR in both cases indicate the large scale dynamics, i.e.,

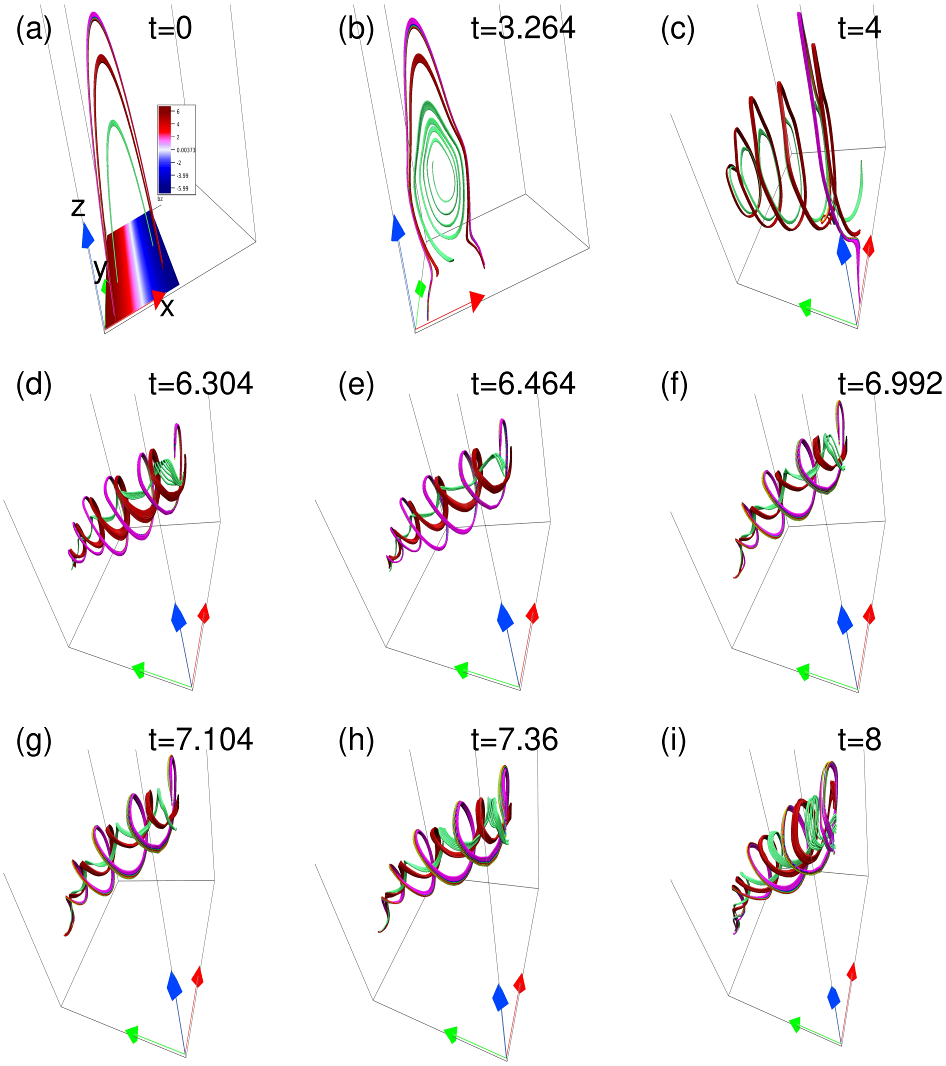

Figure 5.1: Panel (a) shows the initial bipolar sheared arcade configuration along with polarity inversion line, Panels (b) and (c) show the formation of magnetic flux rope. Panels (d) to (i) represent the further evolution of the magnetic flux rope with a tilted axis (along y) of it for $\delta_i/L = 0$ (MHD) case.

the dynamics before or away from reconnections, to be insensitive to the particular Hall forcing.

However, there are conspicuous differences between the MHD and Hall MHD realizations of the MFR morphology. In the Hall MHD case the primary MFR undergoes multiple internal reconnections highlighted in Figure 5.3, leading to magnetic field line morphologies which when projected favorably look like magnetic islands similar to those found in the sinusoidal simulation. A swirling motion is also observed; cf. panels (a) to (f) of Figure 5.3 . Noteworthy, swirling motion during evolution of a prominence eruption has been observed (Pant et al., 2018).

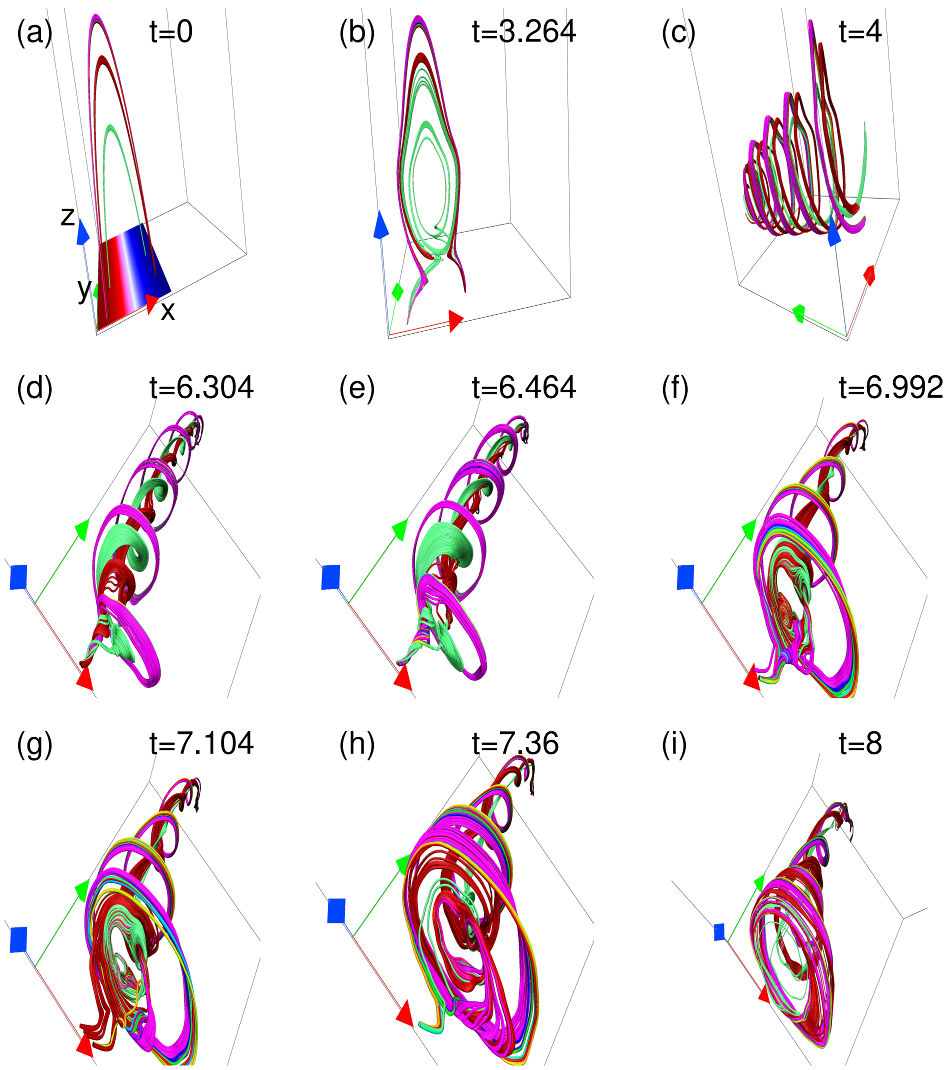

Figure 5.2: Panels (a) to (i) show the topology of magnetic field line s in their evolution for $\delta_i/L = 0.04$ under the Hall forcing. Important is the similarity of the dynamics leading to the formation of primary MFR which generates at a similar instant as the primary MFR in the absence of the Hall forcing.

To complete the analyses, we plot the overall evolution of magnetic and kinetic energies, amplitude of the out-of-plane field and the rate of change of the total volume current density in panels (c) and (d) of the Figure 5.4 The similarity of the energy curves in the presence and absence of the Hall forcing is a reminiscent of the fact that the Hall term does not affect the system energetics directly. Importantly, the out-of-plane magnetic field (approximated by the axial magnetic field B_y) is larger than that in the absence of the Hall forcing, in accordance with the expectation. Further, contrary to its smooth variation in the MHD case, the rate of change of total volume current density in Hall MHD goes through small

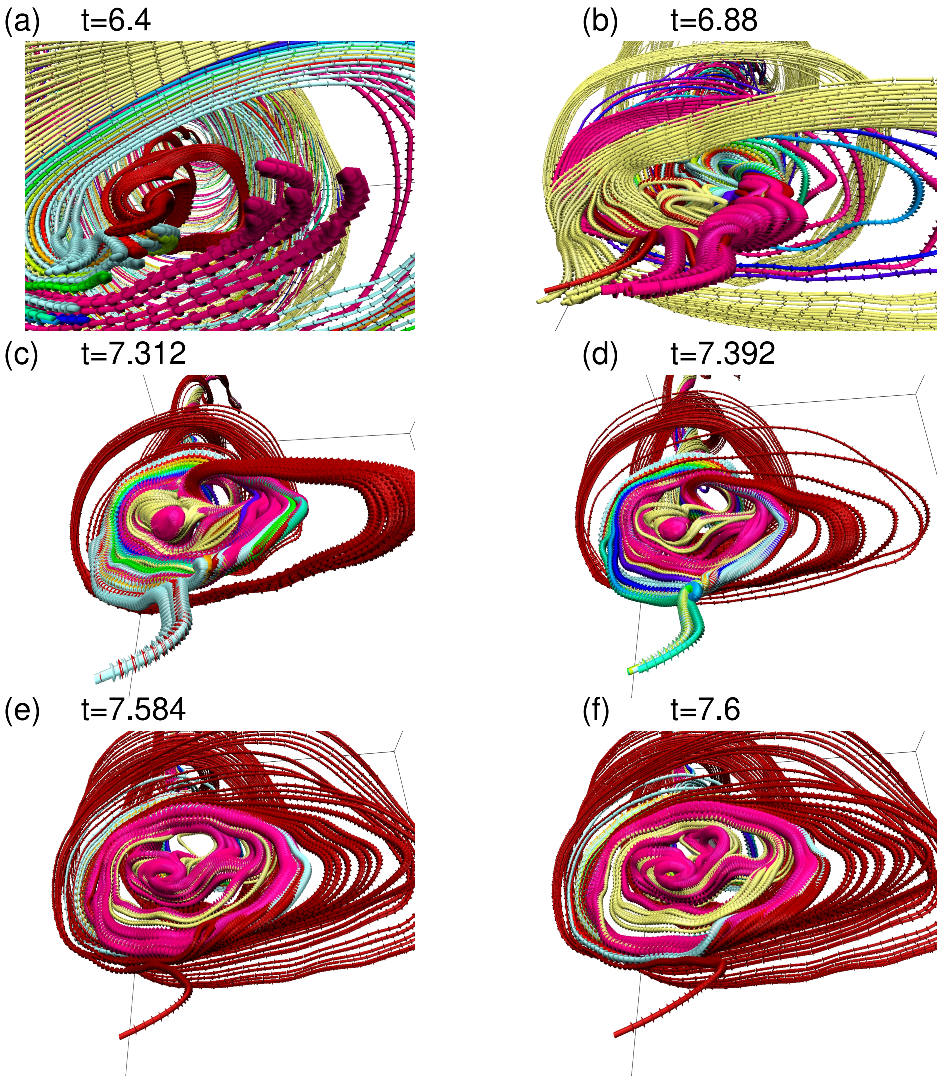

Figure 5.3: Sequence of magnetic field line evolution under the Hall forcing ($\delta_i/L = 0.04$ case), zoomed to reveal intricate magnetic topologies generated by the reconnections. Formation of the "figure 8" kind magnetic structures (panels (a) to panel (f))—the magnetic islands—can be seen clearly. Importantly, such intricate topologies are absent in the MFR evolution without the Hall forcing.

but abrupt changes. Such abrupt changes may correspond to a greater degree of impulsiveness (Bhattacharjee, 2004).

To check the dependence of the above findings on the grid resolution, we have carried out auxiliary simulations with $32 \times 32 \times 64$ grid resolution, spanning the same physical domain with all the other parameters kept identical (not shown). The findings are similar to those at the higher resolution. In particular, they evince the nearly simultaneous formation of the primary MFR, with and without the Hall forcing, through the similar dynamical evolution. Also, breakage of the

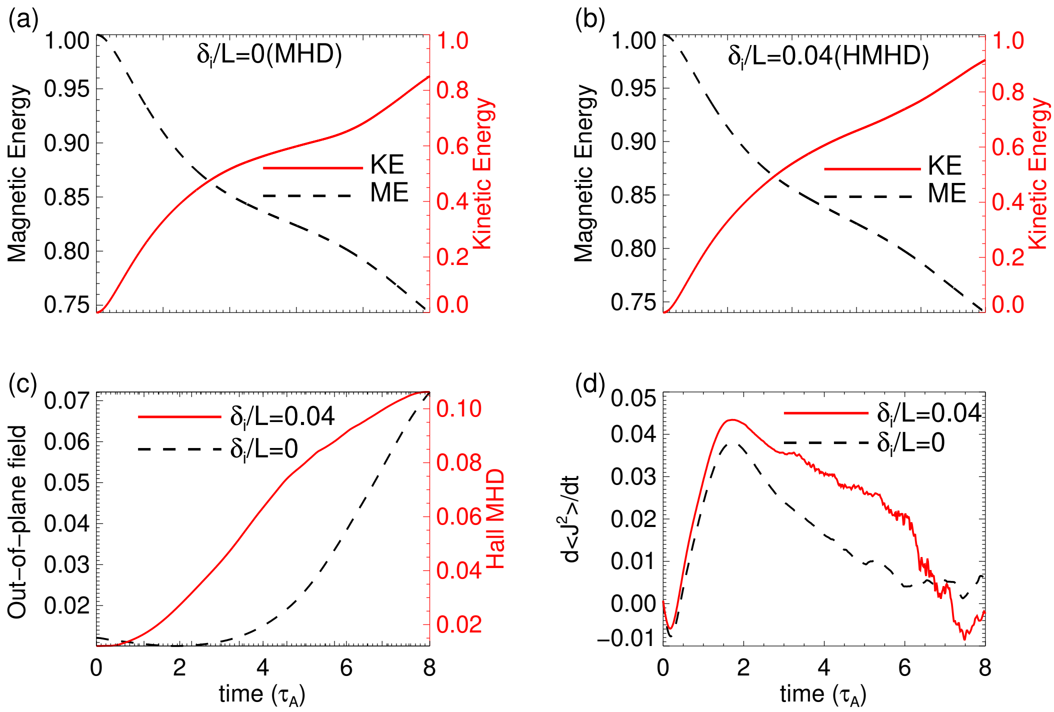

[a]

Figure 5.4: Panels (a) and (b) show the evolution of normalized (with the initial total energy) grid averaged magnetic energy (black dashed curve) and kinetic energy (red solid curve) for $\delta_i/L = 0$ (MHD) and $\delta_i/L = 0.04$ (Hall MHD) respectively. Panel (c) shows the evolution of grid averaged out-of-plane magnetic field for $\delta_i/L = 0$ (MHD) with black dashed curve and $\delta_i/L = 0.04$ (Hall MHD) with red solid curve respectively. Also in Panels (a) to (c), the scales for the solid and the dashed curves are spaced at right and left respectively. Panel (d) represents grid averaged rate of change of total current density for $\delta_i/L = 0$ (black dashed curve) and $\delta_i/L = 0.04$ (red solid curve) respectively. Important are the generation of the out-of-plane magnetic field along with small but abrupt changes in time derivative of the total volume current density in Hall MHD simulation.

[a]In this figure and hereafter in subsequent figures, HMHD acronym is used for Hall MHD.

primary MFR through internal reconnections is found in presence of Hall forcing whereas no such breakage is seen in the absence of the Hall forcing. The identical dynamics in two separate resolutions indicate the findings to be independent of the particular resolution used.

5.3 Case-II: MFR generated from a 3D initial analytical magnetic field

The magnetic field lines dynamics responsible for flares and CMEs are 3D owing to their inherent twist. It is then imperative to complement the above work by exploring Hall MHD evolution of an initially 3D magnetic configuration toward the creation and further evolution of MFR. For the purpose, a comprehensive analysis of 3D Hall-assisted magnetic reconnection during the evolution of an anchored MFR is presented here. Importantly, anchored MFRs are observationally more relevant to solar coronal transients than the non-anchored levitating ones, as idealized in Bora et al. (2021); Kumar et al. (2016). The simulations are initiated with a 3D bipolar sheared field (Kumar et al., 2016) $\mathbf{B}^*$ having a sigmoid shaped polarity inversion line (PIL) (shown in Figure 5.9). The $\mathbf{B}^* = \mathbf{B} + a_0\mathbf{B}^{'}$ where $\mathbf{B}$ is given by the Equation 5.1 - Equation 5.3 and $\mathbf{B}^{'}$ is

$$B_x^{'} = (\sin x \cos y - \cos x \sin y) \exp\left(\frac{-z}{s_0}\right) , \tag{5.7}$$

$$B_y^{'} = -(\cos x \sin y + \sin x \cos y) \exp\left(\frac{-z}{s_0}\right) , \tag{5.8}$$

$$B_z^{'} = 2s_0 \sin x \sin y \exp\left(\frac{-z}{s_0}\right) . \tag{5.9}$$

The parameters k_x, k_y, k_z and s_0 used in simulations are the same as mentioned for Case-I in Section 5.2.

Equation 4.1 - Equation 4.4 are numerically integrated using the 3D HMHD solver (already described in Chapter 3) to get the dynamical evolution of the 3D initial field given above.

The simulations are conducted by assuming the plasma to be incompressible, thermodynamically inactive, and explicitly nonresistive. A physical domain of extent [{0,2π}, {0,2π}, {0,8π}] is resolved by a computational domain of size 64×64×128, making the spatial step sizes $\Delta x = \Delta y$ =0.0997, and Δz =0.1979 (in dimensionless units). The simulations start with a motionless state, i.e. initial flow velocity field ($\mathbf{v}$) is set to zero. The mass density ρ_0 is set to 1 and the effective viscosity τ_A/τ_ν is set to 2×10^{-5}. All the parameters are same for the Hall MHD

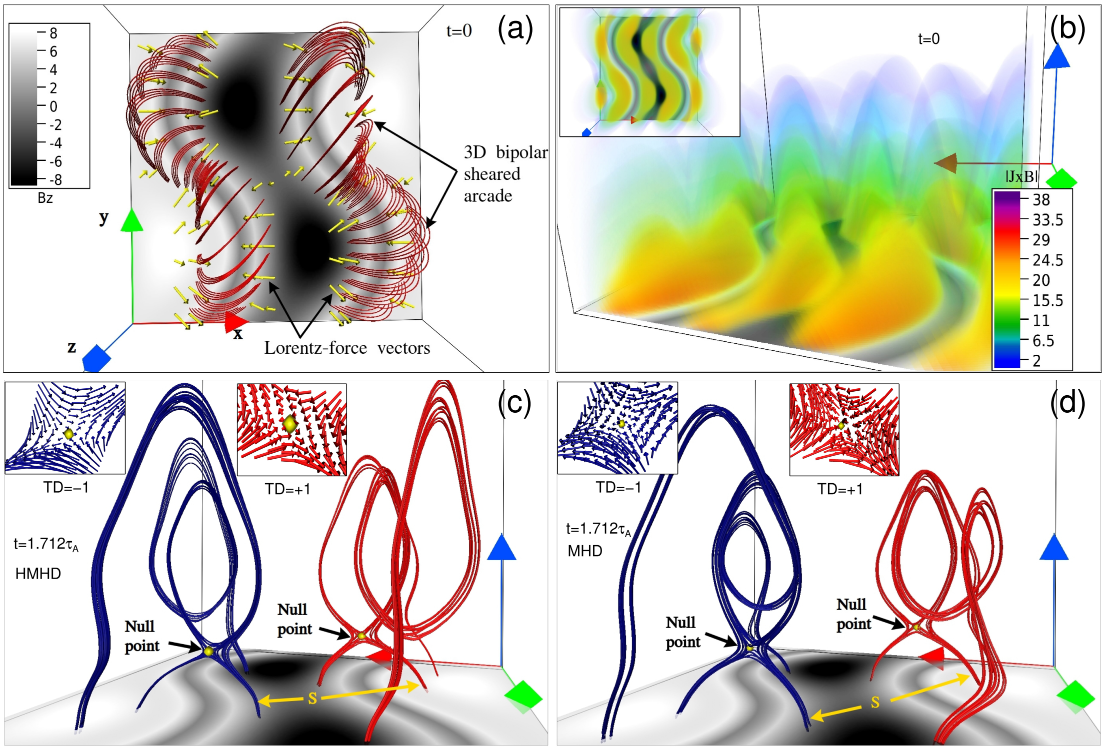

Figure 5.5: (a) Initial 3D sheared magnetic field lines (red) along with the oppositely directed Lorentz force vectors (yellow) around the sigmoid shaped polarity inversion line (PIL). (b) The magnitude of Lorentz force ($|\mathbf{J} \times \mathbf{B}|$) and its top-down view (inset image in the top left corner). (c) and (d) Two 3D nulls (yellow) of topological degrees -1 (blue) and +1 (red) during the Hall MHD and MHD simulations respectively. The spine is indicated by the yellow arrows. The bottom boundary in all the panels of this figure and subsequent figures shows the B_z maps in gray scale, where the lighter shade represents positive-polarity regions and the darker shade indicates the negative-polarity regions. The red, green and blue arrows in each panel represent the x, y and z axis of the Cartesian coordinate system respectively.

and MHD simulations except δ_i/L_0.

For the MHD simulation the value of δ_i/L_0 is set to 0. In conformity with the order of δ_i/L_0 in solar corona, it is set to 0.04 for the Hall MHD simulation. Notably, the ion inertial scales are greater than the dissipation scale (the spatial step sizes). As a result, reconnections because of both Hall effect and the MPDATA assisted residual dissipation are expected to be near-simultaneous in the presented simulations and onset with a steepening of current density.

The simulation results presented herein correspond to a total run of $7000\Delta t$ with the dimensionless temporal step size $\Delta t = 16 \times 10^{-4}$. The total simulated physical time is $7000\Delta t \tau_A = 11.2\tau_A$, where τ_A is in seconds. For the convenience, hereafter (including figures) the time is presented in units of τ_A. The B_z at the

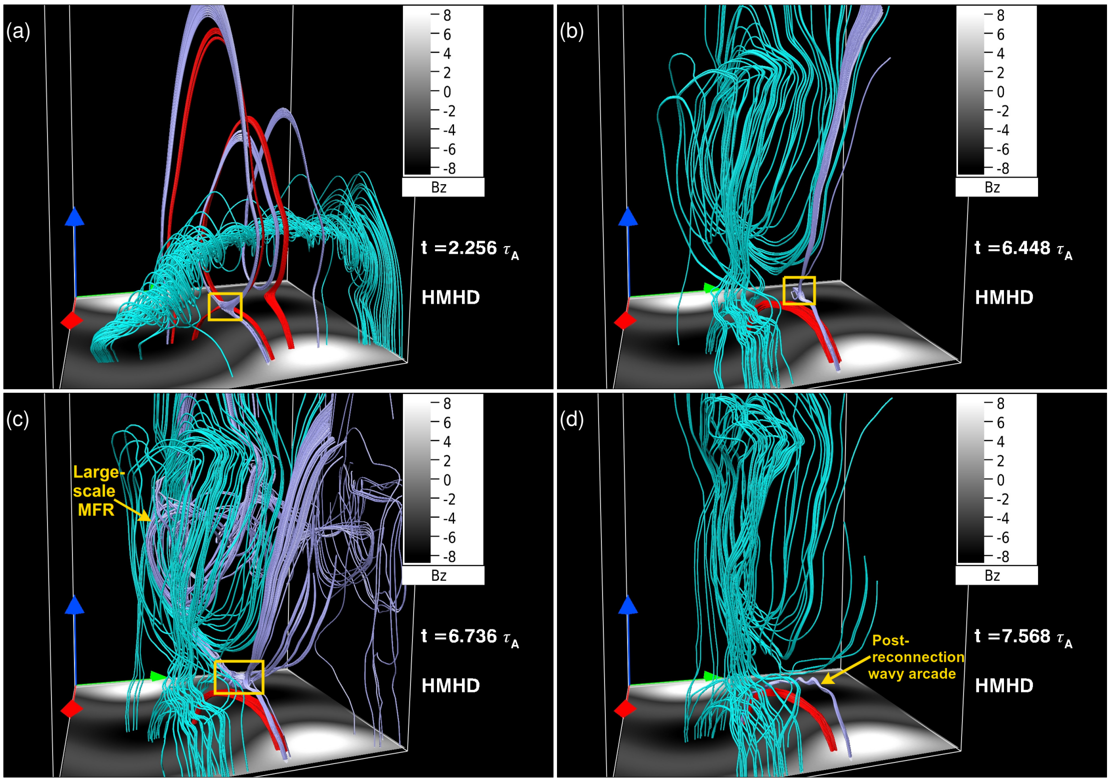

Figure 5.6: Snapshots from the Hall MHD evolution of a 3D MFR. (a) The two set of field lines (red from left and lavender from right side) approaching each other (marked in a yellow rectangular box) below the MFR (cyan color) at $t = 2.256\tau_A$. (b) Structure formed by lavender color magnetic field lines (maked in yellow rectangle) and the post reconnection arcade formed by red magnetic field lines at $t = 6.448\tau_A$. (c) Large-scale MFR formed by lavender color magnetic field lines and associated small-scale structure around reconnection site (marked in yellow rectangle) at $t = 6.736\tau_A$). (d) Post-reconnection wavy arcade generated by lavender magnetic field lines at $t = 7.568\tau_A$.

bottom boundary (at z = 0) is kept fixed throughout the simulation while all other field variables are allowed to vary. At all other boundaries, all variables including B_z, vary with time with their values at a given spatial location on the boundary being mapped from the immediate spatial neighborhood. Importantly, the boundary condition used here is entirely different from the periodic boundary used in Kumar et al. (2016) and allows for the generated flux rope to be anchored.

Our investigation of the reconnection sites toward the generation of initial MFR reveals the repetitive 3D reconnections occurring at null points in Hall MHD as well as MHD simulation. The presence and location of such null points is confirmed by utilizing the well established and tested trilinear method of null detection in three-dimensional vector space; see Haynes & Parnell (2007) for details. For the null detection we have used a python code based on trilinear method, developed

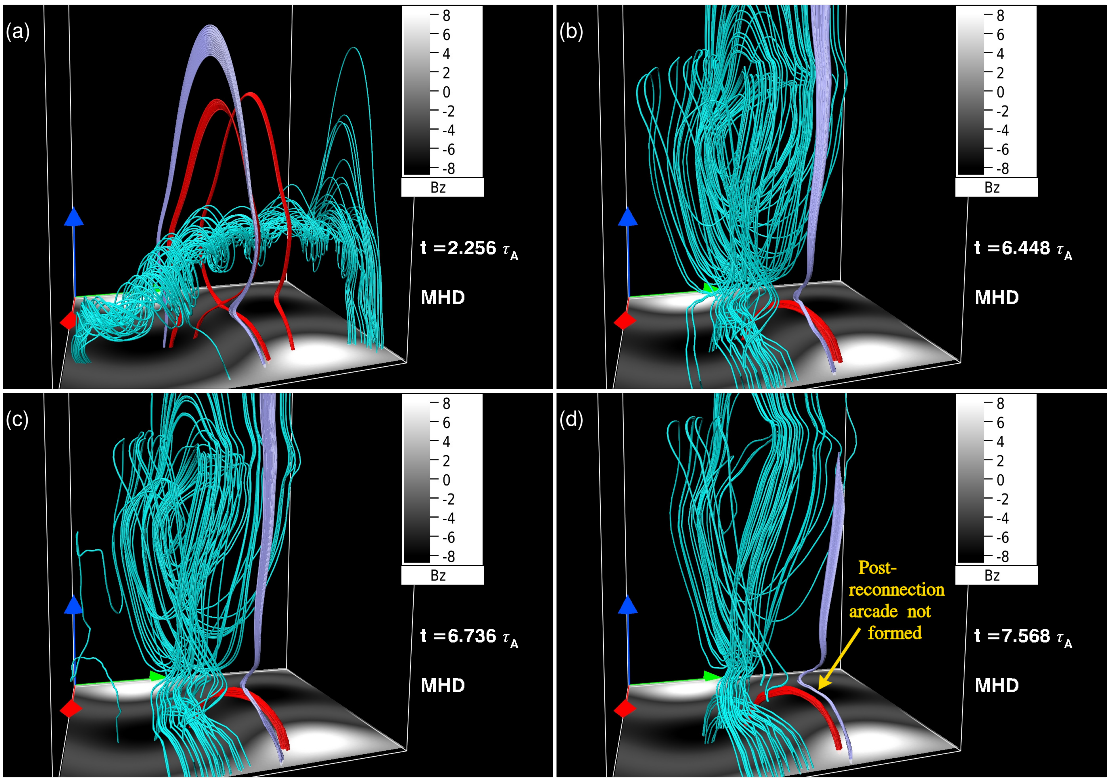

Figure 5.7: Snapshots from the MHD evolution of a 3D MFR. Panel (a) shows the MFR (cyan color) structure with two other sets of magnetic field lines (red and lavender) overlying the MFR. Notably, red and lavender color magnetic field lines are relatively farther compared to the Hall MHD instance of the same at $t = 2.256\tau_A$. Panels (b)-(d) highlight the morphology of lavender magnetic field lines. Noticeably, the lavender magnetic field lines do not exhibit any twisted structure formation near the reconnection site (cf. panels (b)-(d) of Figure 5.6.)

by Federica Chiti, David Pontin, Roger Scott and available at https://zenodo.org/record/4308622#.YByPRS2w0wc.

Null detection shows that there are no null points present initially at $t = 0$. The reconnections onset as the initial non-zero Lorentz force (direction and magnitude around the PIL is shown in the panels (a) and (b) of Figure 5.5) pushes the oppositely directed segments of magnetic field lines toward each other to generate the neck (panels (c) and (d) of Figure 5.5). At the neck the null points are detected and one such instance of the reconnections at null points from each simulation (at $t = 1.712\tau_A$) is presented in the panels (c) and (d) of Figure 5.5. Since there are no null points present at $t = 0$, the net topological degree is zero. Subsequently, careful analysis of the magnetic field vectors around null points reveals the blue magnetic field lines have topological degree -1 (magnetic field lines approaching the null along spine) while the red magnetic field lines have topological degree +1 (magnetic field lines receding from the null along spine); see Figure 5.5 (c) and (d). Hence the net topological degree is zero, implying the topological degree to be conserved (Wyper & Pontin, 2014) because the net topological degree is zero initially. Determining topological degree of all the nulls detected with trilinear method is difficult and beyond the scope of this work, since the maximum number of null points detected in Hall MHD is ≈ 650 and in MHD it is ≈ 500.

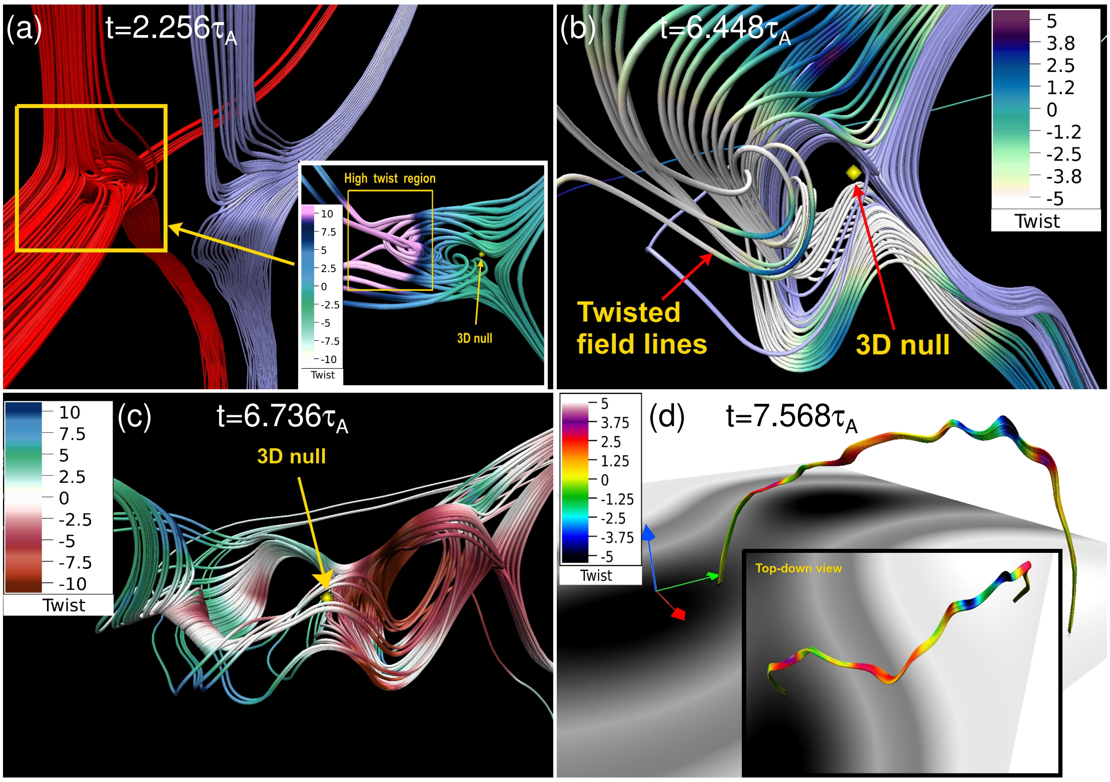

Figure 5.8: Detailed and zoomed view of the snapshots of magnetic structures marked in (a)-(d) of Figure 5.6. (a) Side view of the red and lavender magnetic field lines with the inset image showing the presence of a 3D null point and the associated twisted magnetic field lines left to the 3D null magnetic field lines morphology at $t = 2.256\tau_A$. magnetic field lines in inset image are the red magnetic field lines color coded with the twist ($\alpha = \mathbf{J}\cdot\mathbf{B}/|\mathbf{B}|^2$). (b)-(d) depict the instances from the Hall MHD evolution of lavender magnetic field lines. (b) Zoomed frontal view of the lavender magnetic field lines structure (marked in Figure 5.6(b)) highlighting the presence of a 3D null at $t = 6.448\tau_A$. Additional field lines (left to 3D null and color coded with α) show the twist value ≈ -5 around the 3D null. (c) Frontal view of the lavender magnetic field lines structure (color coded with twist) along with the 3D null at $t = 6.736\tau_A$. Notably, the magnetic field lines have twist $\alpha \approx -10$ on right and $\alpha \approx (5 - 7.5)$ on left to the 3D null. (d) Post-reconnection wavy arcade generated by lavender magnetic field lines (color coded with α) depicts the twist $\alpha \approx -5$ at $t = 7.568\tau_A$.

Noticeably, the initial magnetic field configuration is symmetric about $x = \pi$ (Figure 5(a)), i.e., in the $x =\in \{0, \pi\}$ and $x \in \{\pi, 2\pi\}$ domain. Dynamical evolution and structures are same about $x = \pi$; as evident from the panels (c) and (d) of Figure 5.5. Therefore, for relevant illustrations and to avoid much dynamical complications, we focus only in the $x \in \{\pi, 2\pi\}$ domain here.

Figure 5.6 and Figure 5.7 illustrate the instances of the evolution of selected magnetic field lines sets from the Hall MHD and MHD simulation respectively. To highlight the differences in the magnetic field lines dynamics around the reconnection sites and subsequent large scale structural changes, we compare panels (a)-(d) of Figure 5.6 and Figure 5.7. Panels (a) of Figure 5.6 and Figure 5.7 depict an identical twisted MFR (cyan color), overlying stretched field lines and the reconnection site below MFR during the Hall MHD and MHD simulations. An indistinguishable initial MFR creation in both the simulations is evident from panels (c) and (d) of Figure 5.5. However, the red and lavender magnetic field lines approach each other apparently during the Hall MHD (marked by yellow rectangle in Figure 5.5(a)) at $t = 2.256\tau_A$ but during the MHD the two magnetic field lines set are farther and red magnetic field lines reconnects with itself below the MFR. Panels (b) of Figure 5.6 and Figure 5.7 show the similarity of cyan color MFR and red magnetic field lines post reconnection arcade during the Hall MHD and MHD simulations respectively. It is only the lavender magnetic field lines which exhibit different structures during the Hall MHD and MHD from $t = 6.448\tau_A$ onwards, hence we focus mainly on the instances of lavender magnetic field lines dynamics in panels (c) and (d) of Figure 5.6 and Figure 5.7 further. Panels (c) of Figure 5.6 and Figure 5.7 depict the main difference in the lavender magnetic field lines structure, since during the Hall MHD at $t = 6.736\tau_A$ the lavender magnetic field lines has formed a large-scale MFR (marked by yellow arrow in Figure 5.6(c)) with the associated twisted magnetic field lines region below MFR (marked by yellow rectangle in Figure 5.6(c)). Contrary to the Hall MHD, Figure 5.7(c) depicts no large scale MFR formation by lavender magnetic field lines. Notably, panels (d) of Figure 5.6 and Figure 5.7 show the post-reconnection arcade (Lavender magnetic field lines marked with yellow arrow) in the Hall MHD simulation develops earlier than in the MHD simulation which, yet lacks the arcades to get developed by $t = 7.568\tau_A$. A faster development of a post-reconnection arcade clearly indicates faster reconnection dynamics in Hall MHD.

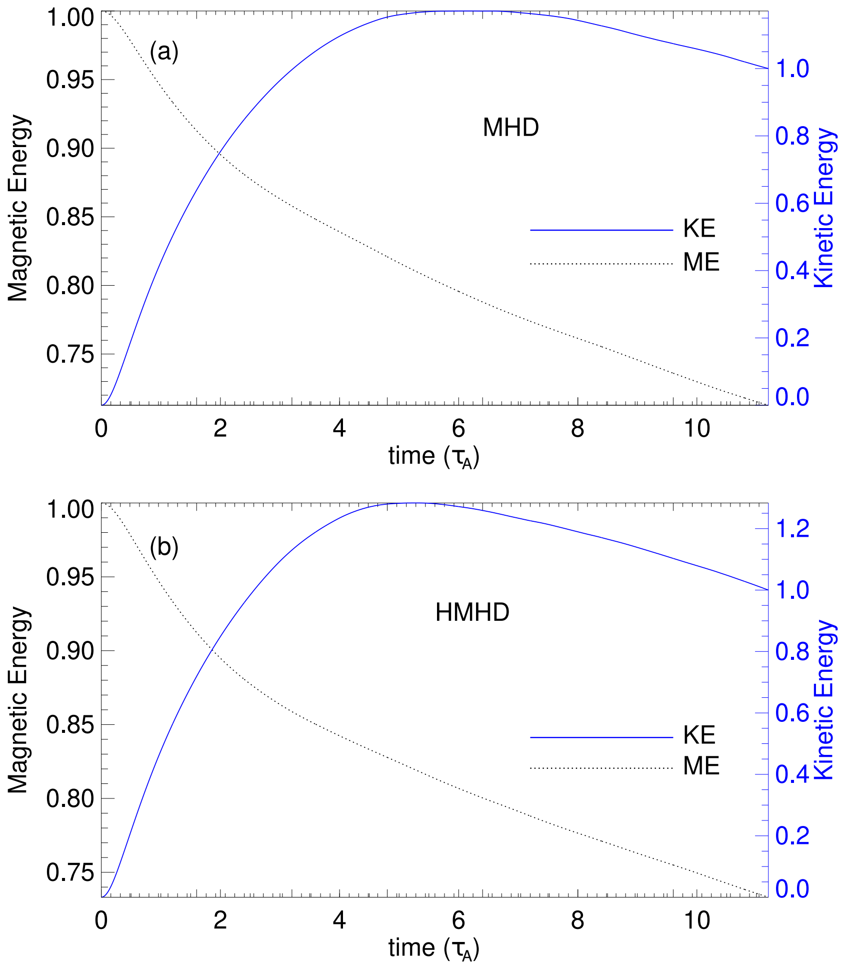

Figure 5.9: Panels (a) and (b) show the temporal variation of the volume averaged magnetic (black dashed curve) and kinetic energies (blue solid curve) during the MHD and Hall MHD evolution respectively.

All the differences mentioned above are purely on the basis of magnetic field lines dynamics and structural changes around possible reconnection sites, which we further analyze using the trilinear method of null points detection and twist analysis. In Figure 5.8, we present the detailed zoomed view of the magnetic field lines morphology marked in the Figure 5.6. Panel (a) shows the red and lavender magnetic field lines sets, depicting the red magnetic field lines to be twisted. Inset image in panel (a) shows the frontal view of red magnetic field lines (color coded with the twist $\alpha = \mathbf{J} \cdot \mathbf{B}/|\mathbf{B}|^2$) around the null point (yellow point marked by arrow) with coordinates x =45.7114, y =30.4794, and z =9.0157. Notably, the field lines are twisted on the left to null point with the twist value $\alpha \approx 10$. Since the red magnetic field lines forms the post-reconnection arcade by $t = 6.448\tau_A$ and does not reconnect further, so we drop it and focus on the dynamics of lavender magnetic field lines in panels (b)-(d) of Figure 5.8. In panel (b), we present the zoomed frontal view of lavender magnetic field lines and mark the presence of detected null point at x =53.2595, y =32.5542, and z =14.0096 location within it. Additional field lines are shown around the null point which depict the twist $\alpha \approx -5$ near the null point. Panel (c) highlights the front view of magnetic field lines (marked in rectangular box in Figure 5.6(c)). magnetic field lines are color coded with the twist values. A null point was detected at x =51.3722, y =32.0806, and z =13.5316 location using the trilinear method and marked by the yellow arrow in the figure. magnetic field lines show a high twist value $\alpha \approx -10$ right to the null point. The lavender color large-scale MFR (Figure 5.6(c)) is formed as a result of reconnections in the region shown in Figure 5.8(c). Finally, panel (d) shows the same post-reconnection wavy arcade marked in Figure 5.6(d) along with the twist value $\alpha \approx -5$. Notably, the post-reconnection arcade is twisted. Interestingly, if the twisted magnetic field lines confine plasma, they are usually observed as filament (against solar disk) or prominence (against solar limb) on the Sun.

Temporal variation of the volume averaged magnetic and kinetic energies is presented in the panels (a) and (b) of Figure 5.9. The solid blue and dashed black curves represent the kinetic and magnetic energy variations respectively. Noticeably, the magnetic energy is decreasing identically in both the simulations, hence the results are in agreement with the general theoretical expectation that the Hall effect do not cause changes in the magnetic energy dissipation rates (Liu et al., 2022).

In summary, ubiquitous twisting of magnetic field lines in the vicinity of null points is unique to the Hall MHD evolution of the 3D MFR. Owing to the local enhancements of the strong gradients of magnetic field, the Hall effects cause magnetic field lines morphological changes, (e.g., twisting) around the reconnection sites which further affects the large-scale dynamics during the Hall MHD simulations.

5.4 Summary

In this Chapter, for the first time, the newly developed 3D HMHD EULAG model has been employed to investigate the Hall effect on magnetic reconnections during the evolution of MFR. Particularly, the topological changes during the MFR creation and evolution are analyzed in the presence and absence of Hall term in the induction equation. Following the model equations, simulations presented in this Chapter use dimensionless set of equations along with the description of normalization. A detailed analysis of the magnetic reconnections for the MFRs generated from two sets of initial conditions is carried out. The results presented in this Chapter, clearly depict that the initial MFR formation mechanism through reconnections is identical in the Hall MHD as well as MHD, but the further evolution in two simulations is illustrious in terms of repetitive formation of intermediate structures during the Hall MHD evolution. Key highlights of the work presented in this Chapter include the faster, efficient and complex reconnections during the Hall MHD simulation and identical volume averaged temporal evolution of magnetic and kinetic energies in the Hall MHD and MHD simulations. The reconnections in our simulations occur owing to the numerical dissipation of the under-resolved magnetic field variables (ILES property of the model, described in Chapter 3). These reconnections being intermittent and local, successfully mimic the physical reconnections. Since the dissipation and Hall scales are tied together in the model. As the current density or magnetic field gradients enhance at the dissipation scale it introduces additional slippage of field lines in Hall MHD (Bora et al., 2022) over MHD (due to the Hall term) and, may be responsible for more efficient and faster reconnections found in the Hall simulations reported in this Chapter.

At last, we want to emphasize ~~on~~ the fact that we have only considered the Hall effect on magnetic reconnections during the evolution of MFR generated through the reconnections from an initially bipolar sheared magnetic arcades. Whereas, presently, there are two different concepts of CMEs on the Sun; one considers that the MFR is absent prior to eruption and it is eventually generated through magnetic reconnections (tether cutting or breakout models); another assumes the pre-existence of MFR emerged from below the photosphere (i.e., from the convection zone) undergoes the ideal MHD instabilities (torus and kink instabilities) which initiate eruptions. Available observations of the CMEs on Sun suggest the possibility of both the ideas. Regardless of which idea is admissible in the real eruptions on Sun, general agreement is that the reconnection shapes the erupting dynamic MFR. In order to understand the CMEs happening due to the successful prominence or filament eruption, is then crucial to also investigate the role of Hall forcing on magnetic reconnetctions driving the dynamics of a pre-existing 3D MFR further.

Chapter 6

Data-based Hall MHD and MHD simulations of a flaring solar active region

6.1 Introduction

In Section 1.6, a straightforward calculation based on observed impulsive rise time of hard X-ray emission ($\approx$ few minutes) during the solar flares, suggests that reconnection length scale is of the order of few tens of meters in the solar corona. An order-of-magnitude analysis of the induction equation at reconnection scale length indicates the inevitability of Hall effects during dissipative processes or magnetic reconnection on the Sun (Bhattacharjee, 2004; Bora et al., 2021). Chapter 5 clearly illustrates that contrary to the standard MHD, presence of the Hall term leads to faster reconnection while also capturing the effects of small-scale processes over large length scale magnetic field line dynamics. Modeling magnetic reconnection in solar corona at small length scales and capturing its effects on large scale dynamics together is challenging and is an open problem. It is compelling to study the Hall MHD evolution in a more realistic scenario with the initial magnetic field obtained from a solar magnetogram. In this Chapter, we present the data-based Hall MHD and MHD simulations of a flaring solar active region as a test bed. The main objective of this work is to explore significance of the Hall effect on magnetic reconnection to understand the spatiotemporal development of the observed solar flare ribbon brightening. To attain the objective, we select the recently reported active region (AR) NOAA 12734 by Joshi et al. (2021) that produced a C1.3 class flare. In absence of reliable direct measurement of the coronal vector magnetic field, several extrapolation models such as nonlinear force-free field (NLFFF) (Wiegelmann, 2008; Wiegelmann & Sakurai, 2012) and non-force-free field (non-FFF) (Hu & Dasgupta, 2008; Hu et al., 2010) have been developed to construct the coronal magnetic field using photospheric magnetograms. The standard is the NLFFF, and the recent data-based MHD simulations initialized with it have been reasonably successful in simulating the dynamics of various coronal transients (Jiang et al., 2013; Amari et al., 2014; Inoue et al., 2014; Savcheva et al., 2016). However, the NLFFF extrapolations require to treat the photosphere as force-free, while it is actually not so (Gary, 2001). Hence, a "preprocessing technique" is usually employed to minimize the Lorentz force on the photosphere in order to provide a boundary condition suitable for NLFFF extrapolations (Wiegelmann et al., 2006b; Jiang & Feng, 2014) and thereby artificially modifying the photosphere. Recently, the non-Force Free Field (non-FFF) model, based on the principle of minimum energy dissipation rate (Bhattacharyya & Janaki, 2004; Bhattacharyya et al., 2007), has emerged as a plausible alternative to the force-free models (Hu & Dasgupta, 2008; Hu et al., 2008, 2010). In the non-FFF model, the magnetic field **B** satisfies the double-curl-Beltrami equation (Mahajan & Yoshida, 1998) and the corresponding Lorentz force on the photosphere is non-zero while it decreases to small values at the coronal heights (Prasad et al., 2018; Nayak et al., 2019; Prasad et al., 2020)—concurring with the observations. In this Chapter, we use non-FFF extrapolation (Hu et al., 2010) to obtain the magnetic field in corona using the photospheric vector magnetogram obtained from the Helioseismic Magnetic Imager (HMI) (Schou et al., 2012) onboard the Solar Dynamics Observatory (SDO) (Pesnell et al., 2012b).

The Chapter is organized as follows. Section 6.2 describes the flaring event in AR NOAA 12734, Section 6.3 presents magnetic field lines morphology of AR NOAA 12734 along with the preferable sites for magnetic reconnections such as QSLs, 3D null point, and null-line found from the non-FFF extrapolation. Section 6.4 focuses on the numerical model, numerical set-up and the evolution of magnetic field lines obtained from the extrapolation along with their realizations in observations. Section 6.5 highlights the key findings.

6.2 Salient features of the observed C1.3 class flare in AR NOAA 12734

The AR NOAA 12734 produced an extended C1.3 class flare on March 08, 2019 (Joshi et al., 2021). The impulsive phase of the flare started at 03:07 UT as reported in the Figure 3 of Joshi et al. (2021) and also shown in the Figure 6.1, which shows the X-ray flux in the 1-8 Å and 0.5-4 Å detected by the Geostationary Operational Environmental Satellite (GOES) (Garcia, 1994). The flux evinces two subsequent peaks after the onset of the flare, one around 03:19 UT and another roughly around 03:38 UT. Joshi et al. (2021) suggested the eruptive event to take place in a coronal sigmoid with two distinct stages of energy release.

Additional observations using the multi-wavelength channels of Atmospheric Imaging Assembly (AIA) (Lemen et al., 2012) onboard SDO are listed below to highlight important features pertaining to simulations reported in this Chapter. Figure 6.2 illustrates a spatio-temporal observational overview of the event. Panel (a) shows the remote semicircular brightening (C1) prior to the impulsive phase of the flare (indicated by the yellow arrow). Panels (b) to (d) indicate the flare by yellow arrow and the eruption by the white arrow in the 94 Å, 171 Å, and 131 Å channels respectively. Notably, the W-shaped brightening appears in panels (b) to (d) along with the flare in different wavelength channels of SDO/AIA. Panel (e) shows the circular structure of the chromospheric material (C2) during the impulsive phase of the flare. It also highlights the developed W-shaped flare ribbon (enclosed by the white box) which has a tip at the center (marked by the white arrow). Panel (f) depicts the post-flare loops in 171 Å channel, indicating the post-flare magnetic field line connectivity between various negative and positive polarities on the photosphere.

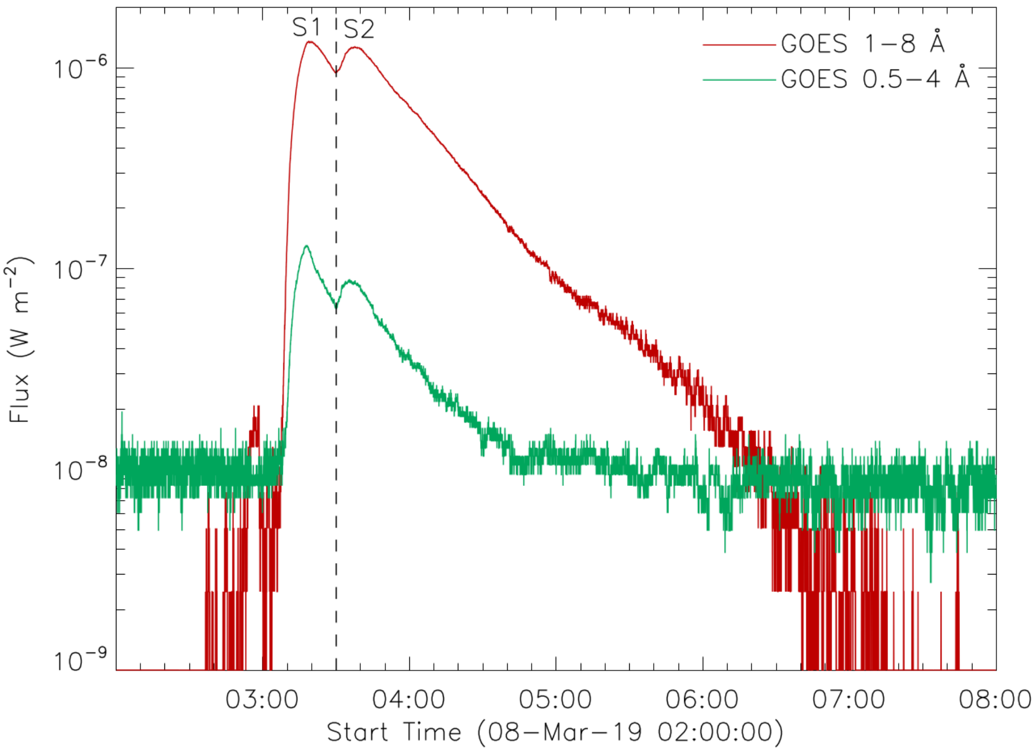

Figure 6.1: GOES light curves showing the evolution of an extended C-class flaring activity in active region NOAA 12734. The red and green lines indicate X-ray flux in 1-8 Å and 0.5-4 Å wavelength bands which correspond to disk-integrated X-ray emission in 1.5-12.5 keV and 3-25 keV energy range, respectively. GOES profiles reveal two distinct episodes of energy release (marked as S1 and S2) that peak at 03:19 and 03:38 UT, respectively, implying two-step process of energy release.

6.3 Coronal magnetic field construction and the morphology of AR NOAA 12734

As stated in Chapter 2, the non-FFF extrapolation technique proposed by Hu & Dasgupta (2008) and based on the minimum dissipation rate theory (MDR) (Bhattacharyya & Janaki, 2004; Bhattacharyya et al., 2007) is used to obtain the coronal magnetic field for the AR NOAA 12734. The vector magnetogram is selected for 2019 March 08, at 03:00 UT ($\approx$ 7 minutes prior to the start of flare). The original magnetogram cut out of dimensions 342×195 pixels with pixel resolution 0.5 arcsec per pixel having an extent of 124 Mm $\times$ 71 Mm from "hmi.sharp_cea_720s" series is considered, which ensures an approximate magnetic flux balance at the bottom boundary. To optimize the computational cost with the available resources, the original field is re-scaled and non-FFF extrapolated over a volume of $256\times128\times128$ pixels while keeping the physical extent same and preserving all magnetic struc-

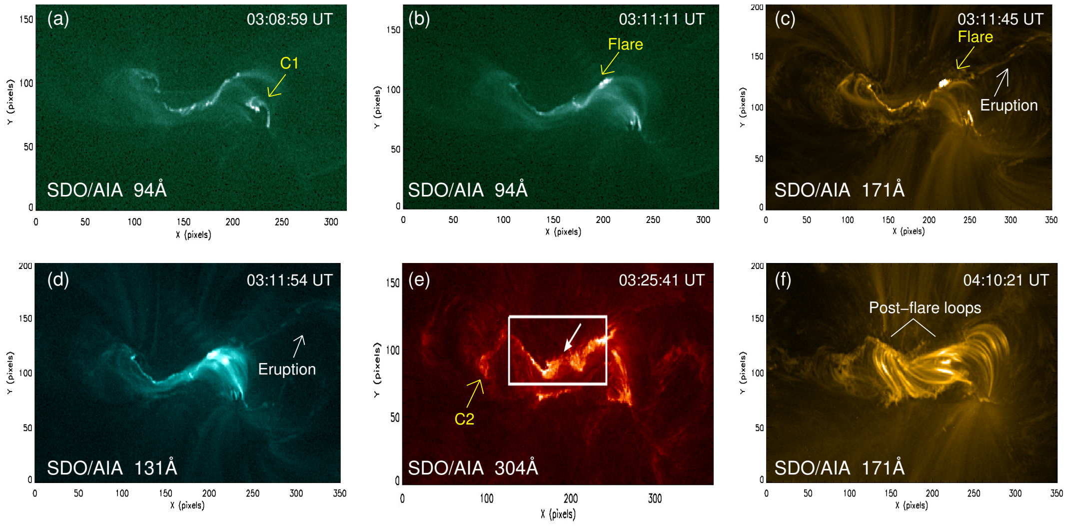

Figure 6.2: Panels (a)-(f) are SDO/AIA images showing the multi-wavelength observations of the flaring active region AR NOAA 12734. Panel (a) shows the quasi circular brightening at the western part of AR prior to the flare (marked by C1). Panels (b)-(d) show the initiation of the flare followed by eruption (indicated by yellow arrow). Panel (e) shows the circular structure after eruption at the eastern part of AR (marked by C2) and the W-shaped flare ribbon (enclosed by white box). Panel (f) shows the post-flare loops.

tures throughout the region. The reduction, in effect, changes the conversion factor of 1 pixel to $\approx$ 0.484 Mm along x and $\approx$ 0.554 Mm along y and z directions of the employed Cartesian coordinate system.

Panel (a) of Figure 6.3 shows E_n in the transverse field, defined in Section 2.2.2, as a function of number of iterations. It shows that E_n tends to saturate at the value of $\approx$0.22. Panel (b) of Figure 6.3 shows logarithmic decay of the normalized horizontally averaged magnetic field, current density, and Lorentz force with height. It is clear that the Lorentz force is appreciable on the photosphere but decays off rapidly with height, agreeing with the general perception that the corona is force-free while the photosphere is not (Liu et al., 2020; Sarp Yalim et al., 2020). Panel (c) shows that the Pearson-r correlation between the extrapolated and observed transverse fields is $\approx$0.96, implying strong correlation. The direct volume rendering of the Lorentz force in panel (d) also reveals a sharp decay of the Lorentz force with height, expanding on the result of panel (b).

To facilitate description, Figure 6.4 (a) shows the SDO/AIA 304 Å image at 03:25 UT, where the flare ribbon brightening has been divided into four segments marked as B1-B4. Figure 6.4 (b) shows the initial global magnetic field line mor-

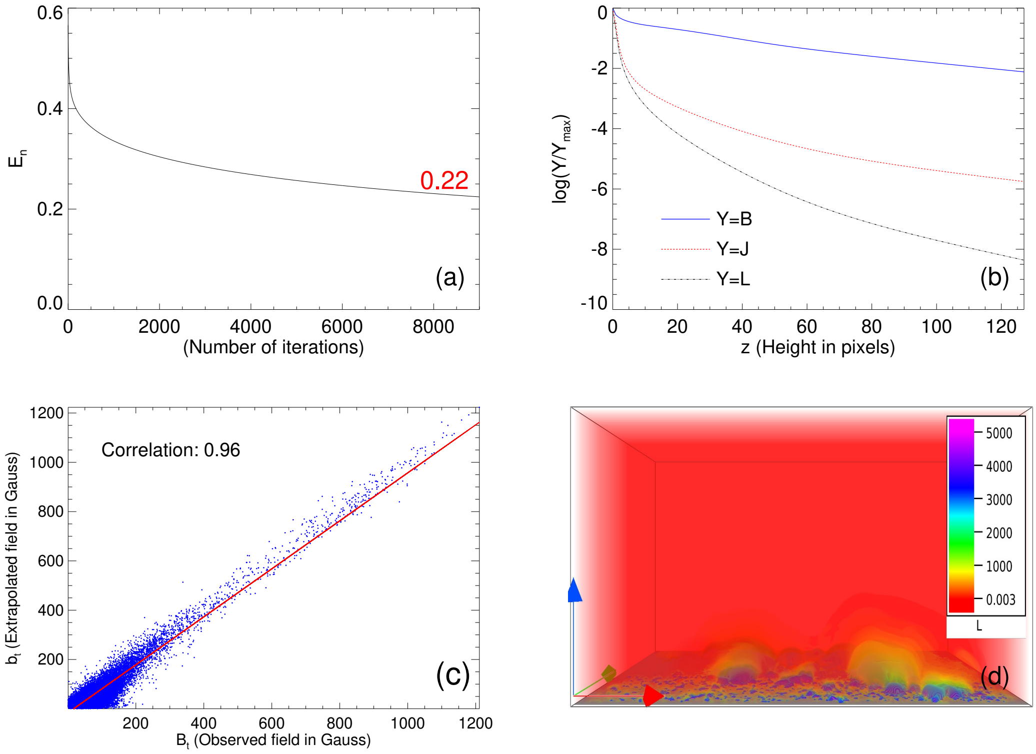

Figure 6.3: Panel (a) shows the variation of the deviation E_n with number of iterations in non-FFF extrapolation. Panel (b) shows the logarithmic variation of horizontally averaged magnetic field (Y=B), the current density (Y=J), and the Lorentz force (Y=L) with height z in pixels. All the quantities plotted in panel (b) are normalized with their respective maximum values. Panel (c) shows the scatter plot of the correlation between the observed and extrapolated magnetic field. The red line is the expected profile for perfect correlation. Distribution of the magnitude of the Lorentz-force for initial extrapolated field is shown in panel (d) using direct volume rendering (DVR). The distribution clearly shows that the Lorentz-force is maximum at bottom boundary and decreasing with the height in computational volume. The red, green and blue arrows on the bottom left corner represent x, y and z directions respectively here and hereafter. The color bars on the right side of the panel represent the magnitude of the strength of Lorentz-force .

phology of AR NOAA 12734, partitioned into four regions R1-R4, corresponding to the flare ribbon brightening segments B1-B4. The bottom boundary of panel (b) comprises of B_z maps in grey scale where the lighter shade indicates positive polarity regions and the darker shade marks the negative polarity regions. The magnetic field lines topologies and structures belonging to a specific region and contributing to the flare are documented below.

Region R1: The top-down view of the global magnetic field line morphology is shown in the panel (a) of Figure 6.5. To help locate QSLs, the bottom boundary

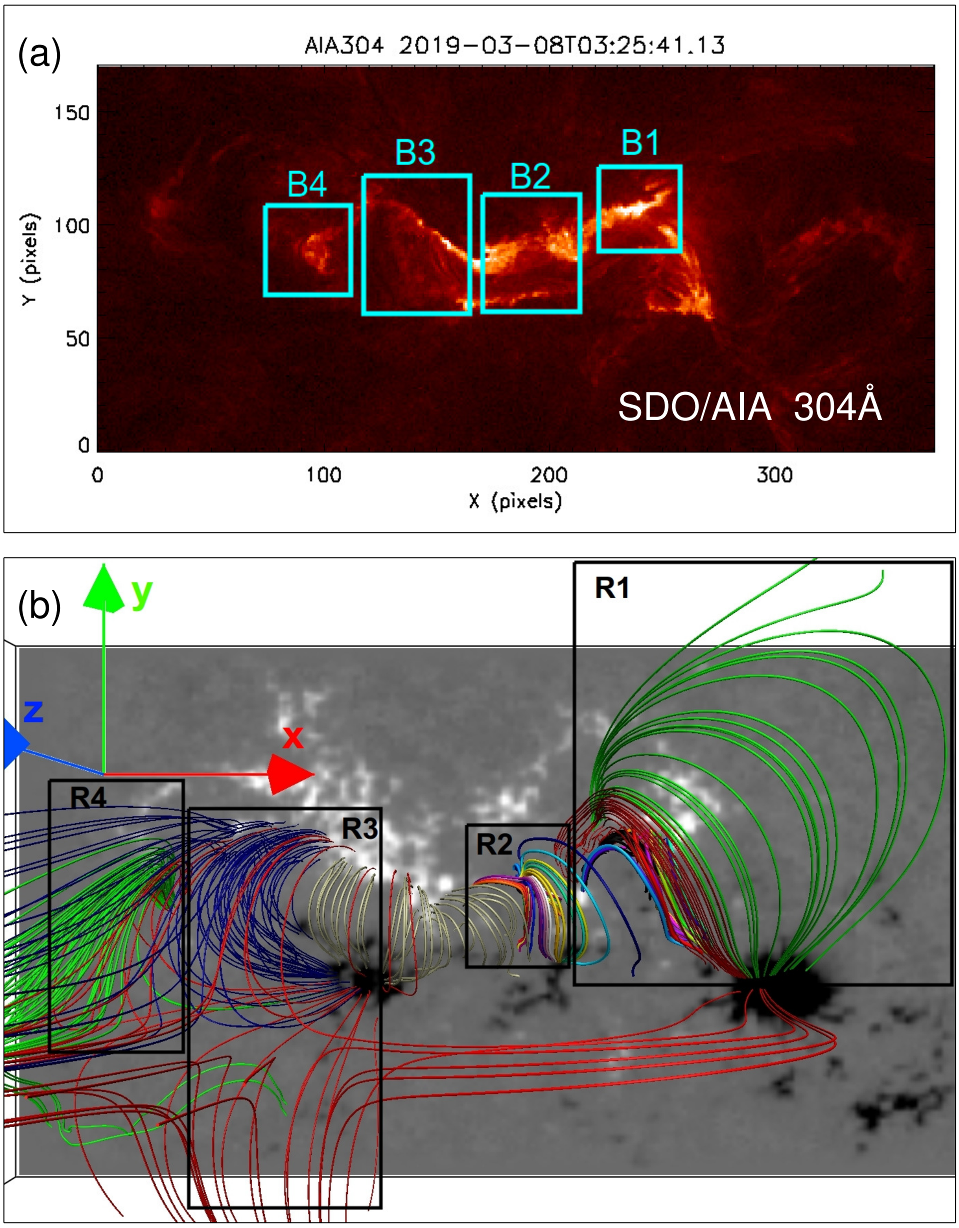

Figure 6.4: Panel (a) shows the SDO/AIA 304Å image where the flare ribbon brightening has been divided into four parts B1, B2, B3, and B4 (enclosed by boxes). Panel (b) shows an overall extrapolated magnetic field lines morphology of AR NOAA 12734 with the B_z-component of magnetogram at the bottom boundary. Foot points of the magnetic structures contained in regions R1, R2, R3, and R4 correspond to the brightening B1, B2, B3, and B4 respectively.

is overlaid with the $\log Q$ map of the squashing factor Q (Liu et al., 2012) in all panels of the figure. Distribution of high Q values along with B_z on the bottom boundary helps in identifying differently connected regions. The region with a large Q is prone to the onset of slipping magnetic reconnections (Démoulin, 2006).

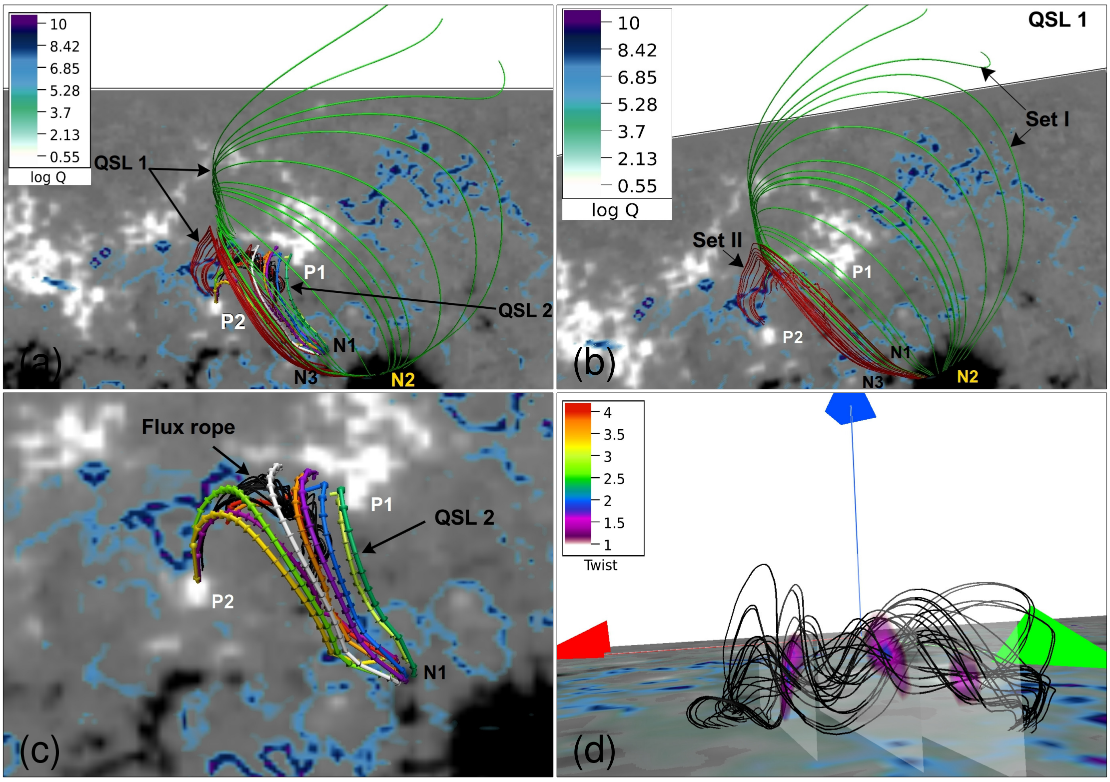

Figure 6.5: Panel (a) shows magnetic field lines morphology of region R1 between positive and negative polarities P1, P2, N1, N2, and N3 respectively. Panel (b) highlights the structure of QSL 1 comprised of magnetic field lines Set I (green) and Set II (maroon). Panel (c) shows the zoomed top view of the flux rope structure (black) and an overlying QSL 2 (multi color arrowed magnetic field lines), between the positive and negative polarities P1, P2, and N1 respectively. Panel (d) shows the side view of the flux rope where three vertical planes along the cross section of the flux rope show the twist value T_w at different locations along the flux rope. In all the panels the log Q between 5 and 10, is overlaid on B_z−component of magnetogram at the bottom boundary.

Foot points of magnetic field lines constituting QSL1 and QSL2 trace along the high Q values near the bottom boundary. QSL1, involving the magnetic field lines Set I (green) and Set II (maroon), is shown in panel (b). Particularly, magnetic field lines Set I (green) extends higher in the corona forming the largest loops in R1. Panel (c) illustrates a closer view of QSL2 (multicolored) and the flux rope (black) beneath, situated between the positive and negative polarities P1, P2 and N1, respectively. In panel (d), the flux rope (constituted by the twisted black magnetic field lines) is depicted using the side view. The twist value T_w (Liu et al., 2012) in the three vertical planes along the cross section of the flux rope is also overlaid. Notably, the twist value is 2 at the center of the rope and decreases outward (cf. vertical plane in middle of the flux rope in panel (d)).

Region R2: Figure 6.6 (a) shows the side view of a 3D null point geometry of magnetic field lines and the bottom boundary B_z overlaid with log Q ranging between 5 and 10. Panel (b) depicts an enlarged view of the 3D null location, marked black. The height of the null is found to be ≈ 3 Mm from the photosphere. The null is detected using the bespoke procedure (Kumar & Bhattacharyya, 2011; Nayak et al., 2020) that approximates the Dirac delta on the grid as

$$n(B_i) = \exp\left[-\sum_{i=x,y,z}(B_i - B_o)^2/d_o^2\right] , \tag{6.1}$$

where small constants B_o and d_o correspond to the isovalue of B_i and the Gaussian spread. The function $n(B_i)$ takes significant values only if $B_i \approx 0\ \forall i$, whereupon a 3D null is the point where the three isosurfaces having isovalues $B_i = B_o$ intersect.

Region R3: Side view of the magnetic field line morphology in region R3 is shown in Figure 6.6 (c), where the yellow surface corresponds to $n = 0.9$. Panel (d) highlights a “fish-bone-like” structure, similar to the schematic in Figure 5 of Wang et al. (2014). To show that in the limiting case $n = 0.9$ reduced to a null line, we plot corresponding contours in the range $0.6 \leq n \leq 0.9$ on three pre-selected planes highlighted in panel (e). The size reduction of the contours with increasing n indicates the surface converging to a line. Such null lines are also conceptualized as favorable reconnection sites (Wang et al., 2014).

Region 4 Figure 6.6 (f) shows magnetic field lines relevant to plasma rotation in B4. Notably, the null line from the R3 intrudes into R4 and the extreme left plane in R3 (Figure 6.6 (e)) is also shared by the R4.

6.4 Results: Comparison of the magnetic reconnections in the Hall MHD and MHD simulations of the flaring active region NOAA 12734

In the spirit of earlier related works (Prasad et al., 2018; Nayak et al., 2019; Prasad et al., 2020), the plasma is idealized to be incompressible and thermodynamically inactive as well as explicitly nonresistive. While this relatively simple idealization is naturally limited, it exposes the basic dynamics of magnetic reconnections unobscured by the effects due to compressibility and heat transfer. Albeit the latter are important for coronal loops (Ruderman & Roberts, 2002), they do not directly affect the magnetic topology—in focus of this Chapter. Historically rooted in classical hydrodynamics, such idealizations have a proven record in theoretical studies of geo/astrophysical phenomena (Rossby et al., 1938; Dahlburg et al., 1991; Bhattacharyya et al., 2010; Bora et al., 2021). Inasmuch as their cognitive value depends on an a posteriori validation against the observations, the present study offers yet another opportunity to do so.

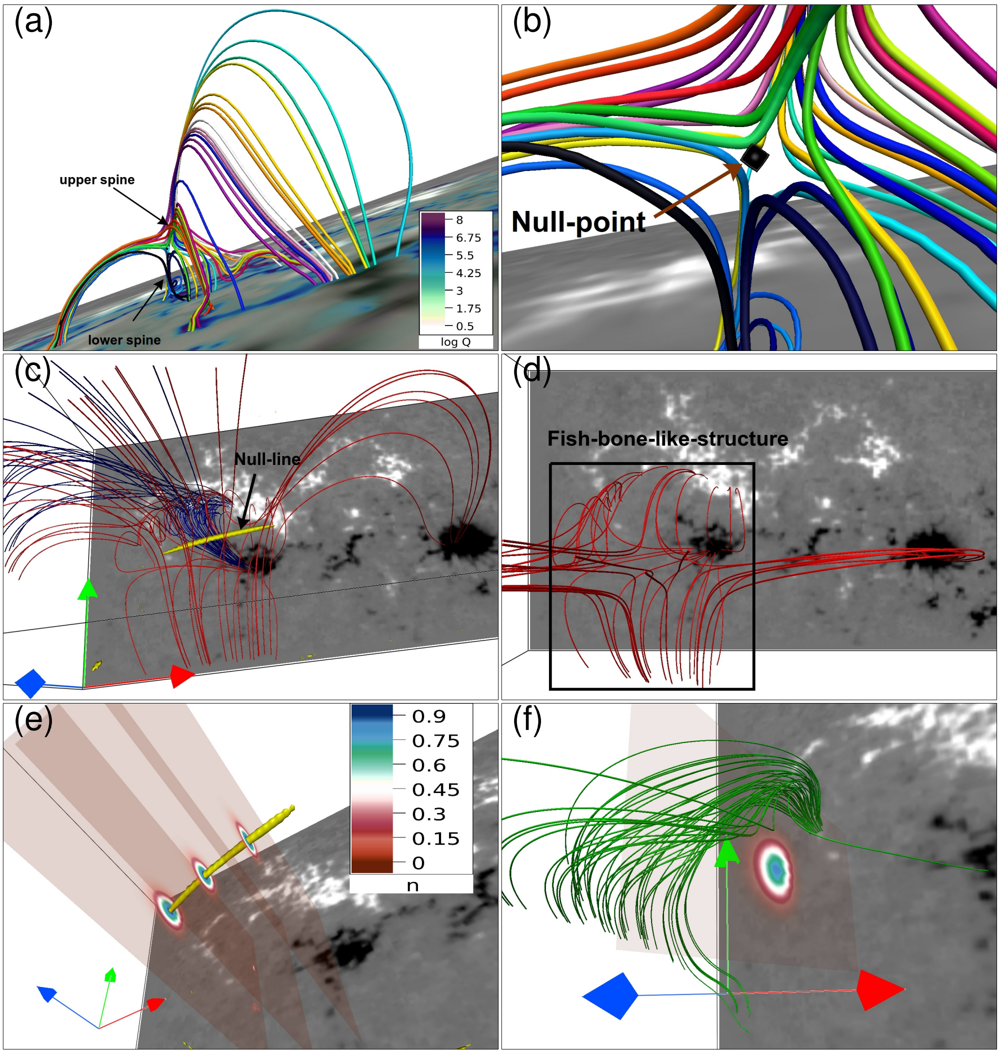

Figure 6.6: Panel (a) shows a 3D null spine-fan configuration in region R2 with the B_z as the bottom boundary overlaid with log Q between 5 and 10. Panel (b) is zoomed view of (a), highlighting the 3D null-point (in black)—an iso surface of $n = 0.6$ indicated by an arrow. Panel (c) shows the side view of magnetic field lines structure in region R3 along with the yellow surface representing the null-line corresponding to $n = 0.9$. Panel (d) shows the top-down view of red magnetic field lines of (c) forming fish-bone-like structure. In panel (e) we show the value of n on the three different vertical planes passing through the cross-sections of the null-line surface. Notably, the planes show circles in the cross-section at different locations which indicates that the yellow surface is a null line. Panel (f) depicts magnetic field lines morphology in region R4 along with the value of n on a vertical plane where the green circular contour corresponds to $n = 0.6$ suggesting the right part of magnetic field lines morphology may be a part of the null-line geometry (shown in panel (c)).

The Hall forcing has been incorporated (Bora et al., 2021) in the computational model EULAG-MHD (Smolarkiewicz & Charbonneau, 2013) to solve the dimensionless Hall MHD equations,

$$\frac{\partial \mathbf{v}}{\partial t} + (\mathbf{v}\cdot\nabla)\mathbf{v} = -\nabla p + (\nabla\times\mathbf{B})\times\mathbf{B} + \frac{1}{R_F^A}\nabla^2\mathbf{v}\ , \tag{6.2}$$

$$\frac{\partial \mathbf{B}}{\partial t} = \nabla\times(\mathbf{v}\times\mathbf{B}) - d_H\nabla\times((\nabla\times\mathbf{B})\times\mathbf{B})\ , \tag{6.3}$$

$$\nabla\cdot\mathbf{v} = 0\ , \tag{6.4}$$

$$\nabla\cdot\mathbf{B} = 0\ , \tag{6.5}$$

where $R_F^A = (v_A L_0/\nu)$, ν being the kinematic viscosity—is an effective fluid Reynolds number, having the plasma speed replaced by the Alfvén speed v_A. Hereafter R_F^A is denoted as fluid Reynolds number for convenience. The transformation of the dimensional quantities (expressed in cgs-units) into the corresponding non-dimensional quantities,

$$\mathbf{B}\longrightarrow\frac{\mathbf{B}}{B_0},\quad \mathbf{x}\longrightarrow\frac{\mathbf{x}}{L_0},\quad \mathbf{v}\longrightarrow\frac{\mathbf{v}}{v_A},\quad t\longrightarrow\frac{t}{\tau_A},\quad p\longrightarrow\frac{p}{\rho_0 {v_A}^2}\ , \tag{6.6}$$

assumes arbitrary B_0 and L_0 while the Alfvén speed $v_A \equiv B_0/\sqrt{4\pi\rho_0}$. Here ρ_0 is a constant mass density, and d_H is the Hall parameter. In the limit of $d_H = 0$, Equation 6.2 - Equation 6.5 reduce to the MHD equations (Prasad et al., 2018).

The governing equations (Equation 6.2 - Equation 6.5) are numerically integrated using the 3D HMHD solver described in Chapter 3.

The simulations are carried out by mapping the physical domain of $256 \times 128 \times 128$ pixels on the computational domain of $x \in \{-1, 1\}$, $y \in \{-0.5, 0.5\}$, $z \in \{-0.5, 0.5\}$ in a Cartesian coordinate system. The dimensionless spatial step sizes are $\Delta x = \Delta y = \Delta z \approx 0.0078$. The dimensionless time step is $\Delta t = 5 \times 10^{-4}$, set to resolve whistler speed—the fastest speed in incompressible Hall MHD. The rationale is briefly presented in Appendix A. The corresponding initial state is motionless ($\mathbf{v} = 0$) and the initial magnetic field is provided from the non-FFF extrapolation. The non-zero Lorentz force associated with the extrapolated field pushes the magnetofluid to initiate the dynamics. Since the maximal variation of magnetic flux through the photosphere is only 2.28% of its initial value during the flare (not shown), the B_z at the bottom boundary (at $z = 0$) is kept fixed throughout the simulation while all other boundaries are kept open. For velocity, all boundaries are set open. The mass density is set to $\rho_0 = 1$.

The fluid Reynolds number is set to 500, which is roughly two orders of magnitude smaller than its coronal value ≈ 25000 (calculated using kinematic viscosity $\nu = 4 \times 10^9$ m^{2}s^{-1} (Aschwanden, 2005) in solar corona). Without any loss in generality, the reduction in R_F^A can be envisaged to cause a reduction in computed Alfvén speed, $v_A|_{\text{computed}} \approx 0.02 \times v_A|_{\text{corona}}$ where the L for the computational and coronal length scales are set to 71 Mm and 100 Mm respectively. This diminished Alfvén speed reduces the requirement of computational resources and also relates it with the observation time. The results presented herein pertain to a run for $1200\Delta t$ which along with the normalizing $\tau_A \approx 3.55 \times 10^3$ s roughly corresponds to an observation time of ≈ 35 minutes. For the ease of reference in comparison with observations, we present the time in units of $0.005\tau_A$ (which is 17.75 s) in the discussions of the figures given in this chapter. Although the coronal plasma idealized to have reduced Reynolds number is inconsequential here, in a comparison of MHD and Hall MHD evolution, we believe the above rationale merits further contemplation. Undeniably such a coronal plasma is not a reality. Nevertheless, the reduced R_F^A does not affect the reconnection or its consequence, but slows down the dynamics between two such events and importantly—reduces the computational cost, making data-based simulations realizable even with reasonable computing resources. A recent work by Jiang et al. (2016) used homologous approach toward simulating a realistic and self-consistent flaring region.

In the present simulations, all parameters are identical for the MHD and the Hall MHD except for the d_H, respectively set to 0 and 0.004. The value 0.004 is motivated by recognizing ILES dissipation models intermittent magnetic reconnections at the $\mathcal{O}(\parallel \Delta\mathbf{x} \parallel)$ length scales, consistent with the thesis put forward in Introduction, we specify an appreciable Hall coefficient as $d_H = 0.5\Delta z/L \approx 0.004$, where $L = 1 \equiv$ smallest extent of the computational volume, having $\Delta y = \Delta z \approx 0.0078$ as the dissipation scales because of the ILES property of the model. Correspondingly, the value is also at the lower bound of the pixel or scale order approximation and, in particular, an order of magnitude smaller that its coronal value valid at the actual dissipation scale. An important practical benefit of this selection is the optimization of the computational cost while keeping magnetic field line dynamics tractable. Importantly, with dissipation and Hall scales being tied, an increased current density at the dissipation scale introduces additional slippage of field lines in Hall MHD over MHD (due to the Hall term) and, may be responsible for more effective and faster reconnections found in the Hall simulation reported below.

The simulated Hall MHD and MHD dynamics leading to the flare show unambiguous differences. Here we document these differences by comparing methodically simulated evolution of the magnetic structures and topologies in the AR NOAA 12734—namely, the flux rope, QSLs, and null points—identified in the extrapolated initial data in the regions R1-R4.

6.4.1 Region R1

The dynamics of region R1 are by far the most complex among the four selected regions. To facilitate future reference as well as to outline the organization of the discussion that follows, Table 6.1 provides a brief summary of our findings—in a spirit of theses to be proven by the simulation results.

Magnetic field lines structure	Hall MHD	MHD
QSL1	Fast reconnection followed by a significant rise of loops, eventually reconnecting higher in the corona.	Slow reconnection followed by a limited rise of loops.
QSL2	Fast reconnection causing the magnetic field lines to entirely disconnect from the polarity P2.	Due to slow reconnection magnetic field lines remain connected to P2.
Flux rope	Fast slipping reconnection of the flux-rope foot points, followed by the expansion and rise of the rope envelope.	Slow slipping reconnection and rise of the flux-rope envelope; the envelope does not reach the QSL1.

Table 6.1: Salient features of magnetic field lines dynamics in R1

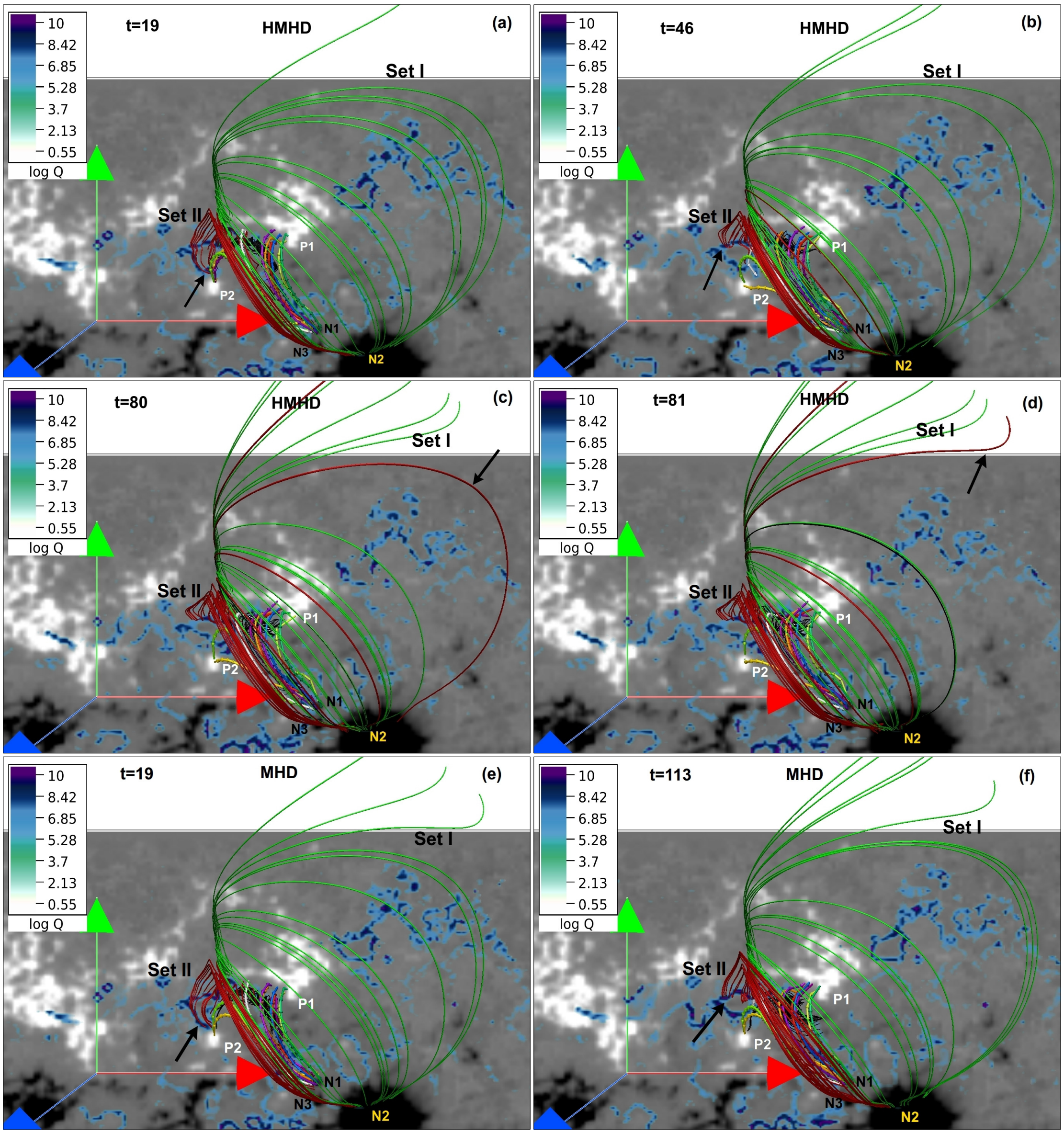

Figure 6.7: Snapshots of the global dynamics of magnetic field lines in region R1 during the Hall MHD and MHD simulations are shown in panels (a)-(d) and panels (e)-(f) respectively. Panels (a) and (b) show the departure of foot points of magnetic field lines Set II (maroon) away from polarity P2 between t=19 and 46 on the bottom boundary (marked by black arrow). Panel (c) depicts the rising magnetic field lines Set II (maroon) higher up in the solar corona at t=80 (marked by black arrow) and (d) shows subsequent connectivity change of rising magnetic field lines at t= 81, due to reconnection with the Set I (green) magnetic field lines. Panels (e) and (f) depict the departure of foot points of magnetic field lines Set II (maroon) away from P2 between t= 19 to 113 which is similar to the Hall MHD but delayed in time—indicating the slower dynamics in the MHD. Notably, significant rise of magnetic field lines Set II and consequent reconnection of it with magnetic field lines Set I higher up in the solar corona is absent in the MHD simulation.

The global dynamics of magnetic field lines in region R1 is illustrated in Figure 6.7; consult Figure 6.5 for the initial condition and terminology. The snapshots from the Hall MHD and MHD simulations are shown in panels (a)-(d) and (e)-(f), respectively. In panels (a) and (b), corresponding to $t = 19$ and $t = 46$, the foot points of magnetic field lines Set II (near P2, marked maroon) exhibit slipping reconnection along high values of the squashing factor Q indicated by black arrows. Subsequently, between $t = 80$ and 81 in panels (c) and (d), the magnetic field lines Set II rise in the corona and reconnect with magnetic field lines Set I to change connectivity. The MHD counterpart of the slipping reconnection in panels (e) and (f), corresponds to magnetic field lines Set II between t=19 and t=113. It lags behind the Hall MHD displays, thus implying slower dynamics. Furthermore, the magnetic field lines Set II, unlike for the Hall MHD, do not reach up to the magnetic field lines Set I constituting QSL1 and hence do not reconnect. The decay index is calculated for each time instant for both the simulations and is found to be less than 1.5 above the flux rope, indicating an absence of the torus instability (?). For more detail, Figure 6.8 and Figure 6.9 illustrate evolution of QSL2 and flux rope separately.

Figure 6.8 panels (a)-(b) and (c)-(d) show, respectively, the instants from the Hall MHD and MHD simulations of QSL2 between P1, P2 and N1. The Hall MHD instants show magnetic field lines that were anchored between P2 and N1 at $t = 10$ have moved to P1 around t=102, marked by black arrows in both panels. The magnetic field lines anchored at P2 moved to P1 along the high Q values—signifying the slipping reconnection. The MHD instants in panels (c)-(d) show the connectivity changes of the violet and white colored magnetic field lines. The white field line was initially connecting P1 and N1, whereas the violet field line was connecting P2 and N1. As a result of reconnection along QSL, the white field line changed its connectivity from P1 to P2 and violet field line changes the connectivity from P2 to P1 (marked by black arrows). Notably, in contrast to the Hall MHD evolution, all magnetic field lines initially anchored in P2 do not change their connectivity from P2 to P1 during the MHD evolution, indicating the slower dynamics. The flux rope has been introduced in panels (c) and (d) of Figure 6.5, respectively, below the QSL2 and in enlargement. Its Hall MHD and MHD evolutions along with the twists on three different vertical cross sections are shown in panels (a)-(f) and (g)-(i) of Figure 6.9, respectively. Magnetic field lines

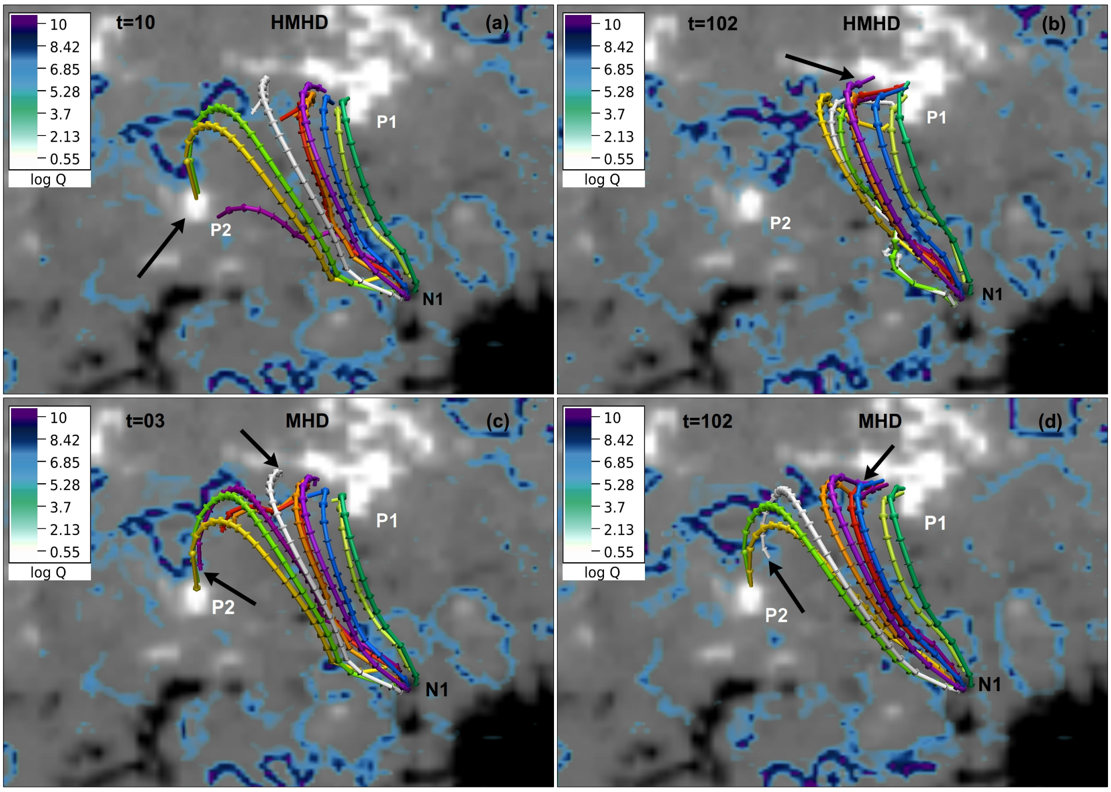

Figure 6.8: Snapshots of the Hall MHD and MHD evolution of QSL2 (Figure 6.5 (c)) are shown in panels (a)-(b) and panels (c)-(d) respectively. Panels (a)-(b) show magnetic field linesanchored in the positive polarity P2 at t=10 have moved to the polarity P1 by t=102 and changed their connectivity (marked by black arrow) due to reconnection along QSL during the Hall MHD. Panels (c)-(d) show the connectivity changes of the violet and white color magnetic field lines during the MHD evolution. The white field line was initially connecting the polarities P1 and N1 whereas the violet field line was connecting P2 and N1. As a result of reconnection along QSL the white field line changes its connectivity from P1 to P2 and violet field line changes the connectivity from P2 to P1 (marked by black arrows). Notably, unlike the Hall MHD simulation not all magnetic field lines move to P1 from P2 due to reconnection along QSL during the MHD which indicates the slower dynamics.

constituting the rope, rise substantially higher during the Hall MHD evolution as a result of slipping reconnection along the high Q in panels (c)-(f). In panel (c) at $t = 32$, the foot points of the rope that are anchored on right side (marked by black arrow) change their connectivity from one high Q regime to another in panel (d) at t=33; i.e., the foot points on the right have moved to the left side (marked by black arrow). Afterwards, the magnetic field lines rise because of the continuous slipping reconnection, as evidenced in panels (e) to (f). Comparing panels (a) with (g) at $t = 10$ and (c) with (h) at t=32, we note that the twist value T_w is higher in the Hall MHD simulation. Panels (h)-(i) highlight the displaced foot

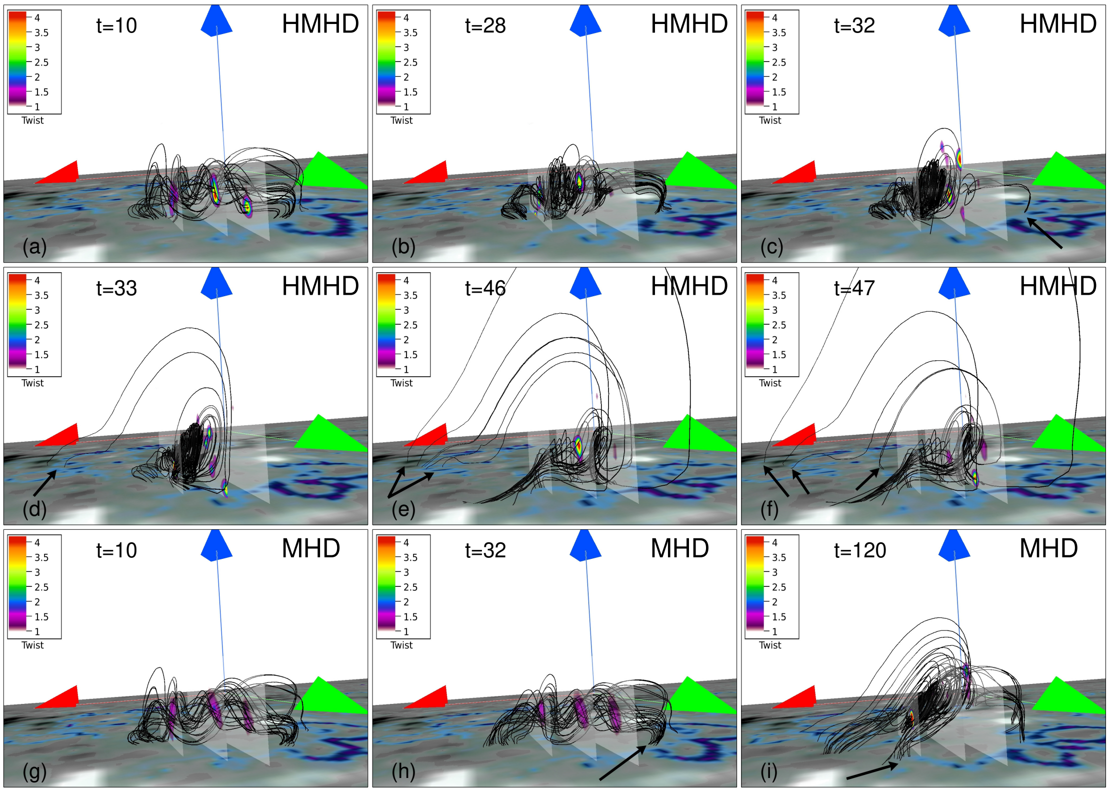

Figure 6.9: Time sequence showing the Hall MHD (panels (a)-(f)) and MHD (panels (g)-(i)) evolution of the flux rope (shown in Figure 6.5(c)) along with the twist T_w. Panel (a) shows the twist on the middle and the right plane on flux rope is higher than initial values (c.f. Figure 6.5(d)) and reduced with time in panel (b). Panels (c)-(d) depict the connectivity change of the foot point of rope from right to left (indicated by black arrow) due to reconnection along QSL. Panels (e)-(f) show the connectivity change of magnetic field lines on left hand side (indicated by black arrow). Panels (g)-(i) depict the dynamic rise of the flux rope between t=10 and t=120 during the MHD simulation. Notably, the foot points of the rope on the right side (marked by black arrow) at t=32 in (h) have moved towards left by t=120 in (i) as a result of reconnection along QSL.

points of flux rope due to slipping reconnection at t=32 and t=120 (cf. black arrow). The rope is preserved throughout the Hall MHD and MHD simulations. The rise and expansion of the flux-rope envelope owing to slipping reconnection is remarkable in the Hall MHD simulation. Dudík et al. (2014) have already shown such a flux-rope reconnection along QSL in a J-shaped current region, with slipping reconnection causing the flux rope to form a sigmoid (S-shaped hot channel observed in EUV images of SDO/AIA) followed by its rise and expansion. Further insight is gained by overlaying the flux rope evolution shown in Figure 6.9 with direct volume rendering of $|\mathbf{J}|/|\mathbf{B}|$ (Figure 6.10 and Figure 6.11) as a measure of magnetic field gradient for the Hall MHD and MHD simulations. In the Hall

MHD case, appearance of large values of $|\mathbf{J}|/|\mathbf{B}| > 475$ inside the rope (panels (a) to (c)) and foot points on left of the rope (panels (d) to (e)) are apparent. The development of the large $|\mathbf{J}|/|\mathbf{B}|$ is indicative of reconnection within the rope. Contrarily, MHD simulation lacks such high values of $|\mathbf{J}|/|\mathbf{B}|$ in the same time span (panels (a)-(b)) and the field lines show no slippage—agreeing with the proposal that large currents magnify the Hall term, resulting into more effective slippage of field lines.

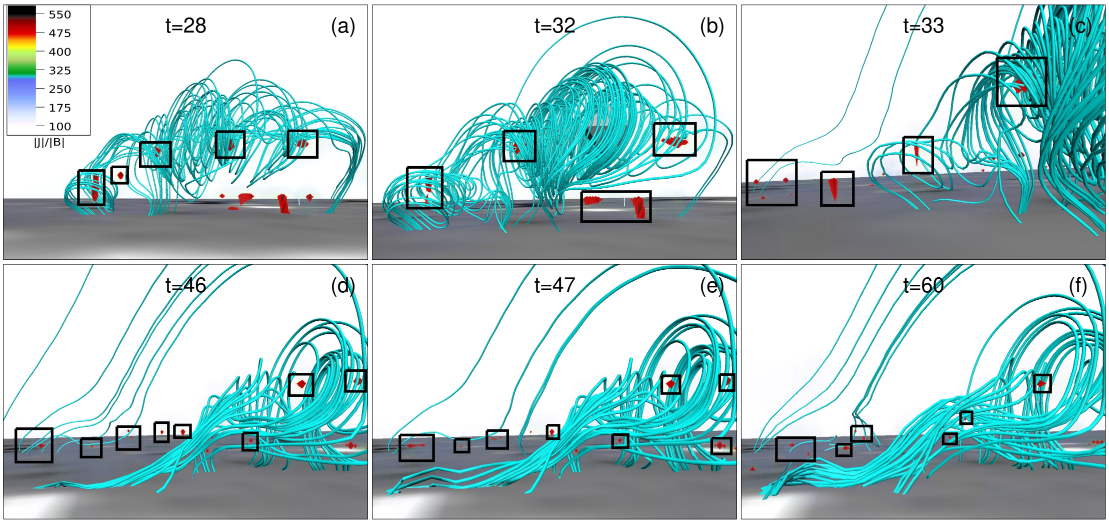

Figure 6.10: Temporal variation of the direct volume rendering of ($|\mathbf{J}|/|\mathbf{B}|$) along with the flux rope is shown during the Hall MHD simulation. Noticeably, the high magnetic field gradient regions with ($|\mathbf{J}|/|\mathbf{B}|$) ≥ 475 develop within (panels (a) to (c)) and on the left side of the flux rope (panels (d) to (f)). The values ($|\mathbf{J}|/|\mathbf{B}|$) ≥ 475 in each panel are enclosed within the black rectangular boxes.

6.4.2 Region R2

To compare the simulated magnetic field lines dynamics in region R2 with the observed tip of the W-shaped flare ribbon B2 (Figure 6.4 (a)) during the Hall MHD and MHD evolution, we present the instants from both simulations at t=70 in panels (a) and (b) of Figure 6.12 respectively. Importantly, the lower spine remains anchored to the bottom boundary during the Hall MHD simulation. Further, Figure 6.13 shows the evolution of the lower spine along with the $|\mathbf{J}|/|\mathbf{B}|$ on the bottom boundary for the Hall MHD (panels (a) to (d)) and MHD (panels (e) to (h)) cases. In the Hall MHD case, noteworthy is the slipping motion of lower spine (marked by the black arrows) tracing the $|\mathbf{J}|/|\mathbf{B}| > 350$ regions on the bottom

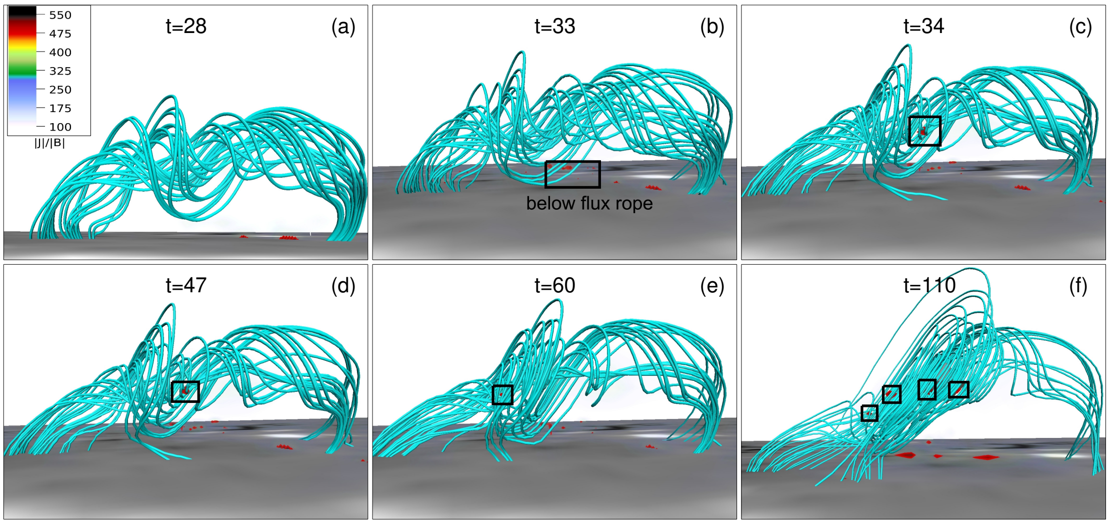

Figure 6.11: Temporal variation of the direct volume rendering of (|**J**|/|**B**|) along with the flux rope is shown during the MHD simulation. Panels (a) and (b) shows the absence of high values of (|**J**|/|**B**|) within the rope at $t = 28$ and $t = 32$ but in later panels (c) to (f) (|**J**|/|**B**|) $\geq$ 475 appears (enclosed by the black rectangular boxes). Notably, as compared to the Hall MHD case (Figure 6.10), the development of (|**J**|/|**B**|) is not significant in the region R1 during the MHD.

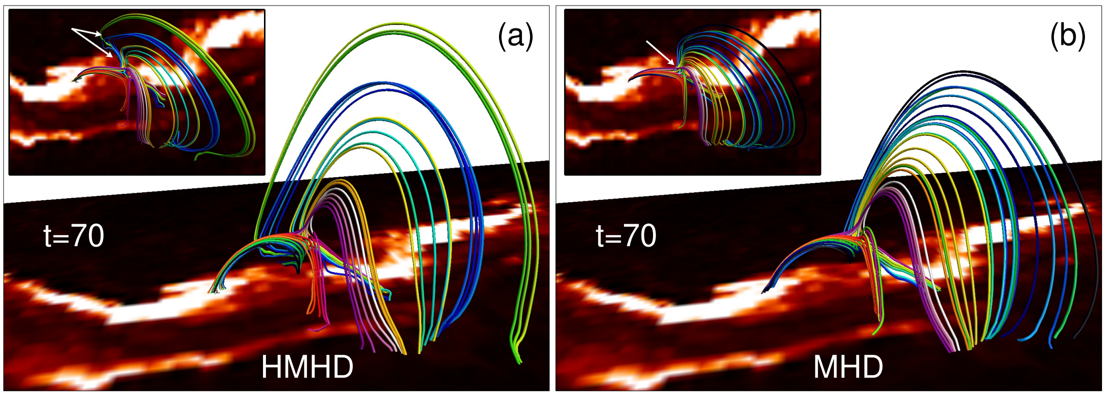

Figure 6.12: Panels (a) and (b) show the comparison of magnetic field lines topology in region R2 at t=70 with the flare ribbons observed in the SDO/AIA 304 Å channel (side views) during the Hall MHD and MHD simulations respectively. The inset images on the top left corner in each panel show the top view of the same magnetic field lines topology. Notably, the spine is anchored in the Hall MHD while it is not connected to the bottom boundary in the MHD at t=70 (marked by white arrow in inset images).

boundary (panels (a) to (b)). Whereas, in the MHD such high values of |**J**|/|**B**| are absent on the bottom boundary—suggesting the slippage of the field lines on the bottom boundary to be less effective in contrast to the Hall MHD. The finding is in agreement with the idea of enhanced slippage of field lines due to high current densities as conceptualized in the introduction. The anchored lower spine provides a path for the plasma to flow downward to the brightening segment B2. In the actual corona, such flows result in flare brightening (Benz, 2008). In contrast, the lower spine gets completely disconnected from the bottom boundary (Figure 6.12 (b)) in the MHD simulation, hence failing to explain the tip of the W-shaped flare ribbon in B2. The anchored lower spine in the Hall MHD simulation is caused by a complex series of magnetic field lines reconnections at the 3D null and along the QSLs in R2.

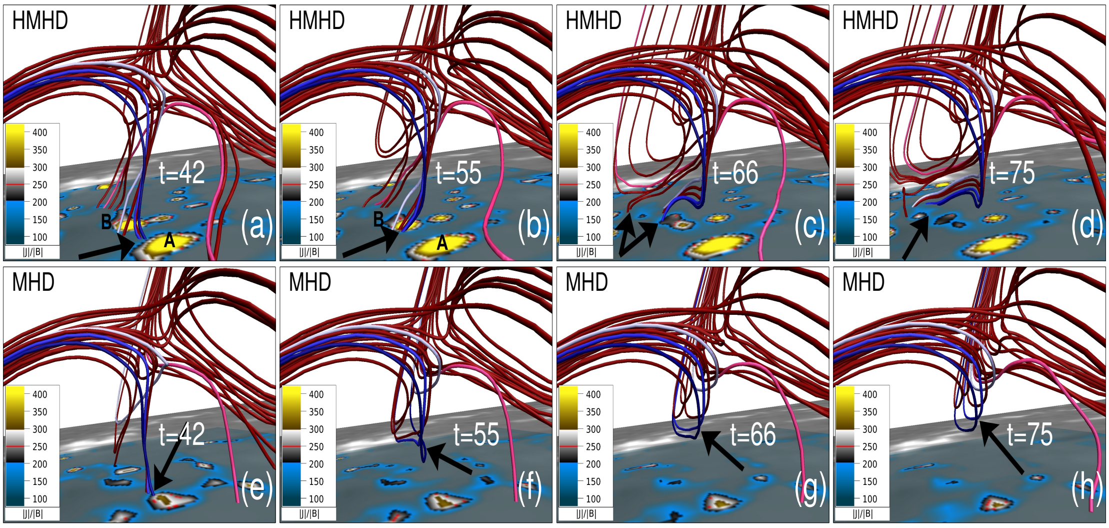

Figure 6.13: Panels (a) to (d) depict the slipping motion of the lower spine field lines (also shown in the Figure 6.6) overlaid with the $|\mathbf{J}|/|\mathbf{B}|$ on the bottom boundary during the Hall MHD evolution. The motion is marked by the black arrows in all the panels indicating the successive change in the location of field lines on the bottom boundary. A and B (in panels (a) and (b)) are the two regions with $|\mathbf{J}|/|\mathbf{B}| > 350$ on the bottom boundary (just below the lower spine). Notably, the field lines follow the high values of $|\mathbf{J}|/|\mathbf{B}|$ on the bottom boundary and remain anchored. Panels (e) to (h) show the evolution of the same lower spine field lines during the MHD simulation. The large values of $|\mathbf{J}|/|\mathbf{B}|$ do not appear below the lower spine (on the bottom boundary) and it does not remain anchored from $t \approx 55$ onward (panels (f) to (h)).

6.4.3 Region R3

Hall MHD and MHD simulations of magnetic field lines dynamics around the null-line are shown in Figure 6.14 and Figure 6.15 respectively. Figure 6.14 shows the blue magnetic field lines prior and after the reconnections (indicated by black arrows) between t=4 to 5 (panels (a)-(b)), t=52 to 53 (panels (c)-(d)), and t=102 to 103 (panels (e)-(f)) during the Hall MHD simulation. Figure 6.15 shows the same blue magnetic field lines prior and after the reconnections (indicated by black arrows) between t=12 to 13 (panels (a)-(b)), t=59 to 60 (panels (c)-(d)), and t=114 to 115 (panels (e)-(f)) during the MHD simulation. Comparison of the panels (a)-(f) of Figure 6.14 with the same panels of Figure 6.15 reveals earlier reconnections of the blue magnetic field lines in the Hall MHD simulation. In both figures, green velocity vectors on the right represent the local plasma flow.

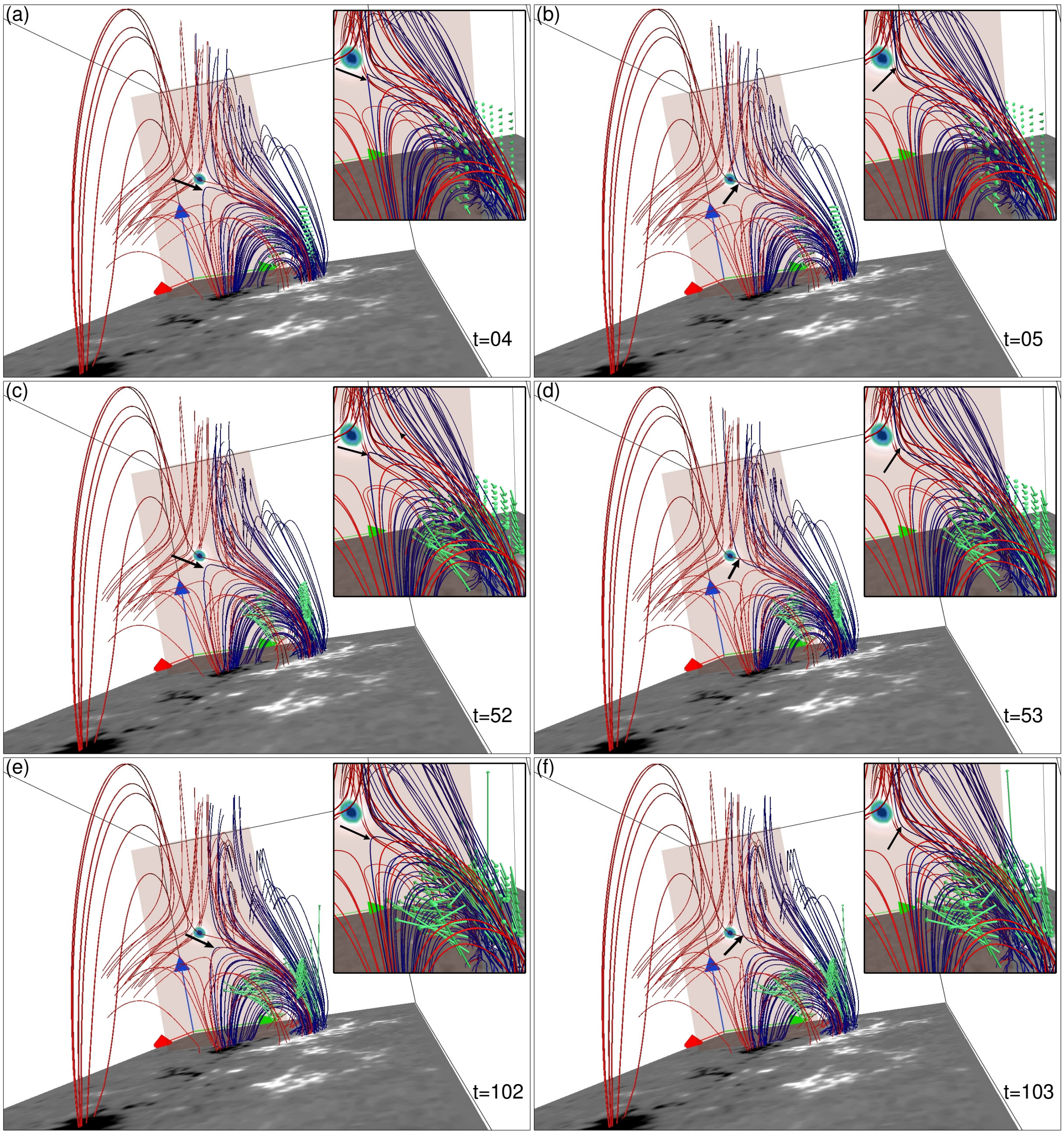

Figure 6.14: Time sequence showing the blue field line prior and after reconnection (indicated by back arrow) in region R3 during the Hall MHD simulation. Evolution of the flow vectors is depicted by green arrows (on the right side)—mimicking the direction of the plasma flow. The plane along the cross section of magnetic field lines morphology in R3, showing the blue circular contours represent the value of n (also shown in Figure 6.6(d)).

They get aligned downward along the foot points of the fan magnetic field

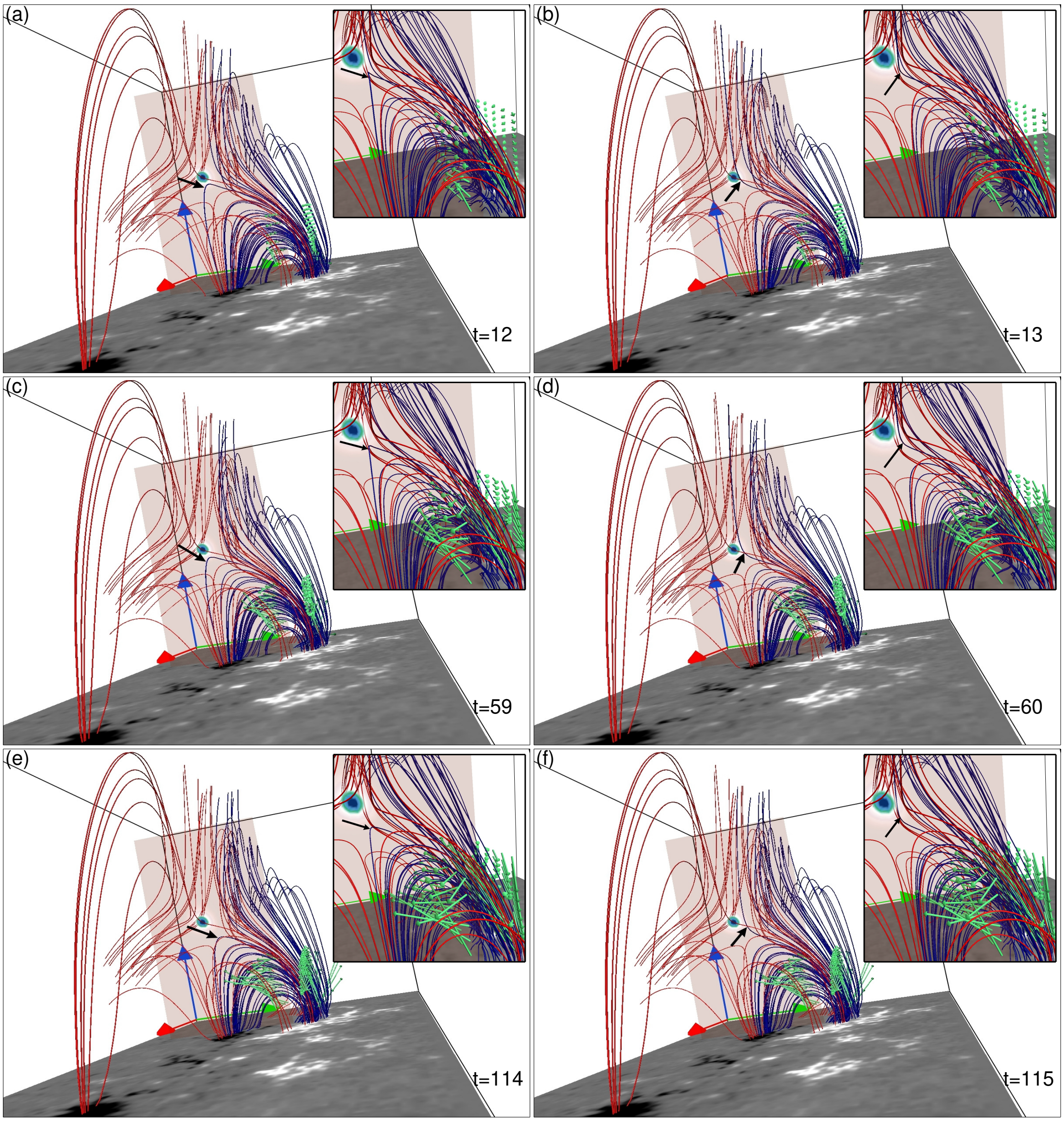

Figure 6.15: Time sequence showing the blue field line prior and after reconnection (indicated by back arrow) in region R3 during the MHD simulation. Evolution of the flow vectors is depicted by green arrows (on the right side)—mimicking the direction of the plasma flow. The plane along the cross section of magnetic field lines morphology in R3, showing the blue circular contours represent the value of n (also shown in Figure 6.6(d)). Notably, reconnection of the blue magnetic field lines is slightly delayed in comparison to its Hall MHD counterpart.

lines, as reconnection progresses. Consequently, the plasma flows downward and impacts the denser and cooler chromosphere to give rise to the brightening in B3. The velocity vectors pointing upward represent a flow toward the null-line. The plasma flow pattern in R3 is the same in the Hall MHD and in the MHD simulation. The vertical yz plane passing through the cross section of the null-line surface (also shown in Figure 6.6 (d)) in all the panels of Figure 6.14 and Figure 6.15 shows the variation of n with time. It is evident that the null is not destroyed throughout the Hall MHD and MHD evolution. Structural changes in the field lines caused by reconnection is near-identical for both the simulations, indicating inefficacy of the Hall term. This inefficacy is justifiable as $|\mathbf{J}|/|\mathbf{B}|$ remains small ≈ 10 (not shown) in both Hall MHD and MHD evolution.

6.4.4 Region R4

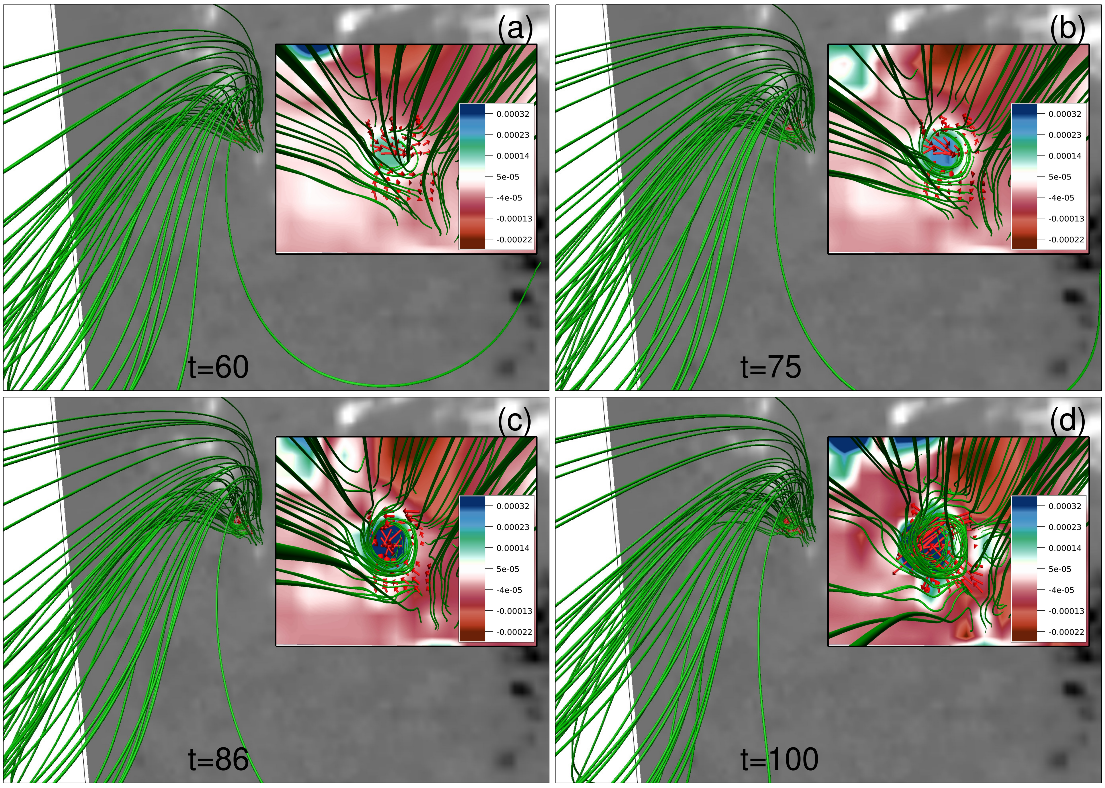

Figure 6.16: Panels (a)-(d) show the global dynamics of magnetic field lines in region R4 during the Hall MHD simulation. Inset images in each panel (on right) depict the time sequence of the zoomed top-down view of the rotational motion of magnetic field lines. The background shows the variation of the z-component of flow $\in$ [-0.00022,0.00032] in all inset images. The red vectors represent the plasma flow and change its direction in an anticlockwise manner in panels (a)-(d). The rotational motion of magnetic field lines coincides with the circular part of the flow.

The development of the circular motion of magnetic field lines in region R4 during the Hall MHD simulation is depicted in Figure 6.16. It shows the global dynamics of magnetic field lines in R4 and the inset images show the zoomed view of magnetic field lines in R4 to highlight the circular motion of magnetic field lines. The bottom boundary is B_z in the main figure while the inset images have the z

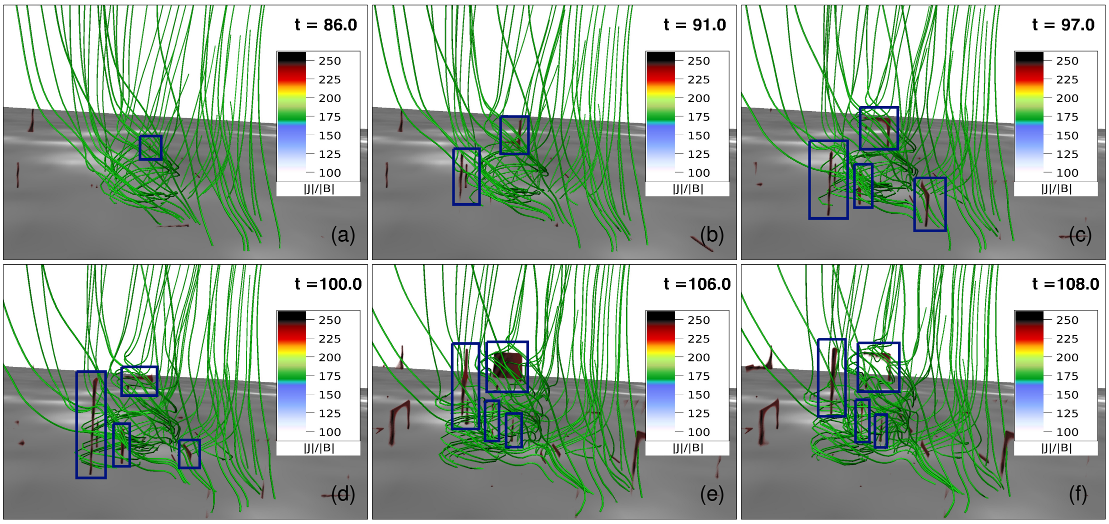

Figure 6.17: Panels (a) to (f) show the side view of the rotating magnetic field lines structure in the region R4 overlaid with $|\mathbf{J}|/|\mathbf{B}|$. The figure depicts the temporal development of strong magnetic field gradient regions of $|\mathbf{J}|/|\mathbf{B}| > 225$ (enclosed in the blue rectangular boxes) within the rotating magnetic structure.

component of the plasma flow at the bottom boundary (on xy plane). The red vectors represent the plasma flow direction as well as magnitude in all the panels of Figure 6.16 where the anticlockwise pattern of the plasma flow is evident. The global dynamics highlight reconnection of the loop anchored between positive and negative polarities at t=60 in Figure 6.16 as it gets disconnected from the bottom boundary in panels (c)-(d) of Figure 6.16. In simulation an anticlockwise motion of foot points in the same direction as the plasma flow is found, indicating field lines to be frozen in the fluid. The trapped plasma may cause the rotating structure B4 in the observations (c.f. ?? (a)). However, no such motion is present during the MHD evolution of the same magnetic field lines (not shown). An interesting feature noted in the simulation is the clockwise slippage of field lines after the initial anticlockwise rotation. Further analysis of R4 using the direct volume rendering of $|\mathbf{J}|/|\mathbf{B}|$ is presented in Figure 6.17. The figure shows $|\mathbf{J}|/|\mathbf{B}|$ attains high values ≥ 225 (enclosed by the blue rectangles) within the rotating field lines from t≈86 onward. This suggests the slippage of field lines is, once again, related to the high magnetic field gradients.

For completeness, we present the snapshots of an overall magnetic field lines morphology including the magnetic structures and topology of regions R1, R2, R3, and R4 together, overlaid with 304 Å and 171 Å from the Hall MHD and

MHD simulations. Figure 6.18 (a) shows an instant (at t=75) from the Hall MHD simulation where the topologies and magnetic structures in R1, R2, R3, and R4, plus the additionally drawn locust color magnetic field lines between R2 and R3 are shown collectively. It shows an excellent match of the magnetic field lines in R2 with the observed tip of W-shaped flare ribbon at B2, which is pointed out by the pink arrow in panel (a). Foot points of the spine-fan geometry around the 3D null orient themselves in the same fashion as the observed tip of the W-shaped flare ribbon at B2 as seen in 304 Å channel of SDO/AIA. The rising loops indicated by the white arrow correspond to the same evolution as shown in Figure 6.7. An overall magnetic field lines morphology mentioned in Figure 6.16 (a) is given at the same time (t=75) during the MHD simulation overlaid with 304 Å image in Figure 6.16 (b). Importantly, unlike the Hall MHD simulation, the MHD simulation does not account for the anchored lower spine and fan magnetic field lines of the 3D null at the center of the B2. Also, the significant rise of overlying maroon magnetic field lines and the circular motion of the material in B4 is captured in the Hall MHD simulation only. In panel (c) magnetic field lines overlaid with 171 Å image shows the magnetic field lines (higher up in the solar atmosphere) have resemblance with the post-flare loops during the Hall MHD. Overall, the Hall MHD evolution seems to be in better agreement with the observations in comparison to the MHD evolution.

6.5 Summary

In this Chapter the data-based Hall MHD and MHD simulations are compared for the flaring Active Region NOAA 12734 as a test bed. Importance of the Hall MHD stems from the realization that the Hall term in the induction equation cannot be neglected in presence of the magnetic reconnection—the underlying cause of solar flares. The selected event is the C1.3 class flare on March 08, 2019 around 03:19 UT for the aforementioned comparison. Although the event is analyzed and reported in the literature, it is further explored using the multi-wavelength observations from SDO/AIA. The identified important features are: an elongated extreme ultraviolet (EUV) counterpart of the eruption on the western side of the

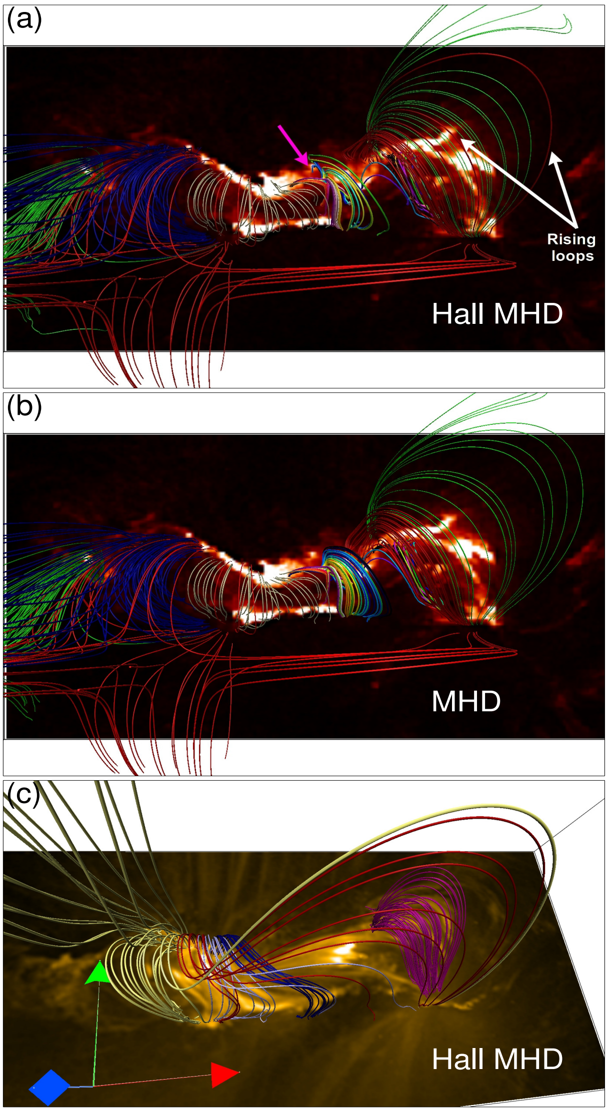

Figure 6.18: Top-down view of an overall magnetic field lines morphology overlaid on the SDO/AIA 304 Å (panels (a) and (b)) and 171 Å images (panel (c)). Anchored magnetic field lines foot points in central part match well with the observed tip of the W-shaped flare ribbon (marked by pink arrow in panel (a)) in the Hall MHD while magnetic field lines foot points are completely disconnected from the bottom boundary in the MHD (panel (b)). Loops rising higher up in the corona is remarkable in the Hall MHD (indicated by white arrow in panel (a)).

AR, a W-shaped flare ribbon and circular motion of cool chromospheric material on the eastern part. The magnetic field line dynamics near these features are utilized to compare the simulations. Notably, the simulations idealize the corona to have an Alfvèn speed which is two orders of magnitude smaller than its typical value. Congruent to the general understanding, the Hall parameter is selected to tie the Hall dynamics to the dissipation scale $\mathcal{O}(\Delta \mathbf{x})$ in the spirit of the ILES carried out in the Chapter. The magnetic reconnection here is associated with the slippage of magnetic field lines from the plasma parcels, effective at the dissipation scale due to local enhancement of magnetic field gradient. The same enhancement also amplifies the Hall contribution, presumably enhancing the slippage and thereby making the reconnection faster and more effective than the MHD as put forward in the prop-hall-rec.

The coronal magnetic field is constructed by extrapolating the photospheric vector magnetic field obtained from the SDO/HMI observations employing the non-FFF technique (Hu et al., 2010). The concentrated distribution of the Lorentz force on the bottom boundary and its decrease with the height justify the use of non-FFF extrapolation for the solar corona. The initial non-zero Lorentz force is also crucial in generating self-consistent flows that initiate the dynamics and cause the magnetic reconnections. Analyses of the extrapolated magnetic field reveal several magnetic structures and topologies of interest: a flux rope on the western part at flaring location, a 3D null point along with the fan-spine configuration at the centre, a "Fish-bone-like structure" surrounding the null-line on the eastern part of the AR. All of these structures are found to be co-spatial with the observed flare ribbon brightening.

The Hall MHD simulation shows faster slipping reconnection of the flux rope foot points and overlying magnetic field lines (constituting QSLs above the flux rope) at the flaring location. Consequently, the overlying magnetic field lines rise, eventually reaching higher up in the corona and reconnecting to provide a path for plasma to eject out. The finding is in agreement with the observed elongated EUV counterpart of the eruption on western part of the AR. Contrarily, such significant rise of the flux rope and overlying field lines to subsequently reconnect higher up in the corona is absent in the MHD simulation—signifying the reconnection to be slower compared to the Hall MHD. Intriguingly, rise and expansion of the flux rope and overlying field lines owing to slipping reconnection on QSLs has also been modelled and observed in an earlier work by Dudík et al. (2014). These are typical features of the "standard solar flare model in 3D", which allows for a consistent explanation of events which are not causally connected (Dudík et al., 2014). It also advocates that null-points and true separatrices are not required for the eruptive flares to occur—concurring the results of this work. Hall MHD evolution of the fan-spine configuration surrounding the 3D null point is in better agreement with the tip of W-shaped flare ribbon at the centre of the AR. The lower spine and fan magnetic field lines remain anchored to the bottom boundary throughout the evolution which can account for the plasma flowing downward after the reconnection and cause the brightening. Whereas in the MHD, the lower spine gets disconnected and cannot account for the brightening. The reconnection dynamics around the null-line and the corresponding plasma flow direction is same in the Hall MHD as well as the MHD simulation and agrees with the observed brightening. Nevertheless, reconnection is earlier in the Hall MHD. Hall MHD evolution captures an anti-clockwise circular motion of magnetic field lines in the left part of the AR which is co-spatial with the location of the rotating chromospheric material in eastern side of the AR. No such motion was found in the MHD simulation. Importantly, the simulations explicitly associate generation of large magnetic field gradients to Hall MHD compared to MHD, resulting in faster and more efficient field line slippage because of the enhanced Hall term.

Overall, the results documented in the Chapter show the Hall MHD explains the flare brightening better than the MHD, prioritizing the requirement to include Hall MHD in future state-of-the-art data-based numerical simulations.

Chapter 7

Summary and Future Prospects

7.1 Summary

In this thesis, the role of Hall effect in magnetic reconnection has been investigated by employing numerical simulations which are initiated with analytical and observed solar magnetic fields. The key problems of fast and impulsive reconnection have been addressed. For the works presented in this thesis, a comparative study of reconnections and the evolution of magnetic structures in the presence and absence of Hall effect is carried out. For the purpose, we have developed a 3D HMHD solver by incorporating Hall term in the well established computational model— EULAG MHD. The development of a 3D HMHD solver benefits from the Implicit Large Eddy Simulation (ILES) nature of EULAG MHD which exhibits numerical diffusion determined by the resolution (Chapter 3). The requirement of very large spatial resolution is overcome by tying the Hall effect with the dissipation scale so that an increased current density at the dissipation scale enhances the Hall effect. Subsequently, benchmarking (Chapter 4) is done with an initially unidirectional sinusoidal magnetic field which has an initial non-zero Lorentz force. This choice of initial condition allows us to validate the developed 3D HMHD solver without repeating the traditional simulations using the Harris current-sheet equilibrium or the GEM challenge. Hall MHD and MHD numerical simulations are carried out in the presence and absence of the Hall term. MHD simulation results show a symmetric magnetic field evolution in the computation domain. Magnetic reconnections generate magnetic flux tubes made by disjoint magnetic field lines. Whereas, during the Hall MHD simulation, the evolution becomes asymmetric and 3D due to the generation of an out-of-reconnection plane magnetic field component. The magnetic energy evolution is identical. The time derivative of growth rate of current density shows abrupt changes during the Hall MHD—implying impulsiveness. These results are in concurrence with the earlier Hall MHD simulations in the literature and validate the developed 3D HMHD solver. Along with the flux tube, magnetic reconnections also generate magnetic flux rope—a twisted set of field lines in the Hall MHD. When viewed favorably, the rope and the tube appear as magnetic islands. Further evolution leads to the breakage of primary islands into secondary islands and later their merging is observed. Overall, the results agree with the existing scenarios of Hall-assisted reconnection based on physical arguments and other recent simulations including those on the GEM challenge. An important finding is the formation of complex 3D magnetic structures, which cannot be apprehended from 2D models or calculations although their projections agree with the latter. Alongside, we have numerically explored the Whistler mode propagation vis-a-vis its analytical model and found the two to be matching reasonably well in the Hall MHD simulations.

Understanding the evolution of a magnetic flux rope is instructive to understand the coronal mass ejections owing to eruptive flares, prominence or filament eruptions on the Sun. Therefore, the developed 3D HMHD solver has been further employed to simulate the Hall effect on the generation and evolution of magnetic flux rope for two cases depending upon the initial conditions (Chapter 5). The simulations in the first and second cases are initiated with an axisymmetric and the three-dimensional bipolar sheared arcade like magnetic fields, respectively. Magnetic flux rope in the first case is levitating and unanchored one, whereas in other case it is anchored to the bottom boundary. A comparative investigation of the Hall MHD and MHD simulations reveal that the primary reconnections through which the flux rope is generated are identical in both the simulations for both cases. However, further evolution of flux ropes is influenced by the Hall forcing as the reconnections proceed. The first case, once again shows a reasonable maintenance of symmetry in the standard MHD simulation, whereas a clear symmetry-breaking—leading to generation of three dimensional magnetic structures—appears to be a signature of the Hall effect. In Hall MHD the flux rope evolves through a series of complex geometries while rotating along its axis. When viewed favorably, it appears to contain structures reminiscent of the "number eight (8)", which is the result of internal reconnection within rope. Notably, the magnetic energies, in the presence and absence of the Hall forcing, vary almost identically for both the cases—consistent with the theoretical understanding that the Hall term directly does not change the magnetic energy dissipation rate.

In the second case, the flux rope is found to generate in consequence of repetitive reconnection at three-dimensional magnetic nulls—detected using trilinear method of null detection techniques, in both Hall MHD as well as MHD simulations while preserving the topological degree. Twisting of magnetic field lines in the vicinity of three-dimensional nulls—an unique feature found during the Hall MHD evolution of rope which further leads to the formation of large scale flux rope. This result suggests that the Hall effect modify dynamics of magnetic structures around small-scale (reconnection site) which further generates large scale structure, hence relating the small scale and large scale dynamics. Also, the faster formation of post-reconnection arcades in the Hall MHD signifies a faster dynamics.

After gaining the experience with of Hall effect 3D magnetic reconnection, the numerical model has been further employed to simulate the Hall effect in magnetic reconnection for a flaring active region (AR) on the Sun as a testbed (Chapter 6). This work compares the data-based Hall MHD and MHD simulations using the flaring NOAA AR 12734 as a test bed. For the purpose, the event under consideration, is the C1.3 class flare on 2019 March 8 around 03:19 UT. Although the event is analyzed and reported in the literature, it is further explored using the multi wavelength observations from SDO/AIA. The important features outline in the observation include an elongated EUV counterpart of the eruption on the western side of the AR, a W-shaped flare ribbon and the circular motion of cool chromospheric material on the eastern part. The magnetic field line dynamics related to these features are compared in the simulations. Notably, the simulations idealize the corona to have an Alfvèn speed of two orders of magnitude smaller than its typical value. Conforming with the general understanding, the Hall parameter is selected to tie the Hall dynamics to the dissipation scale $\mathcal{O}(\Delta \mathbf{x})$ in spirit of the implicit large eddy simulations (ILES). The magnetic reconnection here is associated with the slippage of magnetic field lines from the plasma parcels, effective at the dissipation scale due to local enhancement of magnetic field gradients. The same enhancement also amplifies the Hall contribution and enhances the slippage, thereby making the reconnection faster and more effective in Hall MHD in comparison to the MHD. The coronal magnetic field is constructed by extrapolating the photospheric vector magnetic field obtained from the SDO/HMI observations employing the non-FFF technique. The concentrated distribution of the Lorentz force on the bottom boundary and its decrease with the height justify the use of non-FFF extrapolation for the solar corona. The initial nonzero Lorentz force is also crucial in generating self-consistent flows that initiate the dynamics and cause the magnetic reconnections. Analyses of the extrapolated magnetic field reveals several magnetic structures and topologies of interest: a flux rope on the western part at the flaring location, a 3D null point along with the fan-spine configuration at the center, and a "fish-bone-like structure" surrounding the null line on the eastern part of the AR. All of these structures are found to be cospatial with the observed flare ribbon brightening. The Hall MHD simulation shows faster slipping reconnection of the flux-rope footpoints and overlying magnetic field lines (constituting quasi separatrix layers (QSLs) above the flux rope) at the flaring location. Consequently, the overlying magnetic field lines rise, eventually reaching higher up in the corona and reconnecting to provide a path for plasma to eject out. This finding agrees with the observed elongated EUV counterpart of the eruption on the western part of the AR. Contrarily, such a significant rise of the flux rope and overlying field lines to subsequently reconnect higher up in the corona is absent in the MHD simulation—signifying that the reconnection is slower compared to the Hall MHD. Interestingly, rise and expansion of the flux rope and overlying field lines due to slipping reconnection on QSLs have also been modeled and observed in literature. Previous work in literature, also advocates that null points and true separatrices are not required for the eruptive flares to occur—congruent with the results of our work. Hall MHD evolution of the fan-spine configuration surrounding the 3D null point is in better agreement with the tip of the W-shaped flare ribbon at the center of the AR. The lower spine and fan magnetic field lines remain anchored to the bottom boundary throughout the evolution, which can account for the plasma flowing downward after the reconnection and cause the brightening, whereas in the MHD the lower spine gets disconnected and cannot account for the brightening. The reconnection dynamics around the null line and the corresponding plasma flow direction are the same in the Hall MHD and MHD simulations and agree with the observed brightening. Nevertheless, reconnection is earlier in the Hall MHD. Hall MHD evolution nicely captures an anticlockwise circular motion of magnetic field lines in the left part of the AR that is cospatial with the location of the rotating chromospheric material on the eastern side of the AR. No such motion was found in the MHD simulation. Importantly, the simulations explicitly associate generation of large magnetic field gradients with Hall MHD compared to MHD, resulting in faster and more efficient field line slippage because of the enhanced Hall term.

Importantly, this thesis explores the role of Hall effect in magnetic reconnection and addresses the fast and impulsive reconnection within the Hall MHD. A reasonable agreement between the magnetic field dynamics in a novel Hall MHD simulation of the observed flare and the spatial features of flare brightening, suggests the Hall MHD to provide a plausible explanation for the flare reconnection. Crux of the thesis work is that the Hall effect being small scale effect cause the alteration in the dynamics near reconnection site and in turn affect the dynamics as large as system scale size, accommodating for faster dynamics.

7.2 Future Prospects

This thesis addresses the role of Hall effect in magnetic reconnection within Hall MHD framework to understand fast reconnection dynamics with particular focus on 3D. In line with the explorations carried out in this thesis work, the future scope should consist the continuation of such investigations of Hall effect on 3D magnetic reconnection which will be beneficial in understanding the underlying physics essential for transient explosive activities occurring in astrophysical plasmas. Additionally, further improvements in the model can account for the energy budget and thermodynamics of the transient events. Consequently, the future prospects are briefly presented as following:

1. In this thesis, Hall effect on the reconnections responsible for the generation and evolution of a magnetic flux rope initiated from the sheared bipolar field has been explored. However, the prominences or filaments on the Sun resemble to pre-existing magnetic flux rope structure and the exploration of Hall effect on reconnections driving the eruption of such flux ropes can be helpful in understanding the underlying physics responsible for the phenomenon like local breakage of prominences followed by the swirling motions of plasma material. In this context, we plan to do the numerical simulation of an initial analytical flux rope with an aim to explore the Hall effect on its evolution.

2. Reasonably good agreement between the dynamics obtained from the novel data-constrained Hall MHD simulation of a flare and its observations, inspires us to perform the Hall MHD data-constrained simulations for the high resolution magnetic field data ($\sim$ few km) from the ground based observatory DKIST.

3. We plan to perform observational study as well as numerical simulations to understand small scale transient events such as microflares and nanoflares which are important in understanding the coronal heating problems.

Appendix A

Data-based Hall MHD and MHD simulations of a flaring solar active region

The dimensionless time step is obtained by employing the Hall induction equation

$$\frac{\partial \mathbf{B}}{\partial t} = -d_H \nabla \times ((\nabla \times \mathbf{B}) \times \mathbf{B}), \tag{A.1}$$

for a stationary fluid. The aforementioned equation is linearized over an equilibrium magnetic field $\mathbf{B}_0$ to obtain

$$\frac{\partial \delta\mathbf{B}}{\partial t} = -d_H [\nabla \times (\nabla \times \delta\mathbf{B}) \times \mathbf{B}_0], \tag{A.2}$$

$\delta\mathbf{B}$ being the perturbation. To obtain the wave modes, the perturbation is assumed to be periodic along x and y of a Cartesian coordinate system

$$\delta B_x = \delta B_y \propto \exp[i(k_z z - \omega t)]. \tag{A.3}$$

where the equilibrium field is selected as $\mathbf{B}_0 = B_0 \hat{e}_z$. Straightforward mathematical manipulations yield the dispersion relation for the Whistler wave as

$$\omega = d_H B_0 {k_z}^2. \tag{A.4}$$

The wave number is selected as $k_z = (2\pi)/\Delta z$, Δz is the dissipation scale in the computational domain, making the choice harmonious with the philosophy used extensively in the paper. since the dimensionless $\rho_0 = 1$ in the numerical model, (A.4) can be written

$$\left(\frac{\Delta z}{\Delta t}\right)_{whis} = 4\pi^{\frac{3}{2}} d_H \left(\frac{\Delta z}{\Delta t}\right)_{Alf} \left(\frac{1}{\Delta z}\right)_{whis}. \tag{A.5}$$

With $\Delta z_{whis} = \Delta z_{Alfven} = 0.0078$, namely the dissipation scale in the present model along with d_H=0.004, while $\Delta t_{Alf} \approx 10^{-3}$ from previous numerical experiments; in the present model $\Delta t = \Delta t_{whis} \approx 10^{-4}$.

Bibliography

Alfvén, H. 1942, *Nature*, 150, 405

Alissandrakis, C. E. 1981, *Astron. Astrophys.*, 100, 197

Amari, T., & Aly, J. J. 2010, *Astron. Astrophys.*, 522, A52

Amari, T., Aly, J. J., Luciani, J. F., Boulmezaoud, T. Z., & Mikic, Z. 1997, *Solar Phys.*, 174, 129

Amari, T., Boulmezaoud, T. Z., & Aly, J. J. 2006, *Astron. Astrophys.*, 446, 691

Amari, T., Canou, A., & Aly, J.-J. 2014, *Nature*, 514, 465

Aschwanden, M. J. 2005, Physics of the Solar Corona. An Introduction with Problems and Solutions (2nd edition)

Aulanier, G., Pariat, E., Démoulin, P., & DeVore, C. R. 2006, *Solar Phys.*, 238, 347

Axford, W. I. 1984, Washington DC American Geophysical Union Geophysical Monograph Series, 30, 1

Beaudoin, P., Charbonneau, P., Racine, E., & Smolarkiewicz, P. K. 2013, *Solar Phys.*, 282, 335

Benz, A. O. 2008, Living Reviews in Solar Physics, 5, 1

Bhattacharjee, A. 2004, *Ann. Rev. Astron. Astrophys.*, 42, 365

Bhattacharjee, A., Ma, Z. W., & Wang, X. 2003, in Turbulence and Magnetic Fields in Astrophysics, ed. E. Falgarone & T. Passot, Vol. 614 351

Bhattacharyya, R., & Janaki, M. S. 2004, Physics of Plasmas, 11, 5615

Bhattacharyya, R., & Janaki, M. S. 2004, Physics of Plasmas, 11, 5615

Bhattacharyya, R., Janaki, M. S., Dasgupta, B., & Zank, G. P. 2007, *Solar Phys.*, 240, 63

Bhattacharyya, R., Low, B. C., & Smolarkiewicz, P. K. 2010, Physics of Plasmas, 17, 112901

Bineau, M. 1972, Communications on Pure and Applied Mathematics, 25, 77

Birn, J., et al. 2001, *J. Geophys. Res.*, 106, 3715

Birn, J., Hesse, M., & Schindler, K. 1997, Advances in Space Research, 19, 1763

Biskamp, D. 2000, Magnetic Reconnection in Plasmas, Vol. 3

Bobra, M. G., Sun, X., Hoeksema, J. T., Turmon, M., Liu, Y., Hayashi, K., Barnes, G., & Leka, K. D. 2014, *Solar Phys.*, 289, 3549

Book, D. L., Boris, J. P., & Hain, K. 1975, Journal of Computational Physics, 18, 248

Bora, K., Bhattacharyya, R., Prasad, A., Joshi, B., & Hu, Q. 2022, *Astrophys. J.*, 925, 197

Bora, K., Bhattacharyya, R., & Smolarkiewicz, P. K. 2021, *Astrophys. J.*, 906, 102

Boris, J. P., & Book, D. L. 1973, Journal of Computational Physics, 11, 38

Boris, J. P., & Book, D. L. 1976, Journal of Computational Physics, 20, 397

Chandrasekhar, S., & Kendall, P. C. 1957, *Astrophys. J.*, 126, 457

Charbonneau, P., & Smolarkiewicz, P. K. 2013, Science, 340, 42

Chen, P. F. 2011, Living Reviews in Solar Physics, 8, 1

Chiu, Y. T., & Hilton, H. H. 1977, *Astrophys. J.*, 212, 873

Choudhuri, A. R. 1998, The physics of fluids and plasmas : an introduction for astrophysicists

Couvidat, S., et al. 2016, *Solar Phys.*, 291, 1887

Cowling, T. G. 1953, in The Sun, ed. G. P. Kuiper 532

Dahlburg, R. B., Antiochos, S. K., & Zang, T. A. 1991, *Astrophys. J.*, 383, 420

De Rosa, M. L., et al. 2009, *Astrophys. J.*, 696, 1780

Démoulin, P. 2006, Advances in Space Research, 37, 1269

Demoulin, P., Bagala, L. G., Mandrini, C. H., Henoux, J. C., & Rovira, M. G. 1997, *Astron. Astrophys.*, 325, 305

Demoulin, P., Henoux, J. C., Priest, E. R., & Mandrini, C. H. 1996, *Astron. Astrophys.*, 308, 643

Domaradzki, J. A., & Radhakrishnan, S. 2005, Fluid Dynamics Research, 36, 385

Domaradzki, J. A., Xiao, Z., & Smolarkiewicz, P. K. 2003, Physics of Fluids, 15, 3890

Dudík, J., Janvier, M., Aulanier, G., Del Zanna, G., Karlický, M., Mason, H. E., & Schmieder, B. 2014, *Astrophys. J.*, 784, 144

Dungey, J. 1953, The London, Edinburgh, and Dublin Philosophical Magazine and Journal of Science, 44, 725

Dungey, J. W. 1961, *J. Geophys. Res.*, 66, 1043

Eisenstat, S. C. 1983, SIAM Journal on Numerical Analysis, 20, 358

Eisenstat, S. C., Elman, H. C., & Martin, H. S. 1983, SIAM Journal on Numerical Analysis, 20, 345–357

Freidberg, J. P. 1982, Reviews of Modern Physics, 54, 801

Garcia, H. A. 1994, *Solar Phys.*, 154, 275

Gary, G. A. 1989, *Astrophys. J. Suppl.*, 69, 323

Gary, G. A. 2001, *Solar Phys.*, 203, 71

Ghizaru, M., Charbonneau, P., & Smolarkiewicz, P. K. 2010, *Astrophys. J. Lett.*, 715, L133

Giovanelli, R. G. 1946, *Nature*, 158, 81

Gonzalez, W. D., & Tsurutani, B. T. 1992, in IAU Colloq. 133: Eruptive Solar Flares, ed. Z. Svestka, B. V. Jackson, & M. E. Machado, Vol. 399 277

Gopalswamy, N., Yashiro, S., Vourlidas, A., Lara, A., Stenborg, G., Kaiser, M. L., & Howard, R. A. 2004, in Bulletin of the American Astronomical Society, Vol. 36, American Astronomical Society Meeting Abstracts #204, 738

Griebel, M., Dornseifer, T., & Neunhoeffer, T. 1998, Numerical simulation in fluid dynamics: a practical introduction (the Society for Industrial and Applied Mathematics)

Grinstein, F., Margolin, L., & Rider, W. 2007, Implicit Large Eddy Simulation: Computing Turbulent Fluid Dynamics, Cambridge University Press

Hasegawa, A. 1985, Advances in Physics, 34, 1

Haynes, A. L., & Parnell, C. E. 2007, Physics of Plasmas, 14, 082107

Hesse, M., Birn, J., & Kuznetsova, M. 2001, *J. Geophys. Res.*, 106, 3721

Hesse, M., & Schindler, K. 1988, *J. Geophys. Res.*, 93, 5559

Hoeksema, J. T., et al. 2014, *Solar Phys.*, 289, 3483

Hornig, G., & Schindler, K. 1996, Physics of Plasmas, 3, 781

Howard, T. A., & Tappin, S. J. 2009, *Space Sci. Rev.*, 147, 31

Hoyle, F. 1949, Some recent researches in solar physics.

Hu, Q., & Dasgupta, B. 2008, *Solar Phys.*, 247, 87

Hu, Q., Dasgupta, B., Choudhary, D. P., & Büchner, J. 2008, *Astrophys. J.*, 679, 848

Hu, Q., Dasgupta, B., Derosa, M. L., Büchner, J., & Gary, G. A. 2010, Journal of Atmospheric and Solar-Terrestrial Physics, 72, 219

Huba, J. D. 2003, Hall Magnetohydrodynamics - A Tutorial, ed. J. Büchner, M. Scholer, & C. T. Dum (Berlin, Heidelberg: Springer Berlin Heidelberg), 166

Illing, R. M. E., & Hundhausen, A. J. 1985, *J. Geophys. Res.*, 90, 275

Inoue, S., Hayashi, K., Magara, T., Choe, G. S., & Park, Y. D. 2014, *Astrophys. J.*, 788, 182

Jiang, C., & Feng, X. 2014, *Solar Phys.*, 289, 63

Jiang, C., Feng, X., Wu, S. T., & Hu, Q. 2013, *Astrophys. J. Lett.*, 771, L30

Jiang, C., Wu, S. T., Feng, X., & Hu, Q. 2016, Nature Communications, 7, 11522

Joshi, B., Mitra, P. K., Bhattacharyya, R., Upadhyay, K., Oberoi, D., Sasikumar Raja, K., & Monstein, C. 2021, *Solar Phys.*, 296, 85

Kumar, D., & Bhattacharyya, R. 2011, Physics of Plasmas, 18, 084506

Kumar, D., Bhattacharyya, R., & Smolarkiewicz, P. K. 2013, Physics of Plasmas, 20, 112903

Kumar, D., Bhattacharyya, R., & Smolarkiewicz, P. K. 2015a, Physics of Plasmas, 22, 012902

Kumar, S., & Bhattacharyya, R. 2016, Physics of Plasmas, 23, 044501

Kumar, S., Bhattacharyya, R., Dasgupta, B., & Janaki, M. S. 2017, Physics of Plasmas, 24, 082902

Kumar, S., Bhattacharyya, R., Joshi, B., & Smolarkiewicz, P. K. 2016, *Astrophys. J.*, (in press)

Kumar, S., Bhattacharyya, R., & Smolarkiewicz, P. K. 2015b, Physics of Plasmas, 22, 082903

Lee, C. O., Luhmann, J. G., Hoeksema, J. T., Sun, X., Arge, C. N., & de Pater, I. 2011, *Solar Phys.*, 269, 367

Lemen, J. R., et al. 2012, *Solar Phys.*, 275, 17

Liu, C., Prasad, A., Lee, J., & Wang, H. 2020, *Astrophys. J.*, 899, 34

Liu, R., et al. 2016, *Astrophys. J.*, 818, 148

Liu, Y., et al. 2012, Solar Physics, 279, 295

Liu, Y.-H., Cassak, P., Li, X., Hesse, M., Lin, S.-C., & Genestreti, K. 2022, Communications Physics, 5, 97

Low, B. C. 1996, *Solar Phys.*, 167, 217

Ma, Z. W., & Bhattacharjee, A. 2001, *J. Geophys. Res.*, 106, 3773

Mahajan, S. M., & Yoshida, Z. 1998, Phys. Rev. Lett., 81, 4863

Margolin, L. G., Rider, W. J., & Grinstein, F. F. 2006, Journal of Turbulence, 7, N15

Mininni, P. D., Gómez, D. O., & Mahajan, S. M. 2003, *Astrophys. J.*, 587, 472

Mozer, F. S., Bale, S. D., & Phan, T. D. 2002, *Phys. Rev. Lett.*, 89, 015002

Müller, D., Marsden, R. G., St. Cyr, O. C., & Gilbert, H. R. 2013, *Solar Phys.*, 285, 25

Nakagawa, Y. 1974, *Astrophys. J.*, 190, 437

Nakagawa, Y., & Raadu, M. A. 1972, *Solar Phys.*, 25, 127

Nayak, S. S., Bhattacharyya, R., Prasad, A., Hu, Q., Kumar, S., & Joshi, B. 2019, *Astrophys. J.*, 875, 10

Nayak, S. S., Bhattacharyya, R., Smolarkiewicz, P. K., Kumar, S., & Prasad, A. 2020, *Astrophys. J.*, 892, 44

Otto, A. 2001, *J. Geophys. Res.*, 106, 3751

Pant, V., Datta, A., Banerjee, D., Chandrashekhar, K., & Ray, S. 2018, The Astrophysical Journal, 860, 80

Parker, E. N. 1957, *J. Geophys. Res.*, 62, 509

Parker, E. N. 1994, Spontaneous current sheets in magnetic fields : with applications to stellar x-rays. International Series in Astronomy and Astrophysics, 1

Parnell, C. E., Smith, J. M., Neukirch, T., & Priest, E. R. 1996, Physics of Plasmas, 3, 759

Pesnell, W. D., Thompson, B. J., & Chamberlin, P. C. 2012a, *Solar Phys.*, 275, 3

Pesnell, W. D., Thompson, B. J., & Chamberlin, P. C. 2012b, *Solar Phys.*, 275, 3

Petschek, H. E. 1964, NASA Special Publication, 50, 425

Pontin, D. I., & Priest, E. R. 2022, Living Reviews in Solar Physics, 19, 1

Prasad, A., Bhattacharyya, R., Hu, Q., Kumar, S., & Nayak, S. S. 2018, *Astrophys. J.*, 860, 96

Prasad, A., Bhattacharyya, R., & Kumar, S. 2017, *Astrophys. J.*, 840, 37

Prasad, A., Dissauer, K., Hu, Q., Bhattacharyya, R., Veronig, A. M., Kumar, S., & Joshi, B. 2020, *Astrophys. J.*, 903, 129

Priest, E. 2014, Magnetohydrodynamics of the Sun

Priest, E., & Forbes, T. 2000, Magnetic Reconnection

Priest, E. R., & Titov, V. S. 1996, Proceedings of the Royal Society of London Series A, 354, 2951

Prusa, J., Smolarkiewicz, P., & Wyszogrodzki, A. 2008, Computers & Fluids, 37, 1193

Prusa, J. M., & Smolarkiewicz, P. K. 2003, Journal of Computational Physics, 190, 601

Prusa, J. M., Smolarkiewicz, P. K., & Wyszogrodzki, A. A. 2008, Computers Fluids, 37, 1193–1207

Ramsden, E. 2006, in Hall-Effect Sensors (Second Edition) (Second Edition ed.), ed. E. Ramsden (Burlington: Newnes), 1

Rider, W. J. 2006, International Journal for Numerical Methods in Fluids, 50, 1145

Rossby, C.-G., Namias, J., & Simmers, R. G. 1938, Physical Oceanography and Meteorology, 17

Ruderman, M. S., & Roberts, B. 2002, *Astrophys. J.*, 577, 475

Sakurai, T. 1981, *Solar Phys.*, 69, 343

Sarp Yalim, M., Prasad, A., Pogorelov, N., Zank, G., & Hu, Q. 2020, arXiv e-prints, arXiv:2007.12275

Savcheva, A., Pariat, E., McKillop, S., McCauley, P., Hanson, E., Su, Y., & DeLuca, E. E. 2016, *Astrophys. J.*, 817, 43

Scherrer, P. H., et al. 2012, *Solar Phys.*, 275, 207

Schindler, K., Hesse, M., & Birn, J. 1988, *J. Geophys. Res.*, 93, 5547

Schou, J., et al. 2012, *Solar Phys.*, 275, 229

Schrijver, C. J., et al. 2006, *Solar Phys.*, 235, 161

Scudder, J. D. 1997, *Space Sci. Rev.*, 80, 235

Seehafer, N. 1978, *Solar Phys.*, 58, 215

Shi, C., Tenerani, A., Velli, M., & Lu, S. 2019, *Astrophys. J.*, 883, 172

Shibata, K., & Magara, T. 2011, Living Reviews in Solar Physics, 8

Shibata, K., & Tanuma, S. 2001, Earth, Planets, and Space, 53, 473

Smolarkiewicz, P., & Szmelter, J. 2011, Acta Geophysica, 59, 1109

Smolarkiewicz, P. K. 1983, Monthly Weather Review, 111, 479

Smolarkiewicz, P. K. 1984, Journal of Computational Physics, 54, 325

Smolarkiewicz, P. K. 1991, Monthly Weather Review, 119, 2505

Smolarkiewicz, P. K. 2006, International Journal for Numerical Methods in Fluids, 50, 1123

Smolarkiewicz, P. K., & Charbonneau, P. 2013, Journal of Computational Physics, 236, 608

Smolarkiewicz, P. K., & Clark, T. L. 1986, Journal of Computational Physics, 67, 396

Smolarkiewicz, P. K., & Grabowski, W. W. 1990, Journal of Computational Physics, 86, 355

Smolarkiewicz, P. K., Grubišić, V., & Margolin, L. G. 1997, Monthly Weather Review, 125, 647

Smolarkiewicz, P. K., & Margolin, L. G. 1993, Monthly Weather Review, 121, 1847

Smolarkiewicz, P. K., & Margolin, L. G. 1997, Atmosphere Ocean, 35, 127

Smolarkiewicz, P. K., & Margolin, L. G. 1998, Journal of Computational Physics, 140, 459

Smolarkiewicz, P. K., & Prusa, J. M. 2002, International Journal for Numerical Methods in Fluids, 39, 799

Smolarkiewicz, P. K., & Pudykiewicz, J. A. 1992, Journal of Atmospheric Sciences, 49, 2082

Smolarkiewicz, P. K., & Szmelter, J. 2009, Journal of Computational Physics, 228, 33

Sonnerup, B. U. Ö. 1979, Magnetic field reconnection, Vol. 3 45

Sweet, P. A. 1958, in IAU Symposium, Vol. 6, Electromagnetic Phenomena in Cosmical Physics, ed. B. Lehnert, 499

Terasawa, T. 1983, *Geophys. Res. Lett.*, 10, 475

Titov, V. S. 2007, *Astrophys. J.*, 660, 863

Vasyliunas, V. M. 1975, Reviews of Geophysics and Space Physics, 13, 303

Venkatakrishnan, P., & Gary, G. A. 1989, *Solar Phys.*, 120, 235

Vourlidas, A., Buzasi, D., Howard, R. A., & Esfandiari, E. 2002, in ESA Special Publication, Vol. 506, Solar Variability: From Core to Outer Frontiers, ed. A. Wilson, 91

Vourlidas, A., & Howard, R. A. 2006, *Astrophys. J.*, 642, 1216

Vourlidas, A., Lynch, B. J., Howard, R. A., & Li, Y. 2013, *Solar Phys.*, 284, 179

Wang, H., Liu, C., Deng, N., Zeng, Z., Xu, Y., Jing, J., & Cao, W. 2014, *Astrophys. J. Lett.*, 781, L23

Wang, X., Bhattacharjee, A., & Ma, Z. W. 2000, *J. Geophys. Res.*, 105, 27633

Wheatland, M. S., Sturrock, P. A., & Roumeliotis, G. 2000, The Astrophysical Journal, 540, 1150

Wiegelmann, T. 2004, *Solar Phys.*, 219, 87

Wiegelmann, T. 2008, Journal of Geophysical Research (Space Physics), 113, A03S02

Wiegelmann, T., & Inhester, B. 2010, *Astron. Astrophys.*, 516, A107

Wiegelmann, T., Inhester, B., & Sakurai, T. 2006a, *Solar Phys.*, 233, 215

Wiegelmann, T., Inhester, B., & Sakurai, T. 2006b, *Solar Phys.*, 233, 215

Wiegelmann, T., & Sakurai, T. 2012, Living Reviews in Solar Physics, 9, 5

Wiegelmann, T., & Sakurai, T. 2021, Living Reviews in Solar Physics, 18, 1

Woltjer, L. 1958, Proceedings of the National Academy of Science, 44, 489

Wyper, P. F., & Pontin, D. I. 2014, Physics of Plasmas, 21, 102102

Yoshida, Z., & Giga, Y. 1990, Mathematische Zeitschrift, 204, 235

Zhong, Z., Guo, Y., & Ding, M. D. 2021, Nature Communications, 12, 2734